



## ARCHIVIO ISTITUZIONALE DELLA RICERCA

### Alma Mater Studiorum Università di Bologna Archivio istituzionale della ricerca

Alpine tectono-metamorphic evolution of the Corsica basement

This is the final peer-reviewed author's accepted manuscript (postprint) of the following publication:

*Published Version:*

*Availability:*

This version is available at: <https://hdl.handle.net/11585/916606> since: 2023-02-21

*Published:*

DOI: <http://doi.org/10.1111/jmg.12696>

*Terms of use:*

Some rights reserved. The terms and conditions for the reuse of this version of the manuscript are specified in the publishing policy. For all terms of use and more information see the publisher's website.

This item was downloaded from IRIS Università di Bologna (<https://cris.unibo.it/>).  
When citing, please refer to the published version.

(Article begins on next page)

This is the final peer-reviewed accepted manuscript of:

**Rossetti, F., Cavazza, W., Di Vincenzo, G., Lucci, F., Theye, T. Alpine tectono-metamorphic evolution of the Corsica basement (2023) Journal of Metamorphic Geology, 41 (2), pp. 299-326**

The final published version is available online at:

<https://dx.doi.org/10.1111/jmg.12696>

Terms of use:

Some rights reserved. The terms and conditions for the reuse of this version of the manuscript are specified in the publishing policy. For all terms of use and more information see the publisher's website.

*This item was downloaded from IRIS Università di Bologna (<https://cris.unibo.it/>)*

*When citing, please refer to the published version.*

**Alpine tectono-metamorphic evolution of the Corsica basement**

Journal:	<i>Journal of Metamorphic Geology</i>
Manuscript ID	JMG-22-0025
Wiley - Manuscript type:	Original Article
Date Submitted by the Author:	10-May-2022
Complete List of Authors:	Rossetti, Federico; Universita degli Studi Roma Tre Dipartimento di Scienze Cavazza, William; Universita degli Studi di Bologna Dipartimento di Scienze Biologiche Geologiche ed Ambientali Vincenzo, Gianfranco Di; Istituto di Geoscienze e Georisorse Consiglio Nazionale delle Ricerche Lucci, Federico; Universita degli Studi di Bari Aldo Moro Dipartimento di Scienze della Terra e Geoambientali THEYE, Thomas; Universitat Stuttgart Institut fur Anorganische Chemie
Keywords:	Crustal shortening, low-grade metamorphism, Ar-Ar geochronology, Alpine orogeny, Corsica

SCHOLARONE™  
Manuscripts

1    **Alpine tectono-metamorphic evolution of the Corsica basement**

2

3    Federico Rossetti<sup>1,\*</sup>, William Cavazza<sup>2</sup>, Gianfranco Di Vincenzo<sup>3</sup>, Federico Lucci<sup>4</sup>, Thomas Theye<sup>5</sup>

4

5

6

7    <sup>1</sup>Dipartimento di Scienze, Università Roma Tre, Roma, Italy

8

9    <sup>2</sup>Dipartimento di Scienze Biologiche, Geologiche e Ambientali, Università degli Studi di Bologna,  
10    Bologna, Italy

11

12    <sup>3</sup>Istituto di Geoscienze e Georisorse, CNR, Pisa, Italy

13

14    <sup>4</sup>Dipartimento di Scienze della Terra e Geoambientali, Università degli Studi di Bari “Aldo Moro”,  
15    Bari, Italy

16

17    <sup>5</sup>Institut für Anorganische Chemie, Universität Stuttgart, Stuttgart, Germany

18

19

20

21

22

23

24    **Running title: Alpine tectonics of the Corsica basement**

25

26

27

28

29

30    **Corresponding Author:**

31    Federico Rossetti

32    Dipartimento di Scienze

33    Sezione di Scienze Geologiche

34    Università Roma Tre

35    Largo S. L. Murialdo, 1

36    00146 Roma (ITALY)

37    Phone: +390657338043

38    FAX: +390657338201

39    e-mail: federico.rossetti@uniroma3.it

40

41

42     **Abstract**

43         The Alpine orogenic edifice of Corsica (northern Tyrrhenian Sea) offers the possibility to  
44         investigate the mode through which continental crust responds to the propagation of regional  
45         shortening at convergent plate margins. The geology of Corsica has been traditionally described  
46         separating domains affected by the Alpine tectonism (Alpine Corsica) from those that did not  
47         experience the Alpine tectono-metamorphic overprint (Hercynian Corsica), but recent studies  
48         show that most of Hercynian Corsica was thermally reset in post-Eocene times, questioning this  
49         scheme. The continental units formed at the expenses of the stretched continental margin of the  
50         European plate and consist of Hercynian granitoid basement rocks and cover sequences (Permian  
51         volcaniclastics and Mesozoic sedimentary successions). By integrating meso- and micro-structural  
52         investigations with metamorphic thermobarometry and Ar-Ar geochronology along seriate  
53         structural transects running across the basement section exposed below the Alpine orogenic  
54         wedge, we document middle-late Eocene (ca. 50-33 Ma) westward-verging syn-metamorphic  
55         (low-grade blueschist facies) thick-skinned, basement-involved thrusting. Significantly, crustal  
56         shortening in the continental basement predated of ca. 15-10 Ma the subduction zone  
57         metamorphism in the oceanic-derived Schistes Lustrés Complex. When the P-T-t-deformation  
58         history as reconstructed from the Corsica basement is integrated with the regional scenario of the  
59         Alpine-Apennine orogeny, a tectonic reconstruction is proposed framing the Alpine orogeny in  
60         Corsica within the Apennine-Maghrebian subduction system in the retroside (retrowedge) of the  
61         Apennine orogenic wedge.

62

63         **Key words:** Crustal shortening, low-grade metamorphism, Ar-Ar geochronology, Alpine orogeny,  
64         Corsica

65

66     **1. Introduction**

67         The mode and timing through which regional convergence is accommodated in the  
68         continental crust are key issues to define how orogenic processes and continental accretion occur  
69         in space and time. At crustal scale, tectonic shortening can be accommodated through uniform  
70         thickening (pure-shear deformation mode) or underthrusting (simple shear deformation mode;  
71         e.g. Allmendinger and Gubbel, 1996). Both thin- (basement not involved) and thick-skinned  
72         (basement-involved) structural styles are recognized in active and fossil orogenic belts (e.g.,  
73         Allmendinger and Gubbel, 1996; Pfiffner, 2006), with implications on continental rheology (e.g.,  
74         Babeyko and Sobolev; 2005; Mouthereau et al., 2013; Lowry and Marta Pérez-Gussinye, 2011;  
75         Lacombe and Bellhasen, 2016 ) and the geodynamics at convergent plate margins (e.g., Nemčok et  
76         al., 2013; Lacombe and Bellhasen, 2016).

77         As a part of the Eurasia paleomargin during the Alpine Cenozoic convergence processes  
78         involving the Eurasian, Iberian and African plates, the island of Corsica in the northern Tyrrhenian  
79         Sea (Fig. 1a) (e.g., Faccenna et al., 2001; Rosembaum et al., 2002; Lacombe and Jolivet, 2005;  
80         Handy et al., 2010; Molli and Malavieille, 2010; Carminati et al., 2012; Turco et al., 2012; Malusà  
81         et al., 2015; Jolivet et al., 2021) is an ideal case study to investigate how the continental  
82         lithosphere responds to propagation of regional shortening at convergent plate margins. Plate  
83         convergence along the western end of the Alpine orogen and subsequent rifting and drifting has  
84         exposed on the island of Corsica a wide swath of crystalline basement complex originally covered  
85         by the Alpine orogenic wedge (Jolivet et al., 1990; 1998; Molli and Malavieille, 2010; Vitale  
86         Brovarone et al., 2013; Rossetti et al., 2015; Di Rosa et al., 2020a). This has made possible  
87         observation on shortening-related structures underlying the Alpine orogenic wedge.

88         The geology of Corsica has been classically described separating domains affected by the  
89         Alpine tectonism (Alpine Corsica) from those that did not experience the Alpine tectono-  
90         metamorphic overprint (Hercynian Corsica) forming the foreland of the Alpine orogen as a part of  
91         the European plate (e.g. Duran Delga, 1984; Rossi et al., 1994; Vitale Brovarone et al., 2013) (Fig.  
92         1b). This simplistic subdivision contrasts with the available thermo-chronometric data (Cavazza et  
93         al., 2001; Zarki-Jhaki et al., 2004; Fellin et al., 2006; Danisik et al., 2007), which document that  
94         most of the Hercynian Corsica was thermally reset, demonstrating that virtually all the island was  
95         covered by the Alpine orogenic wedge and/or by foreland basins (Fig. 1c).

96         While the Alpine tectono-metamorphic evolution of the Mesozoic-Cenozoic cover rocks of  
97         the former European continental margin has been recently assessed (Di Rosa et al., 2019, 2017;

98 2020a; Malasoma et al., 2020; Marroni et al., 2020), the structural style, timing and thermo-baric  
99 environments of the Alpine deformation in the Hercynian continental basement is still poorly  
100 documented, despite a mounting body of structural, petrographic and geochronological evidence  
101 of Alpine tectonism (Malasoma et al., 2006; 2019; Malasoma and Marroni, 2007; Garfagnoli et al.,  
102 2009; Di Vincenzo et al., 2016; Di Rosa et al., 2017; 2020b; Frassi et al., 2022). Deciphering the  
103 pressure-temperature-time-deformation (P-T-t-d) history of the Corsica basement during the  
104 Alpine orogeny is essential to frame in a coherent scenario the Alpine tectonic/geodynamic  
105 evolution in the hinterland of the Alps-Apennine (see Vitale Brovarone and Herwatz, 2013).

106 In this study, we describe a coherent set of Alpine-age tectono-metamorphic structures  
107 affecting both Alpine and Hercynian Corsica, as traditionally defined (Figs. 1b and 2). We describe  
108 an early-late Eocene (50-33 Ma) westward-verging syn-metamorphic thick-skinned, basement-  
109 involved thrusting. Implications of these results are framed within the regional scenario of the  
110 Alpine-Apennine orogenic system.

111

## 112 2. Geological background

113 Corsica Island is a fragment of the former southern continental margin of the Eurasia plate,  
114 involved first in the formation of the Alpine convergent margin during consumption of the  
115 Mesozoic Alpine Tethys (Ligurian–Piedmont branch) oceanic realm and successively in the  
116 Oligocene-Miocene rifting and drifting processes leading to opening of the Liguro-Provençal and  
117 Tyrrhenian back-arc basins (Doglioni et al., 1997; Rosembaum et al., 2002; Carminati et al., 2012;  
118 Faccenna et al., 2001; Lacombe and Jolivet, 2005; Molli and Malaiveille 2010).

119 The Alpine orogenic construction caused the formation of a west-verging (present-day  
120 coordinates) orogenic wedge (Fig. 2), formed at the expenses of both the ocean-derived and the  
121 former continental margin units, thrusted onto the Hercynian Corsica (Vitale Brovarone et al.,  
122 2013; Di Rosa et al., 2002; Jolivet et al., 1990; Molli et al., 2006; Rossetti et al., 2015 ). The nappe  
123 edifice consists, from top to bottom, of (i) non-metamorphic or slightly metamorphosed ophiolite  
124 units (Balagne, Nebbio and Macinaggio units), (ii) high-pressure (eclogite to blueschist facies)  
125 subduction channel units of the Schistes Lustrés Complex, a tectonic mélange made of oceanic-  
126 and continental units, and (iii) European continental crust tectonic slices, made of the Tenda and  
127 the external continental units (Durand Delga, 1984; Jolivet et al., 1990; Vitale Brovarone et al.,  
128 2013; Di Rosa et al., 2020a). The latter complex of units, also referred to as Lower units, consists of  
129 various tectonic slices made of Permian-Carboniferous igneous rocks intruded into Pan-African

130 metamorphic host rocks, unconformably covered by Permian volcanics and volcaniclastic deposits  
131 (Rossi et al., 1994; Paquette et al., 2003; Di Rosa et al., 2020b) and by Mesozoic to Eocene  
132 sedimentary successions (e.g., Bezert and Caby, 1988; Rossi et al., 1994; Cavazza et al., 2018; Di  
133 Rosa et al., 2020a). These continent-derived tectonic slices are affected by a diffuse Alpine  
134 tectono-metamorphic overprint, with peak conditions equilibrated within the low-grade blueschist  
135 metamorphic facies (Tribuzio and Giacomini, 2002; Molli et al., 2006; Maggi et al., 2012; Rossetti  
136 et al., 2015; Di Rosa et al., 2019).

137 The age of subduction zone HP/LT metamorphism is constrained is late Eocene (ca. 37-34  
138 Ma), based on U-Pb zircon (Martin et al., 2011) and Lu-Hf garnet and lawsonite (Vitale Brovarone  
139 and Herwatz, 2013) dating of the eclogite- and blueschist facies rocks of the Schistes Lustrés  
140 Complex. A minimum late Eocene age (35 Ma) is also indicated by Ar-Ar phengite geochronology  
141 from the Schistes Lustrés Complex (Brunet et al., 2000). The tectonic assembly of the ophiolite  
142 domain units onto the Hercynian Corsica is primarily constrained by the activity of the ductile-to-  
143 brittle East Tenda Shear Zone (ETSZ), the Alpine shear zone boundary between the continental  
144 margin of the European plate and the Ligurian-Piedmont ocean. The ETSZ experienced a polyphase  
145 tectono-metamorphic evolution, typified by syn-blueschist top-to-the-W thrusting, overprinted by  
146 ductile-to-brittle top-to-the-E extension (Gibbons and Horak, 1984; Jolivet. et al., 1990; Gueydan  
147 et al., 2003; Maggi et al., 2014; Molli et al., 2006; Rossetti et al., 2015; Beaudouin et al., 2020). Most  
148 of the available geochronological data on the syn-blueschist shear zones clusters in the latest  
149 Eocene-earliest Oligocene (35-32 Ma; Ar-Ar phengite geochronology: Brunet et al., 2000; Beaudouin  
150 et al., 2020; Rb-Sr geochronology: Rossetti et al. 2015), considered as the age of the terminal  
151 Alpine overthrusting (Brunet et al., 2000; Rossetti et al., 2015; Beaudouin et al., 2020). Older U-Pb  
152 rutile ages (ca.  $54 \pm 8$  Ma; Maggi et al. 2012), together with the maximum Ar-Ar phengite ages (ca.  
153 45 Ma; Brunet et al., 2000), suggest an early Eocene stage for the ETSZ nucleation. The post-  
154 orogenic top-to-the-E reactivation of the ETSZ culminates during the early Miocene, synchronously  
155 with syn-greenschist extensional shearing in the Schistes Lustrés (Rossetti et al., 2015).

156 Tectono-metamorphic data from the frontal, N-S striking thrust zone bounding the contact  
157 zone between the oceanic-derived Alpine nappe stack and Hercynian Corsica (here after referred  
158 to as Alpine deformation front, ADF; Fig. 2) document a polyphase evolution in the  
159 metasedimentary cover units of the Corsica basement, associated with a progressive top-to-the-  
160 west ductile-to-brittle shearing, equilibrated under low-grade blueschist to greenschist facies  
161 conditions (Di Rosa et al., 2019; 2020a-b). Significantly, distinct pressure-temperature-

162 deformation histories characterize the different tectonic units, indicating different burial and  
163 exhumation trajectories during the crustal slicing associated with the overthrusting of the Schistes  
164 Lustrés Complex onto the European plate margin (Di Rosa et al., 2019). Petro-tectonic evidence  
165 has shown that Alpine deformation and low-grade greenschist to blueschist metamorphism have  
166 also affected the Hercynian granitoid basement of Central Corsica, in the footwall of the main  
167 Alpine contact (Garfagnoli et al., 2009; Malasoma and Marroni, 2006; Di Vincenzo et al, 2016). Di  
168 Vincenzo et al. (2016) documented late Eocene (ca. 37-35 Ma) high-angle, NS-striking mylonitic  
169 shear zones, developed under P-T conditions of  $\geq 300$  °C and 0.5-0.6 GPa, and attributed to Alpine  
170 strike-slip reactivation of the Hercynian basement.  $^{40}\text{Ar}$ - $^{39}\text{Ar}$  minimum ages of  $\sim 46$  Ma from  
171 microstructurally muscovite relics were also assigned to the Alpine tectono-metamorphic  
172 evolution (Di Vincenzo et al, 2016).

173 Biostratigraphic data from the Corsica continental margin cover units constrain the Alpine  
174 orogenic tectonics to pre-Priabonian ( $>38$  Ma) (Ferrandini et al., 2010) times, although post-  
175 Bartonian ( $<38$  Ma) deformation was also reported (Bezert & Caby, 1988). An upper age limit for  
176 the ductile Alpine tectono-metamorphic evolution is provided by the sedimentation of the early  
177 Miocene deposits of the Saint Florent and Francardo Basins, sealing the early thrust contacts  
178 (Dallan & Puccinelli, 1995; Ferrandini et al., 1998; Cavazza et al., 2001). This is in line with the  
179 available thermochronological data, indicating exhumation of the deep roots of the Alpine orogen  
180 during the late Eocene-Miocene (Fellin et al., 2006; Cavazza et al., 2001; Zarki-Jakni et al., 2004;  
181 Danisik et al., 2007).

182

183

### 184 3. Materials and Methods

185 We investigated the structural architecture and the tectono-metamorphic signature of the  
186 continental basement of central Corsica along three seriate E-W trending geological transects  
187 (transect-1 to -3), running across the ADF into the easternmost portion of the Hercynian basement  
188 complex (Fig. 2), with the aim to compare structures and provide ultimate thermobaric and  
189 geochronological constraints on the tectono-metamorphic coupling between Alpine and Hercynian  
190 Corsica. The geology of the study area is presented in Di Rosa et al. (2017; 2020a) and Malasoma  
191 et al. (2020), where the structural architecture of the tectonic boundary zone between the  
192 Schistes Lustrés and the external continental units is detailed. We focus our study exclusively on  
193 the Hercynian basement units (Hercynian granitoids and Permian volcanic deposits) either

194 exposed at the footwall or in the immediate hanging wall of the ADF (transect-1 to -3 in Fig. 2).  
195 The hanging wall units define the so-called Corte slices (Di Rosa et al., 2019, 2020a).

196 The research rationale is based on a multidisciplinary approach that combines field-based,  
197 meso- and micro-structural investigation with metamorphic thermobarometry (inverse and  
198 forward modelling techniques) and Ar-Ar geochronology. Samples for laboratory work were  
199 collected based on the textural and mineralogical evidence at the outcrop scale. Table 1 reports  
200 the location, textures and petrography of the studied samples. Appendix-A details the analytical  
201 protocols and methods adopted in the study. In the following, mineral abbreviations follow  
202 Whitney and Evans (2010), complemented by Wm for white mica.

203

#### 204 **4. Structures in the field**

205 This section describes the structural architecture along the three geological transects and  
206 detail the tectono-metamorphic setting of the sampling sites. Transect-1 and transect-2 illustrate  
207 the deformation structures across the ADF entering Hercynian Corsica, whilst transect-3 is located  
208 exclusively within the Hercynian basement complex (Fig. 2).

209

##### 210 **4.1 Transect-1**

211 Structure in the Lower units (here made of the Castiglione Popolasca unit; Di Rosa et al.,  
212 2020a) is characterized by a stack of west-verging ductile-to-brittle thrust slices that involve the  
213 Hercynian granitoid rocks and its Permian volcaniclastic covers. Overall, a tectonic doubling of the  
214 stratigraphic column is documented. Eocene metabreccias, unconformably covering the basement  
215 rocks, are also involved in the compressional deformation (see also Di Rosa et al., 2019) (Fig. 3a).

216 Moving from west to east, a marked increase in the deformation intensity is observed in the  
217 Permian volcanics in a transition from D<sub>1</sub> to D<sub>2</sub> deformation (Figs. 3a-b). To the east, the main  
218 structural fabric is a penetrative, sub-vertical S<sub>1</sub>, NNW-SSE striking (N02°, 83°; n=19) metamorphic  
219 foliation that transposes the S<sub>0</sub> layering (S tectonites). The S<sub>1</sub> foliation is axial planar to upright  
220 isoclinal folds with sub-horizontal hinge lines, trending sub-parallel to the S<sub>1</sub> foliation (N353°, 18;  
221 n= 23). The L<sub>1</sub> lineations, defined by Qz-Wm alignments, are poorly evident but systematically  
222 trend down-dip (Fig. 3b-d). The S<sub>1</sub> foliation is deformed by a spaced D<sub>2</sub> crenulation cleavage  
223 defined by a S<sub>2</sub> foliation trending sub-parallel to S<sub>1</sub> and shallowly dipping to the east (N353°, 19°;  
224 n=16) (Figs. 3d). To the west, the intensity of the D<sub>2</sub> deformation increases in the Permian

225   volcaniclastics structurally lying below the Hercynian granitoids. There, the  $S_0$  foliation is  
 226   transposed by  $S_1$  and progressive transition from east-dipping  $S_2$  crenulation to shear foliation is  
 227   observed, with development of a ca. 100 m thick panel of S-L and S-C tectonites, dipping shallowly  
 228   (ca. 30°) to the east ( $S_2$  mean strike: N01°, 27°, n= 56). The  $L_2$  stretching lineations are dip-parallel  
 229   (N81°, 28°; n=56), and made of Qz-Wm alignments. This shear zone separates two tectonic slices  
 230   of Hercynian granitoids (Figs. 3a-b, e). The sense of shear is systematically top-the-W as  
 231   documented by the S-C fabric and the asymmetry of  $F_2$  intrafoliar folds (Fig. 3e).

232         The Hercynian granitoid rocks below the major tectonic contact dominantly show primary  
 233   equigranular texture. Brittle deformation structures are widespread and mostly characterized by  
 234   conjugate sets of sub-vertical NE-SW and NW-SE striking fault systems and joints, with mutual  
 235   cross-cutting relationships. Slickenlines, dominantly defined by wear and abrasion tracks, are  
 236   either sub-horizontal or dip-parallel (Fig. 3b). Shear criteria, as provided by synthetic Riedel shears,  
 237   grooves and abrasion structures, indicate dextral-reverse and sinistral-reverse kinematics for the  
 238   NE-SW and NW-SE striking fault systems, respectively. These fault systems overprint subparallel  
 239   discrete (up to 5-meter-thick) anastomosing zones of ductile shearing (mylonites and  
 240   protomylonites; Fig. 3f-g) that are observed up to ca. 4 km from the ADF. Such ductile zones of  
 241   shearing bear oblique stretching lineations, provided by Qz-Wm mica alignments. Shear criteria as  
 242   dominantly provided by S-C fabrics and sigma-type porphyroclasts (quartz and K-feldspar)  
 243   document dextral-reverse and sinistral-reverse kinematics for the NE-SW and the NW-SE striking  
 244   shear zones, respectively (Figs. 3b, f-g). Significantly these ductile shear zones are observed in sites  
 245   of extensive structurally controlled fluid flow as documented by a pervasive network of syn-  
 246   metamorphic veining and marked alteration halos. The vein filling is dominantly made of Qz-Wm ±  
 247   Cb, whilst the alteration halos consists of Wm-Stop-Ep-Ttn±Amp (see below) (Fig. 3h).

248

#### 249   **4.2 Transect-2**

250         Transect-2 runs across the tectonic contacts between the Schistes Lustrés Complex and the  
 251   Lower units (here made of the Ghisoni unit; Di Rosa et al., 2020a) and between the latter and the  
 252   Hercynian basement (Figs. 2 and 4a). The contact between the Schistes Lustrés and the Lower  
 253   units is marked by a dm-thick cataclastic zone striking NNW-SSE, dipping steeply to the ENE.  
 254   Entering the Lower units, a NNW-SSE striking  $S_1$  sub-vertical foliation is observed in the Permian  
 255   volcaniclastics. Moving towards the west, the Permian volcaniclastics are in tectonic contact with  
 256   slightly deformed granitoid rocks, where an incipient subhorizontal, shallowly SE-dipping

secondary foliation is observed (CO34 in Fig. 4a). Farther west, isotropic primary igneous fabrics are predominant within the granitoid rocks. Major ductile shear localisation occurs ca. 3 km west of the fault-controlled contact between the Schistes Lustrés and the Lower units. Here, a ca. 50 m thick zone of ductile shearing is defined by strongly mylonitized granitoids with a gneissic texture, where porphyroclastic Qz-Ksp aggregates occur within a fine-grained white mica matrix (Sample CO36 in Fig. 4). Finite deformation ( $D_2$ ) is partitioned between domains of coaxial and non-coaxial shearing, which deform an early-formed, east-dipping sub-vertical  $S_1$  foliation (Fig. 4b).  $S_2$  foliation dips shallowly towards the east (mean: N08°, 31°; n= 32), bearing dip-parallel L2 stretching lineations (N78°, 32°; n=32) defined by Qz-Wm aggregates. The sense of shear, as deduced by the S-C fabric, sigma-type porphyroclasts and fold asymmetry is systematically top-to-the-W (Figs. 4c-d). To sum-up, the reconstructed structural architecture along Transect-2 documents a major tectonic doubling of the continental basement units, with major shear strain localization along the contact between the Hercynian granitoids and the Permian volcanoclastics (Fig. 4a).

270

#### 271 **4.3 Transect-3**

Transect-3 runs along the Défilé de l'Inzecca, across the same tectonic units described in Transect-2. The basement section was already studied by Garfagnoli et al. (2009). Its structural architecture is dominated by a penetrative sub-vertical  $D_1$  plano-linear fabric with formation of S-L tectonites that almost completely obliterate the primary igneous fabric in both the Hercynian granitoids and the Permian volcanoclastics (Fig. 5a). The  $S_1$  foliation strikes NNW-SSE, dipping steeply either to ENE or WSW (mean: N153°, 83°; n=52), and bears dip-parallel L<sub>1</sub> stretching lineations (mean: N252°, 81°; n=42; Figs. 5b), dominantly made of Qz-Wm associations in gneiss and Ab-Ep in volcanoclastics. A gneissic texture is well evident in the granitoid rocks, defined by Qz-Fsp porphyroblast embedded within Wm folia. In section normal to foliation and parallel to the stretching lineations, cm-sized Qz and Fsp porphyroclasts systems dominantly show phi-type geometries and both up- and down-dip kinematic criteria (dominantly provided by sigma-type clasts) are present, attesting dominant coaxial stretching during formation of the composite  $S_1$ -L<sub>1</sub> fabric (Figs. 5c-d). In the Permian volcanoclastics, the  $D_1$  fabric consists of  $S_1$ -L<sub>1</sub> tectonites that overprint the primary layering. Vertical stretching is documented by L<sub>1</sub>, dip-parallel stretching lineation as provided by Qz-Pl-Ep associations, boudinage and nearly horizontal quartz veining. The  $S_1$  foliation is axial planar to subvertical isoclinal folds with sub-horizontal hinge lines, trending ca. NS (Figs. 5b-g). Various generations of quartz veins are recognized, with early segregated veins

289 that are transposed along the  $S_1$  foliation. A spaced  $S_2$  crenulation foliation is observed to refold  
 290 the  $S_1$  foliation. The  $S_2$  strikes ca. N-S and dips shallowly to the E (Fig. 5b). As documented by the  
 291 decrease in the  $S_2$  spacing, the intensity of the  $S_2$  crenulation increases when moving to the E,  
 292 towards the contact with the Schistes Lustrés Complex (Fig. 5a, h)

293

294 **5. Sample microtexture and petrography**

295 Microstructures, petrography and mineral chemistry of representative samples collected  
 296 along the three investigated samples are described below. Further details on microstructures are  
 297 provided in Supplementary Material#1. Mineral chemistry as obtained from electron microprobe  
 298 analyses (EMPA), and the recalculation of the mineral formulas are provided in the Supplementary  
 299 Material#2.

300

301 **5.1 Transect-1**

302 Sample CO24 is representative of the  $S_1$  fabric in the Permian volcanics (Fig. 3a, 3d-c).  
 303 The sample microfabric is characterized by a penetrative disjunctive foliation, defined by the syn-  
 304 kinematic assemblage made of aligned Wm (up to 40% vol.) and fine-grained re-crystallized Qz (in  
 305 higher strain domains), Ab,  $\pm$  Stp  $\pm$  Rt, which envelopes up to mm-sized Qz and Fsp porphyroclasts  
 306 (Fig. 6a, 7a). Fracturing of Qz-Fsp porphyroclasts is commonly observed with fracture sealing  
 307 largely operated by recrystallized Qz  $\pm$  Wm. Residual igneous microstructures are commonly  
 308 observed, as documented by preserved twinning in Kfs, oscillatory growth zoning in Pl and  
 309 euhedral shapes of the Qz-Fsp grains. Pristine igneous quartz grains show undulatory extinction  
 310 and evidence of dynamic recrystallisation, dominantly assisted by bulging recrystallisation. Post-  
 311 tectonic growth of Cb (ca. 1-2% vol.) is also commonly documented (Supplementary Material#1).  
 312 The Wm (n=36) composition is characterized by Si ranging 3.34-3.49 atoms per formula unit  
 313 (apfu), corresponding to  $X_{\text{Ms}} = 0.41-0.57$ ,  $X_{\text{Cel}} = 0.37-0.51$ ,  $X_{\text{Pl}} < 0.10$ ,  $X_{\text{Pg}} < 0.11$  (Fig. 8a, d-e;  
 314 Supplementary Material#2).

315 Sample CO25 is a  $D_2$  S-C tectonite, representative of the progressive shear strain localization  
 316 in the Permian volcanics (Table 1; Fig.3a, e). At the thin section scale, the syn-metamorphic  
 317 fabric is transpositive and characterized by a significant increase in Wm abundance (up to 70 vol%,  
 318 associated with a very fine-grained (average 10  $\mu\text{m}$ ) matrix made of recrystallized Qz (Fig. 6b). Shear  
 319 sense criteria are provided by oblique foliation, sigma-type Fsp porphyroclasts and S-C fabrics and  
 320 systematically indicate a top-to-the-W sense of shear (Fig. 6b). The metamorphic assemblage is

321 completed by Chl (ca. 10 %vol), Ab, Ep, Stp, Ttn, Ap (< 5% vol). Stp is observed as mostly unoriented  
 322 clusters of elongated crystals and along the  $S_1$  foliation. Chl form late clusters in association with  
 323 Ttn, Ep, Ap, often forming pseudomorphic replacement at the expenses of former igneous grains  
 324 (Fig. 7b). Post-tectonic growth of Cb is also observed. The composition of the syn-tectonic Wm  
 325 ( $n=30$ ) shows Si ranging 3.34-3.51 apfu, corresponding to  $X_{Ms} = 0.47-0.64$ ,  $X_{Cels} = 0.34-0.51$ ,  $X_{Pril} < 0.02$ ,  
 326  $X_{Pg} < 0.05$  (Fig. 8d-e). The composition of Stp is characterized by  $X_{Mg} = 0.13$  and  $X_{Fe^{3+}}$   
 327  $[(Fe^{3+}/(Fe^{3+}+Fe^{2+})] = 0.35$ . Ep shows  $X_{Ps} [Fe^{3+}/(Fe^{3+}+Al^{3+})] = 0.35$  with  $Mn^{3+}$  0.03 apfu, and Chl is  
 328 characterized by Si ranging 2.76-2.91 apfu and XMg between 0.23-0.27 (Supplementary Material#2).

329 Samples CO38 and CO55 are protomylonites, representative of the ductile shear strain  
 330 localization in the Hercynian granitoid basement (Table 1; Fig. 3a). At thin section scale, sample  
 331 microtextures are characterized by a network of anastomosing array of inter- and intra-grain  
 332 fracture network affecting the igneous Fsp-QZ matrix, coexisting with spaced bands (up to 150  $\mu m$   
 333 in thickness) of ductile shear strain localization (Fig. 6c). The crack-filling mineral assemblage  
 334 dominantly consists of Qz  $\pm$  Wm  $\pm$  Stp and late Cb (Fig. 7c). The vein selvage is made of Bt-Chl-Ttn  
 335  $\pm$  Cb, Amp, Ep, Ab, Ap associations. Quartz in veins either preserve fibrous textures or document  
 336 evidence of dynamic recrystallization and grain size reduction, primarily assisted by bulging  
 337 recrystallisation. Igneous quartz exhibits undulose extinction, deformation bands, sub-grain  
 338 formation and core-mantle structures indicative of subgrain rotation recrystallisation (Fig. 6c;  
 339 Supplementary Material#1). Replacement of igneous Mag by the assemblage made of  
 340 stilpnomelane-amphibole-epidote-titanite  $\pm$  ilvaite after igneous magnetite is also observed (Fig.  
 341 7d). The ductile shear bands are defined by anastomosed fine-grained recrystallized Qz in  
 342 association with Wm  $\pm$  Stp (Fig. 6c). The Wm is entirely syn-kinematic and commonly oriented  
 343 parallel to the mylonitic foliation (Fig. 6c). It occurs in two generations: (i) the Wm1 ( $n=6$ ),  
 344 represented by a minor cluster of cores with lower Si (3.26-3.33 apfu) corresponding to  $X_{Ms} = 0.49-$   
 345  $0.61$ ,  $X_{Cels} = 0.27-0.34$ ,  $X_{Pril} < 0.17$ ,  $X_{Pg} < 0.01$ ; and (ii) the Wm2 ( $n=14$ ), forming rims of Wm1 and  
 346 main foliation, which show higher Si (3.35-3.50 apfu) and corresponding to  $X_{Ms} = 0.38-0.60$ ,  $X_{Cels} =$   
 347  $0.36-0.50$ ,  $X_{Pril} < 0.11$ ,  $X_{Pg} < 0.02$  (Fig. 8d-e; Supplementary Material#2). The Stp composition is  
 348 characterized by  $X_{Mg} = 0.24-0.33$  and  $X_{Fe^{3+}} = 0.38-0.45$  apfu. Chl shows  $X_{Mg} = 0.20$  and Bt is  
 349 characterized by  $TiO_2 = 0.55-0.92$  wt% with  $X_{Mg} = 0.24-0.25$ . The Amp shows low  $Al_2O_3$  (1.07-1.29  
 350 wt.%), low  $CaO$  (6.38-7.09 wt%), high  $FeO^t$  (20.99-21.04 wt%) and  $Na_2O$  (3.19-3.31 wt.%),  
 351 belonging to the sodic-calcic group with a chemical composition corresponding to Wnc  
 352 (Hawthorne et al., 2012) (Supplementary Material#2).

353

354 **5.2 Transect-2**

355 Sample CO35 is from a fractured granitoid (Table 1). The fracture network is dominantly  
 356 inter-grain, with up to 0.5 cm alteration halos, making up to 30% vol. of rock. The fracture filling is  
 357 dominantly made of Qz-Wm, with associated Stp-Ep-Amp-Ttn-Ab + Grt, Ap. Two generation of  
 358 metamorphic Wm are documented both in the metamorphic matrix and as vein segregation (Fig.  
 359 7e). Wm1 (n=8) represents cores showing low Si (3.05-3.29 apfu) and corresponding to  $X_{Ms} = 0.68-$   
 360  $0.89$ ,  $X_{Cel} = 0.06-0.29$ ,  $X_{PrI} < 0.02$ ,  $X_{Pg} < 0.03$ . The Wm2 (n=19) consists of rims and overgrowth,  
 361 fracture filling and main foliation. Wm2 has higher Si (3.41-3.59 apfu) corresponding to an increase  
 362 of celadonite compound:  $X_{Ms} = 0.40-0.56$ ,  $X_{Cel} = 0.42-0.59$ ,  $X_{PrI} < 0.02$ ,  $X_{Pg} < 0.02$  (Fig. 8d-e;  
 363 Supplementary Material#2). Metamorphic Ep is observed to rim early igneous All and Mag, in  
 364 association with Grt and late Amph (Figs. 7f). Ep shows  $Fe^{3+}$  ranging 0.89-1.19 apfu and  $Mn^{3+}$  0.01-  
 365 0.04, respectively, corresponding to  $X_{Ps} = 0.30-0.40$ . Grt is essentially an Adr-Grs ( $Adr_{55-78}Grs_{22-38}$ )  
 366 solid solution. The low Si content and low total indicate the presence of hydrogarnet component.  
 367 Stoichiometric constraints result in 5 to 10% of  $SiO_4$  tetrahedra being replaced by  $(OH)_4$ . The Amp  
 368 chemistry corresponds to Na-Amp (Rbk; Supplementary Material#2)

369 Sample CO36 is representative of the D2 mylonitic shear fabrics in the Hercynian granitoids  
 370 (Table 1; Fig. 4). The syn-tectonic mineral assemblage consists of Qz-Wm-Stop-Ep, Ttn, Ab. Texturally  
 371 late fibrous Amp crystallization and post-tectonic Cb growth are also observed. The microtexture is  
 372 dominated by a fine-grained aggregate of recrystallized Qz grains (up to 40% vol.), associated with  
 373 syn-tectonic Wm that wrap around and rim Qz-Fsp porphyroclasts and crenulated Wm microlithons  
 374 (Fig. 6d). Fsp grains are extensively affected by intragranular fractures that are filled by recrystallized  
 375 quartz. Relic igneous quartz grains show evidence of pronounced undulose extinction, distinct  
 376 subgrains and core-mantle structures indicative of subgrain rotation recrystallisation  
 377 (Supplementary Material#1). Shear senses are dominantly provided by oblique foliation and sigma-  
 378 type Fsp-Qz porphyroclasts, systematically pointing to top-to-the-W shearing (Figs 6d-e). Similarly  
 379 to sample CO-35, two generations of metamorphic Wm is commonly observed (Fig 7g-h). The Wm1  
 380 (n=11) forms the cores showing low-Si (3.02-3.32 apfu) and corresponding to a muscovitic  
 381 composition ( $X_{Ms} = 0.62-0.90$ ,  $X_{Cel} = 0.03-0.32$ ,  $X_{PrI} < 0.02$ ,  $X_{Pg} < 0.12$ ) (Fig. 8a-b). The Wm2 (n=26)  
 382 overgrowths Wm1 and defines the main foliation. The Wm2 shows higher Si (3.35-3.58 apfu),  
 383 corresponding to  $X_{Ms} = 0.39-0.62$ ,  $X_{Cel} = 0.36-0.58$ ,  $X_{PrI} < 0.04$ ,  $X_{Pg} < 0.01$  (Fig. 8b, d-e; Supplementary  
 384 Material#2). The Stp composition is characterized by  $X_{Mg} = 0.31-0.36$  and  $X_{Fe^{3+}} = 0.41-0.47$  apfu

385 (Supplementary Material #2c). Epidote is characterized by high Fe<sup>3+</sup> (0.75-0.95), with X<sub>Ps</sub> = 0.25-0.32.  
 386 The Amp corresponds to Act compositions (Supplementary Material#2).

387

388 **5.3 Transect-3**

389 Sample CO42 is representative of the D<sub>1</sub>-D<sub>2</sub> composite fabric in the Hercynian granitoids  
 390 (Table 1; Fig. 5). The sample microfabrics is dominated by a continuous foliation (S<sub>1</sub>) made of  
 391 alternating fine-grained recrystallized Qz grains and Wm folia that envelop fractured Fsp and  
 392 highly strained Qz porphyroblast systems (Fig. 6f). Early igneous quartz grains show evidence of  
 393 pronounced internal strain and recovery, as documented by ondulose extinction, deformation  
 394 bands and subgrain formation. Dynamic recrystallisation is dominantly documented by core-and-  
 395 mantle structures, defined by fine-grained quartz aggregates surrounding large relic quartz grains  
 396 produced by sub grain rotation recrystallisation (Supplementary Material#1). Shear sense  
 397 indicators are not univocal, confirming the dominant coaxial nature of D<sub>1</sub> deformation as observed  
 398 at the mesoscale (Fig. 5c). Igneous textures are locally preserved. The syn-tectonic mineral  
 399 assemblage consists of Wm-Qz- Ab-Stop-Amp + Ep, Ttn, and Ap. Late Cb growth is also observed  
 400 (Fig. 7i). Wm composition (n= 66) is characterized by Si ranging 3.47-3.61 apfu, corresponding to  
 401 X<sub>Ms</sub> = 0.26-0.45, X<sub>Cel</sub> = 0.47-0.61, X<sub>Prl</sub> <0.13 and negligible XPg (<0.01) (Figure 8c-d; Supplementary  
 402 Material#2). Stop shows X<sub>Mg</sub> = 0.25-0.41 and X<sub>Fe<sup>3+</sup></sub> = 0.35-0.48. Ep shows X<sub>Ps</sub>=0.14-0.19 with Mn<sup>3+</sup> <  
 403 0.02 apfu. A two-stage Amp crystallization is documented, with Ca-Na-Amph (Wnc) replacing early  
 404 segregated Na-Amp (Rbk) (Supplementary Material#2).

405

406 **6. Metamorphic Thermobarometry**

407 The thermo-baric environment during syn-metamorphic deformation of the Hercynian  
 408 basement of Corsica was assessed through phase equilibria (pseudosection) modelling by using  
 409 the software Perple\_X (Connolly, 2005; <https://www.perplex.ethz.ch/>, version 6.9.1 updated on  
 410 March 07 2022). We used the bulk composition of samples CO24, CO36 and CO42, which are  
 411 considered representative of the different textures associated with development of the composite  
 412 D<sub>1</sub>-D<sub>2</sub> fabric along the three investigated transects (Fig. 2). The bulk sample compositions were  
 413 simplified to the Na<sub>2</sub>O–CaO–K<sub>2</sub>O–FeO–MgO–Al<sub>2</sub>O<sub>3</sub>–SiO<sub>2</sub>–H<sub>2</sub>O–TiO<sub>2</sub>–O<sub>2</sub> (NCKFMASHTO) system by  
 414 removing MnO (0.01-0.05 wt%) and correcting CaO for the presence of apatite and post-tectonic  
 415 calcite (up to 1-2 % vol. in some samples). This procedure completely removes CaO from sample  
 416 CO24, and only leaves small amounts of CaO in samples CO36 and CO42 (Table 2). We adopted the

417 hp633ver.dat thermodynamic dataset (Holland & Powell, 2011; 2018), and the following solid  
 418 solution models as described in the file solution\_model.dat: Bi(W) for biotite, Chl(W) for chlorite,  
 419 Mica(W) for white mica (White et al., 2014), Ep(HP11) for epidote (Holland & Powell 2011);  
 420 cAmph(G) for clinoamphibole (Green et al., 2016), feldspar for ternary feldspar (Fuhrman &  
 421 Lindsley, 1988), Sp(WPC) for spinel (White et al., 2002), Pu for pumpellyite, and Stlp for  
 422 stilpnomelane. Quartz, ilmenite, rutile, and titanite were considered as pure phases. The fluid  
 423 phase was considered as pure H<sub>2</sub>O and considered to be present in excess.

424 We are aware that solid solution models for complex minerals such as mica or amphibole  
 425 are poorly known at low T, with particular reference to the role of Fe<sup>3+</sup> content in silicate minerals.  
 426 For stilpnomelane solid solution model, ferric iron is not even considered. In case of amphiboles,  
 427 the applied solid solution model fails to predict the analyzed compositions in the considered P-T  
 428 range, except for riebeckite. As further complication, the contents of Fe<sup>2+</sup> and Fe<sup>3+</sup> in minerals are  
 429 not directly analyzed but calculated from microprobe analyses based on stoichiometric  
 430 constraints, and are probably of low precision, particularly for white mica, stilpnomelane, and  
 431 amphibole. In order to estimate the contents of ferric iron of the whole rock compositions, for  
 432 samples Co36 and Co42 we calculated T-Fe<sub>2</sub>O<sub>3</sub> pseudosections (at constant P (0.6 GPa, see below);  
 433 Supplementary Material#3). Bearing in mind the above-mentioned uncertainties, we consider the  
 434 results of the thermodynamic modelling as semi-quantitative.

435

#### 436 **6.1 Sample CO24**

437 Sample CO24 is representative of the thermo-baric environment leading to development of  
 438 S<sub>1</sub> foliation in the volcanoclastic covers (Figs. 2, 3a, c-d). The mineral assemblage defining the S<sub>1</sub>  
 439 foliation consists of Qz-Wm + Stp +Rt, which defines a P-T field restricted by the stability of Stp  
 440 that is limited to high temperature by the Bt-in isograd and to high-pressure by the Stp-out  
 441 isograds, respectively. Considering the isopleths as defined by the Si content in Wm (3.39-3.49  
 442 apfu), the corresponding thermobaric environment is constrained at ca. 0.5-0.6 GPa and T< 350 °C  
 443 (Fig. 9a).

444

#### 445 **6.2 Sample CO36**

446 Sample CO36 refers to the D2 progressive shear strain localization in the continental  
 447 basement (Figs. 2, 4). The syn-tectonic mineral assemblage is made of Qz-Wm-Stop-Ep-Ttn-Ab.  
 448 Choosing a sectioning value of 0.6 GPa, pseudosection modelling in the T-Fe<sub>2</sub>O<sub>3</sub> space indicates

449 that a low  $\text{Fe}_2\text{O}_3$  content <0.1 wt.% is required for the stability of the above assemblage. The  
 450 temperature range is limited between ca. 300-370 °C, as imposed by the lack of Bt and Pmp in the  
 451 metamorphic assemblage (Supplementary Material#3). A value of  $\text{Fe}_2\text{O}_3= 0.1$  wt% is therefore  
 452 considered to construct the P-T pseudosection. Results show that the syn-tectonic metamorphic  
 453 assemblage made of Wm-Ep-Stop-Ttn occurs within a narrow P-T field of  $P=0.45-0.65$  GPa and  $T$  of  
 454 ca. 300-330°C, as constrained by the absence of Amp at high-pressure and absence of Pmp at  
 455 lower temperature and Bt at higher temperature, respectively (Fig. 9b).

456

### 457 **6.3 Sample CO42**

458 Sample CO42 is representative of the development of the  $D_1$  fabric in the continental  
 459 basement (Figs. 2, 5). The syn-tectonic mineral assemblage is made of Qz-Wm-Stop-Ep ± Amp, Ttn,  
 460 Ab. The pseudosection modelling in the  $T-\text{Fe}_2\text{O}_3$  space at constant  $P$  of 0.6 GPa shows that the Stop-  
 461 Amp-Ep assemblage is stable for  $0.3 < \text{Fe}_2\text{O}_3 < 0.9$  wt% at temperatures below 350°C, limited by  
 462 occurrence of Bt in the metamorphic assemblage at higher temperature and Ep at lower  
 463 temperature, respectively (Supplementary Material#3). A value of  $\text{Fe}_2\text{O}_3= 0.6$  wt% is chosen to  
 464 construct the P-T pseudosection. Considering the Si isopleths in Wm for this sample (Si apfu  
 465 ranging 3.50-3.60) and absence of Bt in the metamorphic assemblage, results constrain formation  
 466 of the  $S_1$  foliation at  $P=0.5-0.7$  GPa and  $T$  of ca. 300°C (Fig. 9c).

467

## 468 **7. $^{40}\text{Ar}$ - $^{39}\text{Ar}$ Geochronology**

469 Laser in-situ analyses were completed on the samples used for pseudosection modelling.  
 470 White mica of sample CO24 (Transect-1) yielded a significant age interval (Fig. 10), in the range of  
 471  $37.6\pm0.5$  Ma to  $43.6\pm0.4$  Ma. Some older ages, up to ~50 Ma may be due to contamination by K-  
 472 feldspar, which yielded ages older than 100 Ma where unequivocally identified (Supplementary  
 473 Material#4). The five younger ages define a weighted mean of  $38.0\pm0.2$  Ma. White mica from  
 474 sample CO36 (Transect-2) gave a younger age interval when compared to white mica from  
 475 Transect-1, ranging from  $32.5\pm0.2$  Ma to  $37.8\pm0.3$  Ma. A slightly older age ( $43.2\pm1.8$  Ma) is  
 476 affected by a large uncertainty due to the low gas yield, likely due to contamination by a low K  
 477 phase(s). The first youngest peak in the cumulative plot distribution (Fig. 10) is defined by three  
 478 analyses, yielding a weighted mean age of  $33.3\pm0.2$  Ma. Sample CO42 (Transect-3) gave white-  
 479 mica ages mainly within  $38.6\pm0.4$  to  $48.9\pm0.3$  Ma. Some older ages, as old as ~56-60 Ma,  
 480 analogously to samples CO24, maybe due to contamination by K-feldspar.

481

482 **8. Discussion**

483 The Alpine tectono-metamorphic evolution reconstructed at the footwall of the ADF is  
 484 dominated by development of a low-grade, composite D<sub>1</sub>-D<sub>2</sub> ductile plane-linear fabric,  
 485 characterized by the pervasive development of S-L tectonites that transpose the primary fabrics in  
 486 the Hercynian granitoid basement and the Permian-Triassic volcanoclastic cover.

487 The D<sub>1</sub> deformation is dominantly attested by formation of a panel of N-S striking  
 488 subvertical S<sub>1</sub> foliation, sub-parallel to the ADF, and bearing dip-parallel L<sub>1</sub> stretching lineations.  
 489 Locally, deformation partitioning is documented during development of the D<sub>1</sub> fabrics when  
 490 moving from the Permian volcanoclastic into the granitoid basement, where conjugate sets of  
 491 subvertical NE-striking dextral and SE-striking sinistral mylonitic zones are observed to  
 492 accommodate the D<sub>1</sub> deformation (see also Di Vincenzo et al., 2016; Fig. 3b). Overall, the D<sub>1</sub> finite  
 493 strain documents pure shear dominated deformation fabrics recording subvertical stretching in  
 494 response to an E-W directed maximum shortening direction. A continuum of deformation is  
 495 attested by the progressive overprinting of the quartz veins that, formed orthogonally to the L<sub>1</sub>  
 496 stretching direction, are shortened and folded along the S<sub>1</sub> foliation and later overprinted by new  
 497 vein generations (Figs. 3c and 5f-h). The D<sub>2</sub> deformation overprints the D<sub>1</sub> fabric in a general  
 498 regime of simple shear, associated with development of E-dipping foliations and ductile shear  
 499 zones, accommodating a general top-to-the-W tectonic sense of transport both in the granitoid  
 500 basement and the Permian volcanoclastic cover. The intensity of the D<sub>2</sub> deformation increases  
 501 westward approaching the ADF, suggesting a tectonic linkage with the overthrusting of the Alpine  
 502 Corsica Domain onto the Hercynian Corsica.

503 When integrated with the available literature data (Garfagnoli et al., 2009; Di Rosa et al.,  
 504 2020a; Malasoma et al., 2006; 2020), the structural data collected in this study point to a  
 505 continuum of ductile deformation during the Alpine basement-involved thrusting in the Hercynian  
 506 Corsica. Shortening in the continental crust was first accommodated by (i) pure-shear dominated  
 507 strain at deeper crustal levels and then (ii) top-to-the-W shear strain localization, evolving from  
 508 ductile shearing to brittle overthrusting at shallower crustal conditions. Top-to-the-W thrusting  
 509 involved also the Mesozoic and Cenozoic cover units (see also Di Rosa et al., 2019; 2020a; this  
 510 study).

511

512 **8.1 Metamorphic environment and deformation conditions**

513 Low-T conditions during the progression of the D<sub>1</sub>-D<sub>2</sub> deformation makes the assessment of  
514 the corresponding thermo-baric environment through thermodynamic modelling challenging.  
515 However, considering (i) the occurrence of Stlp and the absence of Bt in the main syn-tectonic  
516 assemblage, which limit the thermal peak to < 400°C; and (ii) the Si-in-Ph isopleths as proxy of the  
517 burial pressure, we can conclude that Alpine deformation/metamorphism occurred at ca. 0.5-07  
518 GPa and 330-370 °C (Fig. 9). These P-T estimates are in good agreement with those obtained by Di  
519 Vincenzo et al. (2016), thus providing a consistent picture of the tectono-metamorphic overprint  
520 of Hercynian Corsica at the footwall of the ADF. The restricted Wm composition imposes a cooling  
521 exhumation path, similarly to what reconstructed for the ETSZ (Maggi et al., 2012). Similar along-  
522 strike peak P conditions are reconstructed at the footwall of the ADF, where progressive burial and  
523 exhumation cooling can be proposed for the Hercynian basement of western Corsica (Fig. 9).

524 Considering an average rock density of 2700 kg/km, the peak P-T conditions recovered  
525 from the continental basement of Corsica conform to a paleo-geothermal gradient of ca. 11°C/km,  
526 typical of the low geotherm in active and fossil convergent plate margins (Penniston-Dorland et  
527 al., 2015; Agard et al., 2018). When the P-T estimates are compared with those available from  
528 literature, it is evident that the Corsica basement was equilibrated at shallower depths according  
529 to a warmer geothermal gradient with respect to the Mesozoic cover rocks (Di Rosa, 2019) and the  
530 metamorphic units of the Tenda Massif (Molli et al., 2006; Maggi et al., 2012; Rossetti et al., 2015),  
531 but recorded a similar cooling exhumation trajectory at lower pressures (Fig. 11)

532 The low-T deformation environments reconstructed through thermodynamic modelling are  
533 in line with the microtextural evidence of the studied samples, which documents, regardless of the  
534 strain intensity and fabric type (either D<sub>1</sub> or D<sub>2</sub>), brittle deformation in feldspar as opposed to  
535 ductile flow and fine-grained dynamic recrystallisation in quartz (Fig. 6 and Supplementary  
536 Material#1), and white mica crenulation. Dynamic recrystallization in quartz was dominantly  
537 assisted by bulging grain boundary (BLG) and subgrain rotation (SGR) recrystallization in the  
538 highest strain domains (sample CO36 and CO42), compatible with environmental temperatures at  
539 the transition between the BLG and SGR zones, at about 400 ±30 °C (Stipp et al., 2002). Taken  
540 together, these microtextural constraints attest that ductile processes were not activated in Fsp  
541 and deformation temperatures were well below 400-450 °C (e.g., O'Hara, 1990; Passchier & Trow,  
542 2010).

543 At such low-T conditions, structurally controlled fluid flow and fluid-mediated deformation  
544 promoted metamorphic recrystallization and rheological weakening of the Corsica basement

545 during the low-grade Alpine tectono-metamorphic evolution. Significantly, brittle precursor  
546 localized the ductile shearing in the basement units, as documented by the field and microtextural  
547 evidence of extensive fracturing and veining associated with development of the Alpine tectono-  
548 metamorphic fabric (Fig. 3h, 5f-h; .6a, c, e, f), providing further evidence of ductile strain  
549 localization initially controlled by brittle behavior of granitoid rocks (Mancktelow and  
550 Pennacchioni 2005; Fusseis and Handy, 2008; Sarkar et al., 2020). In particular, formation of Ph-  
551 rich bands of deformation and mylonites (Fig. 6) documents that fracturing of feldspar followed by  
552 fluid-assisted breakdown to white mica was the dominant process leading to reaction softening  
553 and shear strain localization in the Corsica basement (e.g., Wintsch et al., 1995; Gueydan et al.,  
554 2003; Holyoke and Tullis, 2006; O'Hara, 2007).

555 A relatively high water/rock ratio during progress of the D<sub>1</sub>-D<sub>2</sub> tectono-metamorphic  
556 evolution can be deduced by a general hydration of the granitoid basement rocks, with the diffuse  
557 blastesis of Ph-Amp-Ep associations. Further evidence of fluid-rock interaction is provided by the  
558 occurrence of secondary Ca-rich mineral assemblages (Adr-rich garnet, epidote, Ca-amphibole,  
559 ilvaite and late carbonates), which indicate intensive alteration of the early magmatic  
560 assemblages (Cpx - Mag) in the basement rocks by the chemically reactive infiltrating fluids and  
561 variable redox conditions (e.g., Barton & Berger, 1984; Delgado Martín & Soleri Gil, 2010 ).

562 Similarly to other studies dealing with formation of microstructures during mylonitization  
563 of granitoid precursors, the fluid-rock interactions, reaction weakening and partitioning of  
564 deformation are recognized key elements for strain softening and localization during shear zone  
565 nucleation and development (e.g., Janecke and Evans, 1988; O'Hara, 1990, 2007; Wintsch et al.,  
566 2005, 2007; Johnson et al., 2008; Goncalves, 2012; Maggi et al., 2014; McAlleer e al., 2017;  
567 Papeschi & Musumeci, 2019).

568

569

## 570 **8.2 Age of crustal shortening**

571 Based on the P-T estimates and microtextural evidence, deformation in the investigated  
572 samples developed under temperature conditions insufficient to alter by volume diffusion the Ar  
573 isotope record of white mica. In fact, several field-based studies have documented that Wm can  
574 preserve crystallization ages up to at least ~500 °C (e.g. Di Vincenzo et al. 2004; Augier et al. 2005;  
575 Villa et al. 2014). Given that the strongly peraluminous character of the investigated rock samples  
576 does not represent a primary feature of the igneous protoliths (Di Vincenzo et al., 2016), the <sup>40</sup>Ar-

577  $^{39}\text{Ar}$  ages from Wm record the time of (re)-crystallization during fluid-assisted deformation. Both  
578 samples CO24 (Transect-1) and CO42 (Transect-3) are characterized by deformation features  
579 representative of the D<sub>1</sub> fabric, by Wm with phengitic compositions and by the lack of muscovitic  
580 Wm relicts. Even excluding ages older than ~44 Ma in sample CO24 and ~47 Ma in sample CO42,  
581 our results extend back the development of Alpine syn-deformational phengitic white mica and  
582 consequently crustal shortening of western Corsica to the early Lutetian (at ca. 48 Ma). Sample  
583 CO36 from transect-2, is dominated by the D<sub>2</sub> progressive shear deformation and mainly yielded  
584 Priabonian ages. This sample is however characterized by the occurrence of two Wm generations,  
585 a dominant phengitic Wm2 aligned along the main D<sub>2</sub> foliation and rare muscovitic relicts  
586 representing syn-burial remnants. A possible explanation for this apparent inconsistency is that  
587 either (1) data record a Priabonian burial or, more likely, (2) muscovitic relicts were coincidentally  
588 not sampled during data collection. Following hypothesis (2),  $^{40}\text{Ar}$ - $^{39}\text{Ar}$  data constrain the  
589 development of the D<sub>2</sub> deformation to the Priabonian (ca. 33-38 Ma) and the last increments of  
590 syn-D<sub>2</sub> shearing to not earlier than the Priabonian-Rupelian transition.

591 Ages older than the Bartonian, have been previously reported for phengitic Wm of the  
592 Tenda Massif and the Schistes Lustrés Unit (Monte Pinatelle area) by Brunet et al. (2000). More  
593 recently, Maggi et al. (2012) reported two Ypresian nominal ages from two poorly-defined U-Pb  
594 isochrons using synkinematic rutile fractions and acmite, phengite and oxide-sulfide coating  
595 derived from blueschist-facies top-to-the-W phyllonitic shear bands within the East Tenda Shear  
596 Zone (Maggi et al., 2012; Fig. 1). Maggi et al. (2012) assigned the excess of scatter in the data  
597 arrays to secondary disturbance. On the other hand, the deformation ages recovered in this study  
598 only partially overlap with the U-Pb zircon and Lu-Hf garnet and lawsonite ages as derived from  
599 eclogites of the Schistes Lustrés, which provided Prabonian-Rupelian ages (ca. 34-37 Ma; Martin et  
600 al., 2011; Vitale Brovarone and Herwartz, 2013).

601

602

### 603 **8.3 Tectonic reconstruction**

604 Our petrotectonic reconstruction frames convergent deformation in the Western Corsica  
605 basement during the Eocene-Oligocene. We provide evidence that pure shear dominated  
606 deformation of the Corsica basement predated simple shear strain localization. During early-  
607 middle Eocene times (ca. 50 to 40 Ma), the Hercynian continental crust was first homogenously  
608 shortened during development of a steeply dipping high strain deformation zone in response to a

609 roughly E-W directed maximum compression direction ( $D_1$ ). Top-to-the-W ductile shearing ( $D_2$ )  
610 occurred later, with the last shear increments during the early Oligocene at ca. 32-33 Ma,  
611 synchronous with activation of the syn-blueschist, top-to-the-W reverse shearing along the ETSZ  
612 (Rossetti et al., 2015). Therefore, the coupling between the different tectonic units of the Alpine  
613 orogen in Corsica occurred nearly synchronously during the late Eocene-early Oligocene (34-32  
614 Ma) and in a restricted P-T interval (ca. 0.5-07 GPa and 300-400°C; Fig. 11), when the deepest and  
615 cooler units of the Schistes Lustrés were exhumed at shallower crustal conditions, overthrust and  
616 tectonically assembled along the ETSZ onto the W Corsica basement. At this stage, the Alpine  
617 shortening was accommodated through non-coaxial shearing and W-directed thrusting along the  
618 entire Alpine orogenic system of Corsica, propagating westward across the basement complex.  
619 The final tectonic coupling caused formation of a late Eocene-early Oligocene, W-verging nappe  
620 stack, characterized by an inverted sequence of metamorphic units (from top to bottom:  
621 blueschist- to eclogite-facies Schistes Lustrés, blueschist-facies Tenda Massif, and greenschist-to-  
622 blueschist-facies Western Corsica basement) bounded by major, crustal-scale top-to-the-W shear  
623 zones, equilibrated under low-grade HP greenschist (W Corsica) to blueschist facies (ETSZ)  
624 metamorphic conditions, respectively. The composite Alpine ductile  $D_1/D_2$  fabric in the Corsica  
625 basement is truncated by brittle thrusts, related to the later thick-skinned thrusting involving the  
626 basement and cover units during continuous shortening (Bezert and Caby, 1988; Rossi et al., 1994;  
627 Di Rosa et al., 2020a; Frassi et al., 2022; this study). Transition from orogenic construction to post-  
628 orogenic extensional thinning in Corsica occurred during the late Oligocene-early Miocene, as  
629 documented by the extensional reactivation of the ETSZ (Rossetti et al., 2015).

630 When integrated at regional scale, the P-T-t-deformation history as reconstructed from the  
631 metamorphic units of the Alpine orogen in Corsica has significant implications as to the timing of  
632 the subduction zone metamorphism and the tectonic/geodynamic evolution along the Mesozoic-  
633 Cenozoic active margin developed during convergence of the African and European plates (see  
634 also Vitale Brovarone and Herwatz, 2013). Paleotectonic reconstructions frame the Alpine  
635 orogeny in Corsica either as the southward prosecution of the Western Alps governed by  
636 southeast-dipping (“Alpine”) subduction (e.g., Doglioni et al., 1998; Molli & Malavieille, 2010;  
637 Handy et al., 2010; Carminati et al., 2012; Marroni et al., 2017) or as the retrograde tectonic  
638 accretion above the backstop of the accretionary wedge produced by the north-dipping  
639 (“Apennine-Maghrebian”) subduction (Principi and Treves, 1984; Jolivet et al., 1998; Jolivet &  
640 Faccenna, 2000; Faccenna et al., 2001; 2004; Rossetti et al., 2004; Lacombe & Jolivet, 2005; Vitale

641 Brovarone & Hervatz, 2013; van Hinsbergen et al., 2014; Bestani et al., 2016; Jolivet et al., 2021).  
642 The first scenario involves a subduction flip during the Cenozoic, with the early structured Alpine  
643 belt passively overthrust onto the growing Apennine-Maghrebian orogenic wedge, whereas the  
644 second scenario considers a continuous northward subduction in Cenozoic times. In both  
645 configurations, the Oligocene-Miocene geodynamics is controlled by the Maghrebian-Apennine  
646 slab roll-back and crustal thinning in the back-arc domain.

647 Eocene-Oligocene orogenic metamorphism in the Corsica basement (from ca. 50 to 32 Ma)  
648 broadly overlaps (i) with the age of the orogenic metamorphism affecting both the oceanic- and  
649 continental-derived units in the hinterland of the Maghrebian-Apennine accretionary wedge, as  
650 documented in Calabria (ca. 50-35 Ma; Schenk, 1980; Rossetti et al., 2001a; 2004; Heymes et al.,  
651 2010), in the Alboran Domain of the Betic-Rif belt (ca. 50-40 Ma; Augier et al., 2005; Li and  
652 Massonne, 2018; Marrone et al., 2021a, b; Bessiere et al., 2022), and the Eastern Kabylia region  
653 (ca. 32-21 Ma; Bruguier et al., 2017); and (ii) with the oldest calcalkaline magmatism in Provence,  
654 Sardinia, and Alboran Domain, showing Bartonian-Rupelian ages (ca. 40–32 Ma; Lustrino et al.,  
655 2009; 2017) (Fig. 1). The Apennine-Maghrebian subduction was thus active since at least Eocene  
656 times, a time span compatible with efficient subduction slab retreat and the Oligocene-Miocene  
657 back-arc opening of the Liguro-Provençal, Alboran, and Tyrrhenian basins (e.g., Doglioni et al.,  
658 1997; Faccenna et al., 2001; Jolivet & Faccenna, 200; Gattacecca et al., 2007; Lacombe & Jolivet,  
659 2005; Malinverno & Ryan, 1986; Seranne et al., 1999; Rosebaum et al., 2002; Royden, 1993).

660 We confirm earlier studies (Maggi et al., 2012) providing evidence that the early-middle  
661 Eocene (ca. 50-40 Ma) orogenic metamorphism in the Corsica basement predated of ca. 10-15 Ma  
662 the late Eocene subduction zone metamorphism in the oceanic-derived units of the Schistes  
663 Lustrés (ca. 37-34 Ma; Martin et al., 2012; Vitale Brovarone and Herwatz, 2013). The latter was  
664 instead nearly synchronous with the timing of blueschist metamorphism recorded in the Liguride  
665 ophiolites (late Eocene-early Oligocene (ca. 35-28 Ma; Ar-Ar phengite dating in Rossetti et al.,  
666 2001a, b) but younger than the Oligocene-early Miocene orogenic metamorphism recorded in the  
667 Adria-derived continental units (ca. 30-20 Ma; Ar-Ar phengite dating in Brunet et al., 2000;  
668 Rossetti et al., 2004) exposed in the hinterland of the Apennine chain. Moreover, when the Corsica  
669 basement was involved in the Alpine orogeny, the Europe-derived continental units where  
670 accreted to the Adria plate, as documented in the Calabrian-Peloritan belt of the southern  
671 Apennines (Fig.1; Schenk, 1980; Dietrich, 1988; Rossetti et al., 2001; Vignaroli et al., 2008; 2012;  
672 Heymes et al., 2010). Finally, similarly to the Corsica case, the transition from orogenic accretion

673 to crustal thinning in the Calabrian–Peloritan belt is late Oligocene-early Miocene (Platt and  
674 Compagnoni, 1990; Thomson, 1994; Rossetti et al., 2004; Heymes et al., 2010).

675 Since the orogenic structuration of the Europe-derived basement (foreland of the Alpine  
676 orogen) of Corsica pre-dated the subduction zone metamorphism of the oceanic-derived domain  
677 (hinterland), the south-dipping “Alpine” subduction setting is not a feasible solution to frame the  
678 Alpine orogenic construction in Corsica (see also Vitale Brovarone and Herwatz, 2013). The  
679 Cenozoic Apennine-Maghrebian subduction system formed along the convergent margin that  
680 accommodated the subduction of the Ligurian branch of the Tethyan realm below the European  
681 plate therefore appears as the more appropriate setting. The orogenic structure of Corsica is  
682 therefore interpreted as produced in the retrowedge of the E-verging Apennine orogenic wedge,  
683 as produced by the retroward-directed accretion against the backstop of the European plate. In  
684 this scenario, the transition from pure-shear to simple-shear dominated style of deformation in  
685 the Corsica basement - as determined in this paper - is interpreted as the response of continuous  
686 shortening in the backstop region of the orogenic wedge, where the upper-plate material is first  
687 shortened at depth (buttressing effect), progressively exhumed in the wedge axial zone, and then  
688 accreted against the rigid backstop (Fig. 12). The Mesozoic cover rocks were detached from their  
689 basement during progress of the Alpine shortening and metamorphosed at depth, similarly to  
690 what has been reconstructed for the Oman obduction margin (e.g., Agard et al., 2010). Likewise,  
691 the continent-derived units of the Tenda Massif, forming the basal thrust of the obducted Schistes  
692 Lustrés Complex (Molli et al., 2006; Rossetti et al., 2015), were part of a crustal sliver separated  
693 from the western Corsica basement, confirming previous paleotectonic reconstructions proposing  
694 that the Alpine convergent margin overprinted a stretched continental margin (Vitale Brovarone  
695 et al. 2013).

696

#### 697 **8.4 Questioning Hercynian Corsica**

698 The traditional subdivision of the island into “Alpine” and “Hercynian” Corsica implies (by  
699 definition) the absence of Alpine-age deformation in its western part. These terms and the  
700 underlying assumption have largely dominated geological thinking and are ingrained in the  
701 literature despite early notice of the existence of significant Alpine deformation within the  
702 Hercynian granitoids (e.g. Deprat, 1905). In recent years, a mounting body of structural and  
703 radiometric evidence has shown that the Hercynian basement complex of central Corsica and its  
704 late Paleozoic cover suffered significant Alpine-age ductile shear (Malasoma et al., 2006, 2019;

705 Malasoma and Marroni, 2007; Garfagnoli et al., 2009; Di Vincenzo et al., 2016; Di Rosa et al., 2017,  
706 2019; 2020b; Frassi et al., 2022; this study). Notably, the entire Hercynian basement of Corsica was  
707 affected by the thermal (tectono-metamorphic) effects of Alpine-age shortening and/or burial  
708 underneath the sediments of the foreland basin (Fig. 1c). Coherent thermochronometric datasets  
709 point to the former existence of a widespread tectono-sedimentary cover (up to 7–8 km thick) now  
710 lost to erosion (Cavazza et al., 2001; Zarki-Jakni et al., 2004; Fellin et al., 2006; Danisik et al., 2007).  
711 The structural, radiometric, and thermochronologic evidence outlined above show that the whole  
712 of Corsica was directly affected by the Alpine orogeny. We thus propose the abandonment of the  
713 traditional terms “Alpine” and “Hercynian Corsica” as they are altogether incorrect and  
714 misleading.

715

## 716 **9. Conclusions**

717 The P-T-t-deformation history of the Corsica basement presented in this paper indicates  
718 that Alpine orogenic construction spans from early/middle Eocene to early Oligocene times (ca. 50  
719 to ca. 32 Ma). Crustal shortening in the continental basement predated of ca. 15–10 Ma the  
720 subduction zone metamorphism in the oceanic derived Schistes Lustrés Complex. These new  
721 structural and temporal constraints frame the Alpine orogeny in Corsica within the Cenozoic  
722 Apennine-Maghrebian subduction system, in the retroside of the Apennine orogenic wedge.  
723

## 724 **Acknowledgements**

725 Sara Marrone participated to the field work. We wish to thank Moritz Schmelz for help in  
726 thin section preparation.

727

## 728 **Appendix - A: Analytical protocols and methods**

### 729 **Electron Microprobe Analyses (EMPA)**

730 Mineral phases were analyzed with a Cameca SX100 electron microprobe at the Faculty of  
731 Chemistry, Universität Stuttgart. Operating conditions were 15 kV and 10–15 nA, counting times of  
732 20 s both for peak and background, spot sizes of 1–5 µm. Compositions were determined relative to  
733 synthetic oxides, and minerals, used also for routine calibration and instrument stability monitoring.  
734 Repeated analyses of the standards resulted in one-sigma ( $1\sigma$ ) standard deviations close to the ones  
735 calculated from counting statistics. For the major minerals, calculated  $1\sigma$  (%) precisions are (i) better

than 1.5 % for Si; (ii) better than 2% for Al; (iii) 1 to 5% for Ca, Mg, Fe, Mn, Ti, Na and K, applying the above-mentioned conditions. The chemical formulas of white mica (Wm) were calculated on the basis of 11 oxygens and  $\Sigma$  (Si, Al, Ti, Cr, Mn, Mg, Fe) = 6.02 cations, assuming  $Fe^{3+} = [9.96 - 2*(Si + Ti) - (Al + Cr) - 2*(Ca + Ba) - (Na + K)]$ , and a stoichiometric fixed trioctahedral substitution ( $X_{Tri} = 0.02$ ). The molar fractions of paragonite ( $X_{Pg} = \text{atomic } [Na / (Na + K + Ca + Ba)]$ ), pyrophyllite ( $X_{PrI} = [1 - (Na + K + Ca + Ba)]$ ), muscovite ( $X_{Ms} = Al^{[IV]} - \{X_{Pg} + X_{PrI} + (X_{Tri}/2) + Ti + [(Ca + Ba) / (Na + K + Ca + Ba)]\}$ ) and celadonite ( $X_{Cel} = 1 - \{X_{Ms} + X_{Pg} + X_{PrI} + (X_{Tri}/2) + Ti + [(Ca + Ba) / (Na + K + Ca + Ba)]\}$ ) were then calculated. The chemical formulas of chlorite (Chl) were calculated based on 10 cations ( $\Sigma$  [Si, Al, Ti, Cr, Mn, Mg, Fe]) assuming  $Fe^{3+}(\text{apfu}) = [8 - 2*(Si + Ti) - Al^{\text{Tot}}]$ . The chemical formulas of stilpnomelane (Stp) were calculated on the basis of 120 cations ( $\Sigma$  [Si, Al, Ti, Mn, Mg, Fe]), assuming  $(Si + Al^{[IV]}) = 72$  apfu,  $Fe^{3+} = \{[Al^{\text{Tot}} + 2*Fe^{\text{Tot}} + 2*(Mg + Mn) + 2*(Si + Ti) + 2*(Ba + Ca) + K + Na]/3\} - 64$  and OH =  $(Fe^{2+} + Mg + Mn)$ . The chemical formulas of feldspar (Fsp) were calculated based on 8 oxygens assuming  $Fe^{3+} = Fe^{\text{Tot}}$ . The chemical formulas of titanite (Ttn) were calculated based on 5 oxygens, assuming Si= 1 apfu and  $Fe^{3+} = Fe^{\text{Tot}}$ . The chemical formuls of epidote (Ep) were calculated based on 12.5 oxygens and assuming  $Fe^{3+} = Fe^{\text{Tot}}$ . The pistacite component ( $X_{Ps} = \text{atomic } [Fe^{3+} / (Al + Fe_{3+})]$ ) was then calculated. The chemical formulas of biotite (Bt) were calculated based on 11 oxygens assuming  $Fe^{2+} = Fe^{\text{Tot}}$ . The chemical formulas of ilvaite (Ilv) were calculated based on 8.5 oxygens and assuming  $(Al + Fe^{3+}) = 1$  apfu. The chemical formulas of ilmenite (Ilm) were calculated based on 2 cations ( $\Sigma$  [Al, Ti, Mn, Mg, Fe]) assuming  $Fe^{3+}(\text{apfu}) = [2 - (2 * Ti) - Al]$ . The chemical formulas of garnet (Grt) were calculated based on 8 cations with H<sub>2</sub>O wt% determined through the deficiency of Si in the tetrahedral site  $[Si^{4+} + (H^+/4)] = 3$  apfu. Feldspar, biotite, titanite, ilmenite and magnetite structural formulae were calculated using existing routines in Calcmin\_32 software (Brandelink, 2009). White mica, chlorite, stilpnomelane, epidote, garnet and ilvaite structural formulae were calculated through opportune routines compiled during this work and then implemented in the Calcmin\_32 software (Bradelik, 2009). The chemical formulae of amphibole were calculated through the ACES2013 Excel spreadsheet (Locock, 2014), using the 13-CNK normalization scheme and with  $Fe^{3+}$  estimation following the electroneutrality criterion (Hawthorne et al., 2012). Amphibole classification is after Wintsch et al., (1999) and Hawthorne et al. (2012).

764

## 765 Whole-rock geochemistry

Whole-rock major element analyses were performed at the Activation Laboratories (Ontario, Canada), by means of ICP emission following the 4Lithores analytical protocol (lithium

768 metaborate/tetraborate fusion ICP whole rock) For major elements the precision is estimated better  
769 than 2% for values higher than 5 wt %, and better than 5% in the range 0.1-5 wt %. Further details  
770 can be found at <https://actlabs.com/geochemistry/lithogeochemistry-and-whole-rock-analysis/lithogeochemistry/#d2c5f444686baec86>.  
771

772

### 773 **$^{40}\text{Ar}$ - $^{39}\text{Ar}$ geochronology**

774  $^{40}\text{Ar}$ - $^{39}\text{Ar}$  in-situ analyses were completed at IGG-CNR (Pisa, Italy). Following back-scattered  
775 electron (BSE) imaging, rock chips ~9 mm in diameter was drilled from polished thick (~0.4 mm  
776 thick) sections using a diamond core drill. Samples, after cleaning by alternating deionized water  
777 and methanol, were wrapped in aluminum foil and irradiated for 60 hours in the TRIGA reactor at  
778 the University of Pavia (Italy), along with the monitor Fish Canyon Tuff sanidine (FCs). In-situ  $^{40}\text{Ar}$ -  
779  $^{39}\text{Ar}$  analyses were completed through an ultraviolet laser beam, produced by a pulsed Nd:YAG  
780 laser (frequency quadrupled and Q-switched). The ultraviolet laser, operating at 20 Hz and 0.5–1  
781 mJ per pulse, was focused to ~10  $\mu\text{m}$  and repeatedly rastered, by a computer-controlled x-y stage,  
782 over areas of ~0.010–0.015  $\text{mm}^2$  (typical 100x100  $\mu\text{m}^2$ ) and a few ten micrometres deep. Argon  
783 isotope compositions were determined simultaneously through a multi-collector noble gas mass  
784 spectrometer ARGUS VI (Thermo Fisher Scientific). Ar isotopes from 40 to 37 were acquired using  
785 Faraday detectors, equipped with  $10^{12} \Omega$  resistors for  $^{40}\text{Ar}$  and  $^{38}\text{Ar}$  and  $10^{13} \Omega$  resistors for  $^{39}\text{Ar}$   
786 and  $^{37}\text{Ar}$ . Faraday detectors were cross calibrated for the slight offset using air shots.  $^{36}\text{Ar}$  was  
787 measured using a Compact Discrete Dynode (CDD) detector. The CDD was calibrated daily for its  
788 yield by measuring four to six air pipettes prior to the first analysis. Blanks were monitored every  
789 one to two runs and were subtracted from succeeding sample results. Data corrected for post-  
790 irradiation decay, mass discrimination effects, isotope derived from interfering neutron reactions  
791 and blank are listed in Supplementary Material#3. Uncertainties on single runs are  $2\sigma$  analytical  
792 uncertainties, including in-run statistics and uncertainties in the discrimination factor, interference  
793 corrections and procedural blanks. Uncertainties on weighted means also include the uncertainty  
794 on the fluence monitor ( $2\sigma$  internal errors). Ages were calculated using an age of 28.201 Ma for  
795 the FCs (Kuiper et al., 2008), using decay constants of Min et al. (2000) and an atmospheric  
796  $^{40}\text{Ar}/^{36}\text{Ar}$  ratio of  $298.56 \pm 0.31$  (Lee et al., 2006). More details about mass spectrometer  
797 calibration and analysis can be found in Di Vincenzo et al. (2021).

798

### 799 **Figure Captions**

800 Figure 1 – (a) The Western Mediterranean region with the main Alpine orogenic belts (red lines  
801 indicating the orogenic fronts) and distribution of the exhumed orogenic roots (purple areas). The  
802 study area is indicated by a yellow rectangle. (b) Geological sketch map of the Corsica Island  
803 (modified after Cavazza et al., 2018); (c) Maximum temperatures experienced by the Corsica rocks  
804 during the Alpine tectonics as derived from low-T thermochronology and Raman spectroscopy of  
805 carbonaceous materials. The areal distribution of maximum temperatures indicates that virtually  
806 all the island was covered either by the Alpine orogenic wedge or by foreland deposits. Source of  
807 data: Cavazza et al. (2001), Zarki-Jhaki et al. (2004), Fellin et al. (2006), Danisik et al. (2007) Viatle  
808 Brovarone et al. (2013), Jourdan et al. (2018).

809

810 Figure 2 – Geological map of the study area at the junction between Alpine and Hercynian Corsica  
811 (modified and re-adapted after (Vitale Brovarone et al., 2013), with indicated the three geological  
812 transects and representative samples described in this study. The metamorphic lineations and  
813 associated sense of shear are after Jolivet et al. (1990), Molli et al. (2006), Maggi et al. (2014)  
814 Rossetti et al. (2015); Beaudoin et al. (2020), this study.

815

816 Figure 3 – (a) Geological map of the Ponte Castirla area (modified and readapted after Rossi et al.,  
817 1994) showing distribution of the main ductile and brittle structural fabrics along Transect-1.  
818 West-verging, ductile-to-brittle thrust contacts are mapped out and a tectonic doubling of the  
819 basement stratigraphy is evident. The unconformable Eocene sediments are also involved in  
820 thrusting. The geological cross section illustrates the structural architecture of the Corsica  
821 basement across Transect-1. Location of the studied samples are also shown. Moving westward,  
822 transition from  $S_1-L_1$  plano-linear fabric to  $D_2$  mylonites ( $S_2$  foliation) is observed in the basement  
823 units. (b) Equal-area (lower-hemisphere projection) stereoplots showing the ductile ( $D_1, D_2$ ) and  
824 brittle fabrics reconstructed along Transect -1. (c) Subvertical principal  $S_1$  foliation and incipient E-  
825 dipping  $S_2$  foliation in the Permian volcaniclastics (sample CO24). (d)  $D_2$  S-C tectonites developed  
826 in Permian volcaniclastics (sample CO25). Sense of shear is top-to-the-W. The inset shows  $D_2$   
827 crenulation folding in shear lithons. (e) Protomylonite fabric in Hercynian granitoids (sample Co-  
828 38).

829

830 Figure 4 – (a) Geological cross section illustrative of the structural architecture across Transect-2  
831 and sample location. (b) Characters of the  $D_2$  deformation in the Hercynian granitoids. Transition

832 from D<sub>2</sub> crenulation (lower portion) to ductile shearing (upper portion) is evident. (c) Sigma-type  
833 feldspar porphyroclasts indicating top-to-the-W shearing. (d) Equal-area (lower-hemisphere  
834 projection) stereoplot of the D<sub>2</sub> plato-linear fabric.

835

836 Figure 5 - (a) Geological cross section illustrative of the structural architecture across Transect-3  
837 and sample location. (b) Equal-area (lower-hemisphere projection) stereoplot of the D<sub>1</sub> (left) and  
838 D<sub>2</sub> (right) structures. (c) Gneissic texture (S-L tectonites) in the Hercynian granitoids (exposure  
839 parallel to L<sub>1</sub> and normal to S<sub>1</sub>. Porphyroclastic feldspar (Fsp) – quartz (Qz) systems define the main  
840 S<sub>1</sub> foliation. Kinematic criteria are not univocal, indicating overall pure-shear (coaxial) deformation.  
841 (d) L<sub>1</sub> stretching lineations in granitoids made of Qz- Wm aggregates trending at high angle (pitch  
842 104°) to the S<sub>1</sub> strike. (e) Subvertical S<sub>1</sub> foliation in the Permian volcaniclastics. Note the sub-  
843 horizontal Qz veins and intrafoliar F<sub>1</sub> folds. (f) Detail showing isoclinal F<sub>1</sub> folds in the Permian  
844 volcaniclastics. Note the deformed, early segregated quartz veins. (g) D<sub>1</sub> boundinage and  
845 stretching in Permian volcaniclastics. (h) S<sub>2</sub> foliation, axial planar to W-verging folds, overprinting  
846 a continuous S<sub>1</sub> foliation and early segregated quartz veins in the Permian volcaniclastics.

847

848 Figure 6 - Sample Microtextures. (a) Thin section scan of sample CO24, showing the S<sub>1</sub> foliation as  
849 defined by aligned white mica embedding quartz and fractured feldspar porphyroclasts. Kinematic  
850 criteria as provided by sigma-type clasts are not univocal, indicating overall pure shear (coaxial)  
851 deformation. (b) The sample CO24 at microscale (crossed polars). The S<sub>1</sub> foliation is defined by  
852 aligned white mica layers and finely-recrystallised quartz enveloping fractured feldspar grains.  
853 Post-tectonic calcite (Cc) growth is observed. (c) Oblique foliation and S-C fabric defined by aligned  
854 white mica folia and recrystallized quartz in sample CO25 (crossed polars). Note syn-tectonic  
855 stilpnomelane growth along the C surfaces. (d) Microtexture of sample CO38 (crossed polars),  
856 showing fractured feldspar grains with recrystallized quartz veins. Domains of shear strain  
857 localization formed by fine-grained recrystallized quartz and white mica enveloped the large  
858 feldspar porphyroclasts. In the high strain domains, quartz shows evidence of undulose extinction,  
859 deformation bands and evidence of dynamic recrystallisation, dominantly assisted by grain  
860 boundary bulging (BLG). (e) Microtexture of sample CO36 (crossed polars), showing feldspar  
861 porphyroclasts with recrystallized quartz veins. Relict igneous quartz show evidence of subgrain  
862 formation (SG) and evidence of dynamic recrystallisation dominantly assisted by subgrain rotation.  
863 The shear bands are defined by fine-grained recrystallized quartz and white mica. The sense of

864 shear, as defined by S-C structures, oblique foliation, and sigma-type porphyroclasts, is top-to-the-  
865 W. (f) Thin section scan of sample CO42, showing the  $S_1$  foliation as defined by white mica folia  
866 and quartz ribbons enveloping porphyroclastic feldspar grains. Stilpnomelane is aligned along the  
867  $S_1$ . (g) Microtexture of sample CO42 (crossed polars) showing fractured igneous quartz and  
868 feldspar grains, embedded in a matrix made of white mica and finely recrystallized quartz that  
869 define the  $S_1$  foliation. The relict quartz show evidence of undulose extinction, subgrain formation  
870 and dynamic recrystallisation. The white mica is crenulated.

871

872 Figure 7 - Sample microtextures. (a) Back-scattered electron (BSE) image of sample CO24, showing  
873 elongated quartz and fractured (igneous) feldspar. White mica defines the main  $S_1$  foliation and  
874 together with quartz fill the cracks in feldspar. (b) BSE image of sample CO25, showing a  
875 pseudomorphic replacement made of white mica, chlorite, titanite, apatite along the main  $S_1$   
876 foliation. (c) BSE image of sample CO55 showing a quartz-white mica- stilpnomelane veins cutting  
877 across a K-feldspar grain. (d) Coronitic overgrowth of the assemblage made of stilpnomelane-  
878 amphibole (winchite)-epidote-titanite after igneous magnetite in sample CO38 (natural light). (e)  
879 BSE image showing chemical zoning of white mica and epidote in sample CO35. (f) The assemblage  
880 epidote-garnet-amphibole (riebekite) overgrowing igneous allanite and magnetite in sample CO35  
881 (natural light). (g) BSE image showing two generations of white mica in sample CO36. (h) BSE  
882 image showing two generation of epidote in sample CO36. (i) Decussate texture defined by  
883 amphibole (riebekite) and stilpnomelane in sample CO42 (natural light).

884

885 Figure 8 – White mica texture and composition in dated samples. (a) sample CO24. (b) Sample  
886 CO36. (c) Sample CO42. (d) Right: Si vs. Al + Fe<sup>3+</sup> diagram for the analyzed Wm; Left: Celadonite –  
887 Pyrophyllite – Muscovite diagram showing the composition of the analyzed Wm.

888

889 Figure 9 – NCKFMASHTO P-T pseudosections calculated for the dated samples (bulk rock  
890 composition shown in Table 2). The fields are contoured with isopleths of phengite (Si apfu)  
891 compositions. Occurrence of stilpnomelane and absence of pumpellyite at low-T and biotite at  
892 high-T, respectively, constrain the overall thermobaric evolution. Mineral abbreviations are after  
893 Whitney and Evans (2010).

894

895     Figure 10 - Summary of in-situ  $^{40}\text{Ar}$ - $^{39}\text{Ar}$  data on rock chips of samples CO24, CO36 and CO42:  
896     cumulative probability distribution and ranked distribution. Uncertainties are  $2\sigma$ . Ages refer to the  
897     youngest peak for each sample. Data are compared with the cumulative probability distribution of  
898     samples previously investigated by Di Vincenzo et al. (2016).

899

900     Figure 11 – Alpine P-T-t paths of the Corsica basement units as available from the literature  
901     compared with the P-T-t data as reconstructed in this study. The tectonic coupling of the different  
902     tectonic slices is constrained at ca. 0.4 GPa and T lower than 300°C during continuous cooling and  
903     W-directed ductile-to-brittle shearing (thrusting).

904

905     Figure 12. Schematic tectonic reconstruction of the Alpine orogeny in Corsica framed within the  
906     retrowedge of the Apennine orogenic wedge (doubly verging orogen). (a) Shortening of the  
907     continental margin as induced by buttressing against the rigid backstop of the European plate  
908     (upper-plate). In this stage ( $D_1$  deformation, at ca. 50-40 Ma) the basement units were  
909     homogenously horizontally shortened and vertically stretched (yellow strain ellipse). (b)  
910     Continuous shortening resulted in the progressive exhumation of the early underplated HP  
911     oceanic units (Schistes Lustrés) that were progressively overthrust and assembled against the  
912     basement units along the ETSZ. This stage corresponds to the top-to-the-W simple-shear stage  
913     ( $D_2$  deformation, at ca. 33-32 Ma) in the early deformed basement units (Not scale; location of  
914     structures is only indicative).

915

916     **Supplementary Material#1:** Fsp and Qz microfabrics in the studied samples.

917

918     **Supplementary Material#2:** EMPA and representative chemical formulas of syn-metamorphic  
919     mineral phases

920

921     **Supplementary Material#3:** T- Fe<sub>2</sub>O<sub>3</sub> pseudosections for samples CO36 and CO42 (calculated at  
922     0.6 GPa)

923

924     **Supplementary Material#4:** Ar-Ar in-situ-data

925

926

927 **References**

- 928 Agard, P., Searle, M.P., Alsop, I., & Dubacq, B. (2010). Crustal stacking and expulsion tectonics during  
 929 continental subduction: P-T deformation constraints from Oman. *Tectonics*, 29 TC5018 1-19,  
 930 doi:10.1029/2010TC002669.
- 931 Agard, P., Plunder, A., Angiboust, S., Bonnet, G., & Ruh, J. (2018). The subduction plate interface:  
 932 rock record and mechanical coupling (from long to short timescales). *Lithos*, 320–321, 537–566.  
 933 <https://doi.org/10.1016/j.lithos.2018.09.029>
- 934 Allmendinger, R.W., & Gubbels, T. (1996). Pure and simple shear plateau uplift, Altiplano-Puna,  
 935 Argentina and Bolivia. *Tectonophysics*, 259, 1-13.
- 936 Augier, R., Agard, P., Monié, P., Jolivet, L., Robin, C. & Booth-Rea, G. (2005). Exhumation, doming  
 937 and slab retreat in the Betic Cordillera (SE Spain): in situ  $^{40}\text{Ar}/^{39}\text{Ar}$  ages and P-T-d-t paths for  
 938 the Nevado-Filabride complex. *Journal of Metamorphic Geology*, 23, 357–381, doi:  
 939 10.1111/j.1525-1314.2005.00581.x
- 940 Austrheim, H. (1987). Eclogitization of lower crustal granulites by fluid migration through shear  
 941 zones. *Earth and Planetary Science Letters*, 81(2-3), 221-232.
- 942 Babeyko, A. Y. & Sobolev, S. V. (2005). Quantifying different modes of the late Cenozoic shortening  
 943 in the central Andes. *Geology*, 33, 621-624.
- 944 Barton, M. & Bergen, M.J. (1984). Secondary ilvaite in a dolerite dyke from Rogaland, SW Norway.  
 945 *Mineralogical Magazine*, 48, 449–456.
- 946 Beaudoin, A., Scaillet, S., Mora, N., Jolivet, L., & Augier, R. (2020). In situ and step-heating  $^{40}\text{Ar}/^{39}\text{Ar}$   
 947 dating of white mica in low-temperature shear zones (Tenda massif, Alpine Corsica, France).  
 948 *Tectonics*, 39, e2020TC006246. <https://doi.org/10.1029/2020TC006246>
- 949 Bestani, L., Espurt, N., Lamarche, J., Bellier, O., & Hollender, F., (2016). Reconstruction of the  
 950 Provence Chain evolution, southeastern France, *Tectonics*, 35, 1506–1525,  
 951 doi:10.1002/2016TC004115
- 952 Bezert, P., & Caby, R. (1988). Sur l'âge post-Bartonien des événements tectonometamorphiques  
 953 alpins en bordure orientale de la Corse cristalline (Nord de Corte). *Bulletin de la Société  
 954 Géologique de France*, 8, 965–971.
- 955 Brandelik, A. (2009). CALCMIN—an EXCEL™ Visual Basic application for calculating mineral structural  
 956 formulae from electron microprobe analyses. *Computer and Geosciences*, 35, 1540-1551.
- 957 Bruguier, O., Bosch, D., Caby, R., Vitale-Brovarone, A., Fernandez, L., Hammor, D., et al. (2017). Age  
 958 of UHP metamorphism in the Western Mediterranean: Insight from rutile and minute zircon  
 959 inclusions in a diamond-bearing garnet megacryst (Edough Massif, NE Algeria). *Earth and  
 960 Planetary Science Letters*, 474, 215–225. <https://doi.org/10.1016/j.epsl.2017.06.043>
- 961 Brunet, C., Monié, P., Jolivet, L., Cadet, J.P. (2000). Migration of compression and extension in the  
 962 Tyrrhenian Sea, insights from  $^{40}\text{Ar}/^{39}\text{Ar}$  ages on micas along a transect from Corsica to Tuscany.  
 963 *Tectonophysics*, 321, 127–155, doi:10.1016/S0040-1951(00)00067-6
- 964 Carminati, E., Lustrino M., & Doglioni, C. (2012). Geodynamic evolution of the central and eastern  
 965 Mediterranean: Tectonics vs. igneous petrology constraints. *Tectonophysics*, 579, 173–192.
- 966 Cavazza, W., Zattin, M., Ventura, B., Zuffa, G.G., 2001. Apatite fission-track analysis of Neogene  
 967 exhumation in northern Corsica (France). *Terra Nova* 13, 51–57.
- 968 Cavazza W., Gandolfi G., & Paganelli L. (2018). Reconstructing the Alpine orogenic wedge and its  
 969 foreland basin: The petrologic transition from Cretaceous passive-margin to Eocene foreland  
 970 sedimentation in northern Corsica (France). In: R.V. Ingersoll, T.F. Lawton and S.A. Graham (Eds.),  
 971 *Tectonics, sedimentary basins, and provenance: A celebration of the career of William R.*  
 972 *Dickinson. Geol. Soc. Am. Spec. Pap.*, 540. [https://doi.org/10.1130/2018.2540\(31\)](https://doi.org/10.1130/2018.2540(31))

- 973 Connolly, J.A.D., 2005. Computation of phase equilibria by linear programming: A tool for  
 974 geodynamic modeling and its application to subduction zone decarbonation. *Earth Planetary*  
 975 *Science Letters* 236, 524–541
- 976 Delgado Martín, J., & Soleri Gil, A. (2010). Ilvaite stability in skarns from the northern contact of the  
 977 Maladeta batholith, Central Pyrenees (Spain). *European Journal of Mineralogy*, 22 (3), 363-380,  
 978 doi: 10.1127/0935-1221/2010/0022-2021
- 979 Danisik, M., Kuhlemann, J., Dunk, I., Szekely, B., & Frisch, W. (2007). Burial and exhumation of  
 980 Corsica (France) in the light of fission track data. *Tectonics*, 26, TC1001.  
 981 <http://dx.doi.org/10.1029/2005TC001938>.
- 982 Deprat, M. (1905). L'origine de la protogine de Corse. *Comptes Rendue Ac. Sc.*, 141 (2), 151-153.
- 983 Dietrich, D. (1988). Sense of overthrust shear in the Alpine nappes of Calabria (southern Italy).  
 984 *Journal of Structural Geology*, 10(4), 373–381. [https://doi.org/10.1016/0191-8141\(88\)90015-6](https://doi.org/10.1016/0191-8141(88)90015-6)
- 985 Di Rosa, M., Frassi, C., Malasoma, A., Marroni, M., Meneghini, F., & Pandolfi, L. (2020a). Syn-  
 986 exhumation coupling of oceanic and continental units along the western edge of the Alpine  
 987 Corsica: A review. *Ophioliti*, 2020, 45 (2), 71-102 - doi: 10.4454/ophioliti.v45i2.533
- 988 Di Rosa M., Meneghini F., Marroni M., Frassi C., & Pandolfi L. (2020b). The coupling of high-pressure  
 989 oceanic and continental units in Alpine Corsica: evidence for syn-exhumation tectonic erosion at  
 990 the roof of the plate interface. *Lithos*, 354-355, 105328,  
 991 <https://doi.org/10.1016/j.lithos.2019.105328>.
- 992 Di Rosa, M., De Giorgi, A., Marroni, M., and Vidal, O. (2017). Syn- convergence exhumation of  
 993 continental crust: Evidence from structural and metamorphic analysis of the Monte Cécu area,  
 994 Alpine Corsica (Northern Corsica, France). *Geological Journal*, 52, 919–937, doi:  
 995 10.1002/gj.2857Di
- 996 Di Vincenzo G., Folco L., Suttle M.D., Brase L. & Harvey R. P. (2021). Multi-collector  $^{40}\text{Ar}/^{39}\text{Ar}$  dating  
 997 of microtektites from Transantarctic Mountains (Antarctica): a definitive link with the  
 998 Australasian tektite/microtektite strewn field. *Geochimica Cosmochimica Acta*, doi:  
 999 doi.org/10.1016/j.gca.2021.01.046
- 1000 Di Vincenzo, G., Carosi, R. & Palmeri, R. (2004). The relationship between tectono-metamorphic  
 1001 evolution and argon isotope records in white mica: constraints from in-situ  $^{40}\text{Ar}-^{39}\text{Ar}$  laser  
 1002 analysis of the Variscan basement of Sardinia. *Journal of Petrology*, 45, 1013–1043, doi: 10.1093/  
 1003 petrology/egh002
- 1004 Di Vincenzo G., Grande A., Prosser G., Cavazza W., & DeCelles, P.G. (2016).  $^{40}\text{Ar}/^{39}\text{Ar}$  laser dating of  
 1005 ductile shear zones from central Corsica (France): Evidence of Alpine (middle to late Eocene) syn-  
 1006 burial shearing in Variscan granitoids. *Lithos*, 262, 369-383.
- 1007 Doglioni, C., Gueguen, E., Sabat, F., & Fernandez, M. (1997). The Western Mediterranean  
 1008 extensional basins and the Alpine orogen. *Terra Nova*, 9(3), 109–112.  
 1009 <https://doi.org/10.1046/j.1365-3121.1997.d01-18.x>
- 1010 Doglioni, C., Mongelli, F., & Pialli, G. (1998). Boudinage of the Alpine belt in the Apenninic back-arc  
 1011 *Memorie della Società Geologica Italiana*, 52, 457-468
- 1012 Durand-Delga, M., 1984. Principaux traits de la Corse Alpine et corrélations avec les Alpes Ligures.  
 1013 *Memorie della Società Geologica Italiana*, 28, 285–329.
- 1014 Faccenna C, Becker, TW, Luente, FP, Jolivet, L, & Rossetti, F. (2001). History of subduction and back-  
 1015 arc extension in the Central Mediterranean. *Geophysical Journal International*, 145, 809–820,  
 1016 doi: 10.1046/j.0956-540x.2001.01435.x.
- 1017 Faccenna, C., Piromallo, C., Crespo-Blanc, A., Jolivet, L. & Rossetti, F. (2004). Lateral slab deformation  
 1018 and the origin of the western Mediterranean arc. *Tectonics*, 23, TC1012,  
 1019 doi:10.1029/2002TC001488

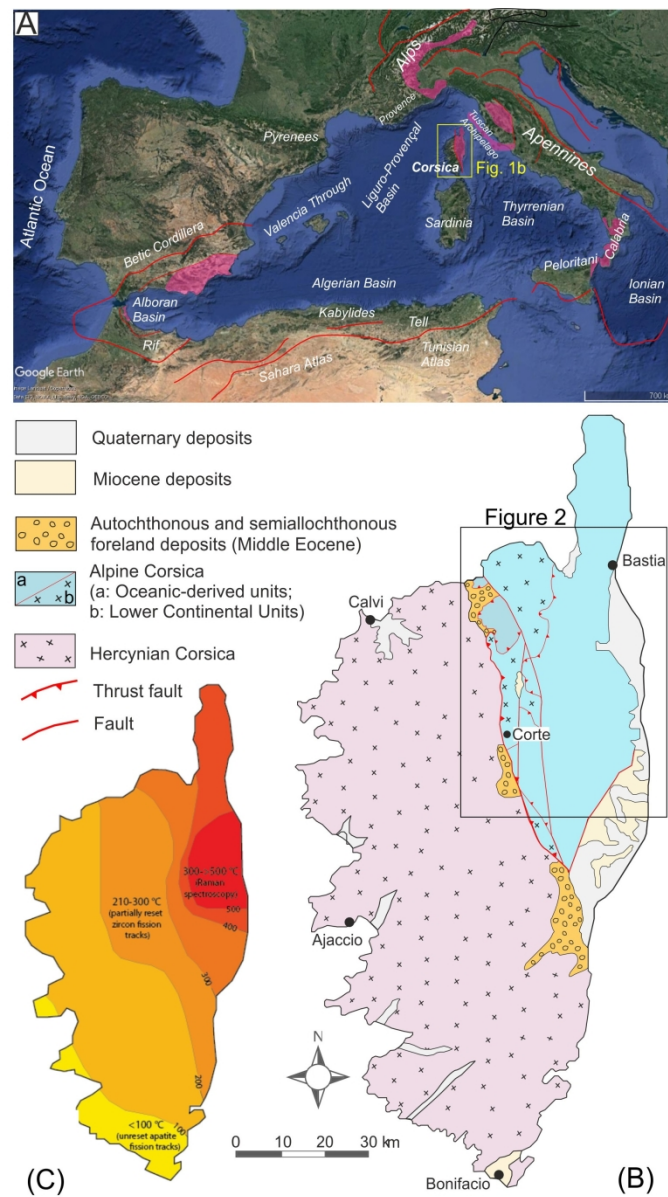
- 1020 Fellin, M.G., Vance, J.A., Garver, J.I., & Zattin, M. (2006). The thermal evolution of Corsica as  
1021 recorded by zircon fission-tracks. *Tectonophysics*, 421, 299–317.
- 1022 Ferrandini, M., Ferrandini, J., Loyer-Pilot, M.D., Butterlin, J., Cravette, J., & Janin, M.C. (1998). Le  
1023 Miocène du Bassin de Saint-Florent (Corse): Modalités de la transgression du Burdigalien  
1024 Supérieur et mise en évidence du Serravalien. *Geobios*, 31, 125–137.
- 1025 Ferrandini, J., Ferrandini, M., Rossi, P., & Savary-Sismondini, B. (2010). Definition and dating of the  
1026 Venaco Formation (Corsica, France): a Priabonian gravity flow deposit. *Comptes Rendus  
1027 Geosciences*, 342, 921–929.
- 1028 Frassi, C., Di Rosa, M., Farina, F., Pandolfi, L., & Marroni, M. (2022). Anatomy of a deformed upper  
1029 crust fragment from western Alpine Corsica (France): insights into continental subduction  
1030 processes. *International Geology Review*. doi: 10.1080/00206814.2022.2031315
- 1031 Fuhrman, M.L., & Lindsley, D.H. (1988). Ternary-feldspar modeling and thermometry. *American  
1032 Mineralogist*, 73, 201–215
- 1033 Fusseis, F., & Handy, M.R. (2008). Micromechanisms of shear zone propagation at the brittle–  
1034 viscous transition. *Journal of Structural Geology*, 30, 1242–1253, doi: 10.1016/j.jsg.2008.06.005.
- 1035 Fusseis, F., Handy, M.R., & Schrank, C. (2006) Networking of shear zones at the brittle-to-viscous  
1036 transition (Cap de Creus, NE Spain). *Journal of Structural Geology*, 28, 1228–1243.
- 1037 Garfagnoli, F., Menna, F., Pandeli, E., & Principi, G. (2009). Alpine metamorphic and tectonic  
1038 evolution of the Inzecca-Ghisoni area (southern Alpine Corsica, France). *Geological Journal*, 44,  
1039 191–210.
- 1040 Gibbons, W., & Horak, J. (1984). Alpine metamorphism of Hercynian horneblende granodiorite  
1041 beneath the blueschist facies Schistes Lustrés nappe of NE Corsica. *Journal of Metamorphic  
1042 Geology*, 2, 95–113.
- 1043 Gonçalves, P., Oliot, E., Marquer, D., & Connolly, J. A. D. (2012). Role of chemical processes on shear  
1044 zone formation: an example from the Grimsel metagranodiorite (Aar massif, Central  
1045 Alps). *Journal of Metamorphic Geology*, 30(7), 703–722.
- 1046 Gueydan, F., Leroy, Y.M., Jolivet, L., & Agard, P. (2003). Analysis of continental midcrustal strain  
1047 localization induced by microfracturing and reaction softening. *Journal of Geophysical Research*  
1048 108, doi:10.1029/2001JB000611.
- 1049 Handy, M.R., Schmid, S., Bousquet, R., Kissling, E., & Bernoulli, D. (2010). Reconciling platetectonic  
1050 reconstructions of Alpine Tethys with geological–geophysical record of spreading and  
1051 subductions in the Alps. *Earth-Science Reviews*. <http://dx.doi.org/10.1016/j.earscirev.2010.06.002>.
- 1053 Hawthorne, F. C., Oberti, R., Harlow, G. E., Maresch, W. V., Martin, R. F., Schumacher, J. C., & Welch,  
1054 M. D. (2012). Nomenclature of the amphibole supergroup. *American Mineralogist*, 97(11–12),  
1055 2031–2048.
- 1056 Heymes, T., Monié, P., Arnaud, N., Pêcher, A., Bouillin, J. P., & Compagnoni, R. (2010). Alpine  
1057 tectonics in the Calabrian-Peloritan belt (southern Italy): New 40Ar/39Ar data in the Aspromonte  
1058 Massif area. *Lithos*, 114(3–4), 451–472. <https://doi.org/10.1016/j.lithos.2009.10.011>.
- 1059 Holyoke, C.W., Tullis, J., 2006. Mechanisms of weak phase interconnection and the effects of phase  
1060 strength contrast on fabric development. *J. Struct. Geol.* 28, doi: 10.1016/j.jsg.2006.01.008.
- 1061 Holland, T.J.B., & Powell, R. (2011) An improved and extended internally consistent thermodynamic  
1062 dataset for phases of petrological interest, involving a new equation of state for solids. *Journal  
1063 of Metamorphic Geology* 29:333–383. doi:10.1111/j.1525-1314.2010.00923.x
- 1064 Holland, T.J.B., Green, E.C.R., Powell, R. (2018). Melting of Peridotites through to Granites: A  
1065 Simple Thermodynamic Model in the System KNCFMASHTOCr, *Journal of Petrology*, 59,  
1066 881–900, <https://doi.org/10.1093/petrology/egy048>

- 1067 Janecke, S.U. & Evans, J.P. (1988). Feldspar-influenced rock rheologies. *Geology*, 16, 1064–  
1068 1067.
- 1069 Johnson, S., Marsh, J., & Vernon, R. (2008). From tonalite to mylonite: coupled mechanical and  
1070 chemical processes in foliation development and strain localization. In: (Ed.) Declan De Paor,  
1071 *Journal of the Virtual Explorer*, 30, doi: 10.3809/jvirtex.2009.00208
- 1072 Jolivet, L., Dubois, R., Fournier, M., Goffé, B., Michard, A., Jourdan, C. (1990). Ductile extension in  
1073 Alpine Corsica. *Geology*, 18, 1007–1010.
- 1074 Jolivet, L., Faccenna, C., Goffé, B., Mattei, M., Rossetti, F., Brunet, C., Storti, F., Funiciello, C., Cadet,  
1075 J.P., D'Agostino, N., & Parra, T. (1998). Mid crustal shear zones in postorogenic extension:  
1076 examples from the northern Tyrrhenian Sea case. *Journal of Geophysical Research* 103, 12123–  
1077 12160.
- 1078 Jolivet, L., & Faccenna, C. (2000). Mediterranean extension and the Africa-Eurasia collision.  
1079 *Tectonics*, 19(6), 1095–1106. <https://doi.org/10.1029/2000TC900018>
- 1080 Jolivet, L., Baudin, T., Calassou, S., Chevrot, S., Ford, M., Issautier, B., Lasseur, E., Masini, E.  
1081 Manatschal, G., Mouthereau, F., Thinon, I., & Vidal O. (2021). Geodynamic evolution of a wide  
1082 plate boundary in the Western Mediterranean, near-field versus far-field interactions. *Bulletin  
1083 de la Société Géologique de France*, 192 doi: <https://doi.org/10.1051/bsgf/2021043>
- 1084 Kuiper K. F., Deino A., Hilgen F. J., Krijgsman W., Renne P. R. & Wijbrans J. R. (2008). Synchronizing  
1085 rock clocks of earth history. *Science*, 320, 500–504.
- 1086 Lacombe, O. & Bellahsen, N. (2016). Thick-Skinned tectonics and basement-involved fold-thrust  
1087 belts: Insight from selected Cenozoic orogens. *Geological Magazine*, 153, 763–810.
- 1088 Lacombe, O., Jolivet, L. (2005). Structural and kinematic relationships between Corsica and the  
1089 Pyrenees-Provence domain at the time of the Pyrenean orogeny. *Tectonics*, 24.
- 1090 Lee J. Y., Marti K., Severinghaus J. P., Kawamura K., Yoo H. S., Lee J. B. & Kim J. S. (2006). A  
1091 redetermination of the isotopic abundances of atmospheric Ar. *Geochimica Cosmochimica Acta*,  
1092 70, 4507–4512.
- 1093 Li, B., & Massonne, H. J. (2018). Two Tertiary metamorphic events recognized in high-pressure  
1094 metapelites of the Nevado-Filabride Complex (Betic Cordillera, S Spain). *Journal of Metamorphic  
1095 Geology*, 36(5), 603–630. <https://doi.org/10.1111/jmg.12312>
- 1096 Locock, A. J. (2014). An Excel spreadsheet to classify chemical analyses of amphiboles following the  
1097 IMA 2012 recommendations. *Computers & Geosciences*, 62, 1–11.
- 1098 Lowry, A. R. & Perez-Gussinyé, M. (2011). The role of crustal quartz in controlling Cordilleran  
1099 deformation. *Nature*, 471, 353–357.
- 1100 Lustrino, M., Morra, V., Fedele, L., & Franciosi, L. (2009). Beginning of the Apennine subduction  
1101 system in central western Mediterranean: Constraints from Cenozoic “orogenic” magmatic  
1102 activity of Sardinia, Italy. *Tectonics*, 28, doi: [10.1029/2008tc002419](https://doi.org/10.1029/2008tc002419).
- 1103 Lustrino M., Fedele L., Agostini S., Di Vincenzo G., Morra V. (2017) Eocene-Miocene igneous activity  
1104 in Provence (SE France): 40Ar/39Ar data, geochemical-petrological constraints and geodynamic  
1105 implications. *Lithos* 288–289, 72–90. <http://dx.doi.org/10.1016/j.lithos.2017.07.008>
- 1106 Maggi, M., Rossetti, F., Corfu, F., Theye, T., Andersen, T.B., Faccenna, C. (2012). Clinopyroxene-rutile  
1107 phyllonites from the East Tenda Shear Zone (Alpine Corsica, France): pressure-temperature-time  
1108 constraints to the Alpine reworking of Variscan Corsica. *Journal of the Geological Society, London*,  
1109 169, 723–732, doi:10.1144/jgs2011-120.
- 1110 Maggi, M., Rossetti, F., Ranalli, G., & Theye, T. (2014). Feedbacks between fluid infiltration and  
1111 rheology along a regional ductile-to-brittle shear zone: the East Tenda Shear Zone (Alpine Corsica).  
1112 *Tectonics*, 33, 253–280.
- 1113 Malasoma, A., Marroni, M., Musumeci, G., & Pandolfi, L. (2006). High pressure mineral assemblage  
1114 in granitic rocks from continental units, Alpine Corsica. France. *Geological Journal* 41, 49–59.

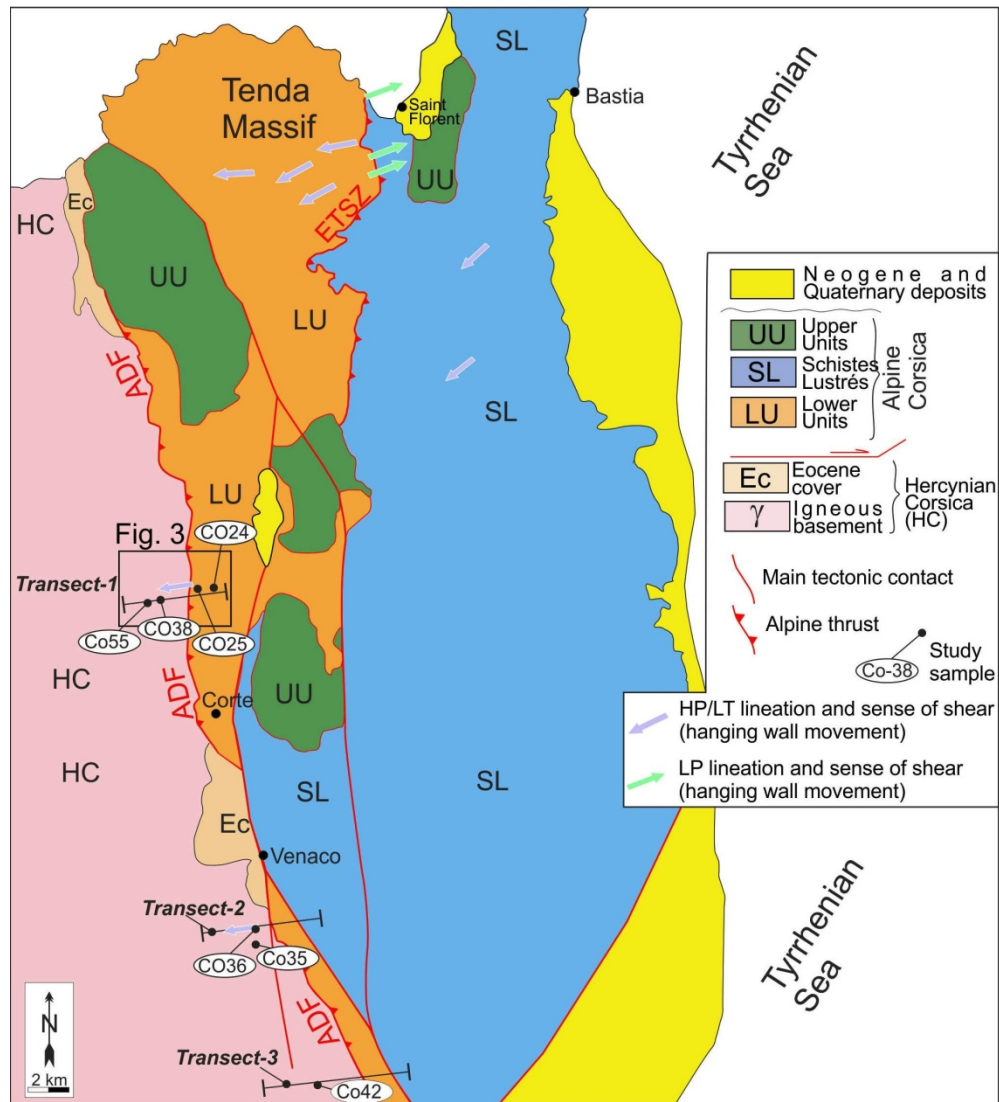
- 1115 Malasoma, A., & Marroni, M. (2007). HP/LT metamorphism in the Volparone Breccia (Northern  
 1116 Corsica, France): evidence for involvement of the Europe/Corsica continental margin in the  
 1117 Alpine subduction zone. *Journal of Metamorphic Geology* 25, 529–545.
- 1118 Malasoma A., Morelli G., Di Rosa M., Marroni M., Pandeli E., Principi, G. & Pandolfi L. (2020). The  
 1119 stratigraphic and structural setting of metamorphic continental units from Alpine Corsica: clues  
 1120 from the area between Asco and Golo valleys (Central Corsica, France). *Journal of Maps*, 16, 313–  
 1121 323.
- 1122 Malusà, M. G., Faccenna, C., Baldwin, S. L., Fitzgerald, P. G., Rossetti, F., Balestrieri, M. L., Danisik,  
 1123 M., Ellero, A., Ottira, G., & Piromallo, C. (2015). Contrasting styles of (U) HP rock exhumation  
 1124 along the Cenozoic Adria-Europe plate boundary (Western Alps, Calabria, Corsica).  
 1125 *Geochemistry, Geophysics, Geosystems*, 16(6), 1786–1824. <https://doi.org/10.1029/2015GC005767>
- 1127 Mancktelow, NS, & Pennacchioni, G. (2005) The control of precursor brittle fracture and fluid-rock  
 1128 interaction on the development of single and paired ductile shear zones *Journal of Structural  
 1129 Geology*, 27, 645–661.
- 1130 Marrone, S., Monié, P., Rossetti, F., Lucci, F., Theye, T., Bouybaouene, M. L., & Zaghloul, M. N. (2021a). The  
 1131 Pressure-Temperature-time-deformation history of the Beni Mzala unit (Upper Sebtides, Rif belt,  
 1132 Morocco): Refining the Alpine tectono-metamorphic evolution of the Alboran Domain of the Western  
 1133 Mediterranean. *Journal of Metamorphic Geology*, 39, 591–615. <https://doi.org/10.1111/jmg.12587>.
- 1134 Marrone, S., Monie, P., Rossetti, F., Aldega, L., Bouybaouene, M., Charpentier, D., et al. (2021b). Timing of  
 1135 Alpine orogeny and postorogenic extension in the Alboran Domain, inner Rif chain, Morocco. *Tectonics*,  
 1136 40, e2021TC006707. <https://doi.org/10.1029/2021TC006707>
- 1137 Marroni, M., Meneghini, F., & Pandolfi, L. (2017). A revised subduction inception model to explain the  
 1138 Late Cretaceous, double-vergent orogen in the precollisional western Tethys: Evidence from the  
 1139 Northern Apennines. *Tectonics*, 36, 2227–2249. <https://doi.org/10.1002/2017TC004627>
- 1140 Martin A.J., Rubatto D., Vitale Brovarone A. and Hermann J., 2011. Late Eocene lawsonite-eclogite  
 1141 facies metasomatism of a granulite sliver associated to ophiolites in Alpine Corsica. *Lithos*, 125,  
 1142 620–640.
- 1143 McAleer, R. J., Bish, D. L., Kunk, M. J., Sicard, K. R., Valley, P. M., Walsh, G. J., et al. (2017). Reaction  
 1144 softening by dissolution-precipitation creep in a retrograde greenschist facies ductile shear zone, New  
 1145 Hampshire, USA. *Journal of Metamorphic Geology*, 35(1), 95–119.
- 1146 Min K., Mundil R., Renne P. R. & Ludwig K. R. (2000) A test for systematic errors in  $^{40}\text{Ar}/^{39}\text{Ar}$   
 1147 geochronology through comparison with U/Pb analysis of a 1.1-Ga rhyolite. *Geochimica  
 1148 Cosmochimica Acta*, 64, 73–98.
- 1149 Molli, G., Malavieille, J. (2010). Orogenic processes and the Corsica/Apennines geodynamic  
 1150 evolution: insights from Taiwan. *International Journal of Earth Sciences*, 100, 1207–1224,  
 1151 doi:10.1007/s00531-010-0598-y.
- 1152 Molli, G., Tribuzio, R., Marquer, D. (2006). Deformation and metamorphism at the eastern border  
 1153 of the Tenda Massif (NE Corsica): a record of subduction and exhumation of continental crust.  
 1154 *Journal of Structural Geology*, 28, 1748–1766, doi:10.1016/j.jsg.2006.06.018.
- 1155 Mouthereau, F., Watts, A.B., & Burov, E. (2013). Structure of orogenic belts controlled by lithosphere  
 1156 age. *Nature Geosciences*, 6, 785–789, doi: 10.1038/ngeo1902.
- 1157 Nemčok, M., Mora, A. and Cosgrove, J. W. (Eds), 2013. Thick-Skin-Dominated Orogens: From Initial  
 1158 Inversion to Full Accretion. Geological Society of London Special Publication, 377, doi  
 1159 10.1144/SP377. Published, 12/2013.
- 1160 O’Hara, K. (1990). State of strain in mylonites from the western Blue Ridge province, southern  
 1161 Appalachians: the role of volume loss. *Journal of Structural Geology* 12, 419–430.
- 1162 O’Hara, K. (2007). Reaction weakening and emplacement of crystalline thrusts: Diffusion control on  
 1163 reaction rate and strain rate. *Journal of Structural Geology*, 29, 1301e1314

- 1164 Papeschi, S., & Musumeci, G. (2019). Fluid-assisted strain localization in quartz at the brittle/ductile  
 1165 transition. *Geochemistry, Geophysics, Geosystems*, 20, doi: 10.1029/2019GC008270
- 1166 Passchier, C. W., & Trouw, R. A. J. (2010). *Microtectonics* (2nd ed.). Springer.
- 1167 Penniston-Dorland, S. C., Kohn, M. J., & Manning, C. E. (2015). The global range of subduction zone  
 1168 thermal structures from exhumed blueschists and eclogites: Rocks are hotter than models. *Earth*  
 1169 and *Planetary Science Letters*, 428, 243–254. <https://doi.org/10.1016/j.epsl.2015.07.031>
- 1170 Pfiffner, O.A. (2006). Thick-Skinned and thin-skinned styles of continental contraction. *Geological*  
 1171 *Society of America Special Paper* 414, 157–177.
- 1172 Platt, J. P. & Compagnoni, R. (1990). Alpine ductile deformation and metamorphism in a Calabrian  
 1173 basement nappe (Aspromonte, south Italy). *Eclogae geologicae Helvetiae* 83(1), 41–58.
- 1174 Principi, G., & Treves, B. (1984). Il sistema Corso-Appennino come prisma di accrezione. Riflessi sul  
 1175 problema generale del limite Alpi-Appennino. *Memorie-Società Geologica Italiana*, 28, 529–576.
- 1176 Rosenbaum, G., Lister, G.S., & Duboz, C. (2002). Relative motions of Africa, Iberia and Europe during  
 1177 Alpine orogeny. *Tectonophysics*, 359, 117–129.
- 1178 Rossetti, F., Faccenna, C., Goffé, B., Monié, P., Argentieri, A., Funiciello, R., & Mattei, M. (2001).  
 1179 Alpine structural and metamorphic signature of the Sila Piccola Massif nappe stack (Calabria,  
 1180 Italy): Insights for the tectonic evolution of the Calabrian Arc. *Tectonics*, 20(1), 112–133, doi:  
 1181 10.1029/2000TC900027
- 1182 Rossetti, F., Faccenna, C., Jolivet, L., Funiciello, R., Goffé, B., Tecce, F., & Vidal, O. (2001). Structural  
 1183 signature and exhumation P-T-t path of the Gorgona blueschist sequence (Tuscan  
 1184 Archipelago, Italy). *Ophioliti*, 26, 175–186.
- 1185 Rossetti, F., Glodny, J., Theye, T., & Maggi, M. (2015). Pressure–temperature–deformation–time of  
 1186 the ductile Alpine shearing in Corsica: From orogenic construction to collapse. *Lithos*, 218, 99–  
 1187 116, doi: 10.1016/j.lithos.2015.01.011
- 1188 Rossetti, F., Goffé, B., Monié, P., Faccenna, C., & Vignaroli, G. (2004). Alpine orogenic P-T-t-  
 1189 deformation history of the Catena Costiera area and surrounding regions (Calabrian Arc,  
 1190 southern Italy): The nappe edifice of north Calabria revised with insights on the Tyrrhenian-  
 1191 Apennine system formation. *Tectonics*, 23(6), doi: [10.1029/2003TC001560](https://doi.org/10.1029/2003TC001560).
- 1192 Rossi, P., Durand-Delga, M., Caron, J.M., Guieu, G., Conchon, O., Libourel, G., & Loÿe-Pilot, M.D.,  
 1193 avec la collaboration de Ohnenstetter D., Ohnenstetter M., Ferrandini J., Rouire J., Dominici R.,  
 1194 (1994). Notice esplicative, Carte géol. France (1/50000), feuille Corte (1110). Orléans: BRGM, 150  
 1195 pp.
- 1196 Schenk, V. (1980). U-Pb and Rb-Sr radiometric dates and their correlation with metamorphic events  
 1197 in the granulite basement of the Serre, southern Calabria (Italy), *Contribution to Mineralogy and*  
 1198 *Petrology*, 73, 23–38.
- 1199 Stip, M, Stunitz, H, Heilbronner, R, & Schmid, SM. (2002). The eastern Tonale fault zone: a “natural  
 1200 laboratory” for crystal plastic deformation for quartz over a temperature range from 250 to  
 1201 700°C. *Journal of Structural Geology*, 24, 1861–1884
- 1202 Thomson, S. N. (1994). Fission track analysis of the crystalline basement rocks of the Calabrian Arc,  
 1203 southern Italy: evidence of Oligo-Miocene late orogenic extension and erosion, *Tectonophysics*,  
 1204 238, 331–352
- 1205 Tribuzio, R., & Giacomini, F. (2002). Blueschist facies metamorphism of peralkaline rhyolites from  
 1206 the Tenda crystalline massif (northern Corsica): evidence for involvement in Alpine subduction  
 1207 event?. *Journal of Metamorphic Geology*, 20, 513–526.
- 1208 Turco, E., Macchiavelli, C., Mazzoli, S., Schettino, A., & Pierantoni, P.P. (2012). Kinematic evolution  
 1209 of Alpine Corsica in the framework of Mediterranean mountain belts. *Tectonophysics*, 579, 193–  
 1210 206.

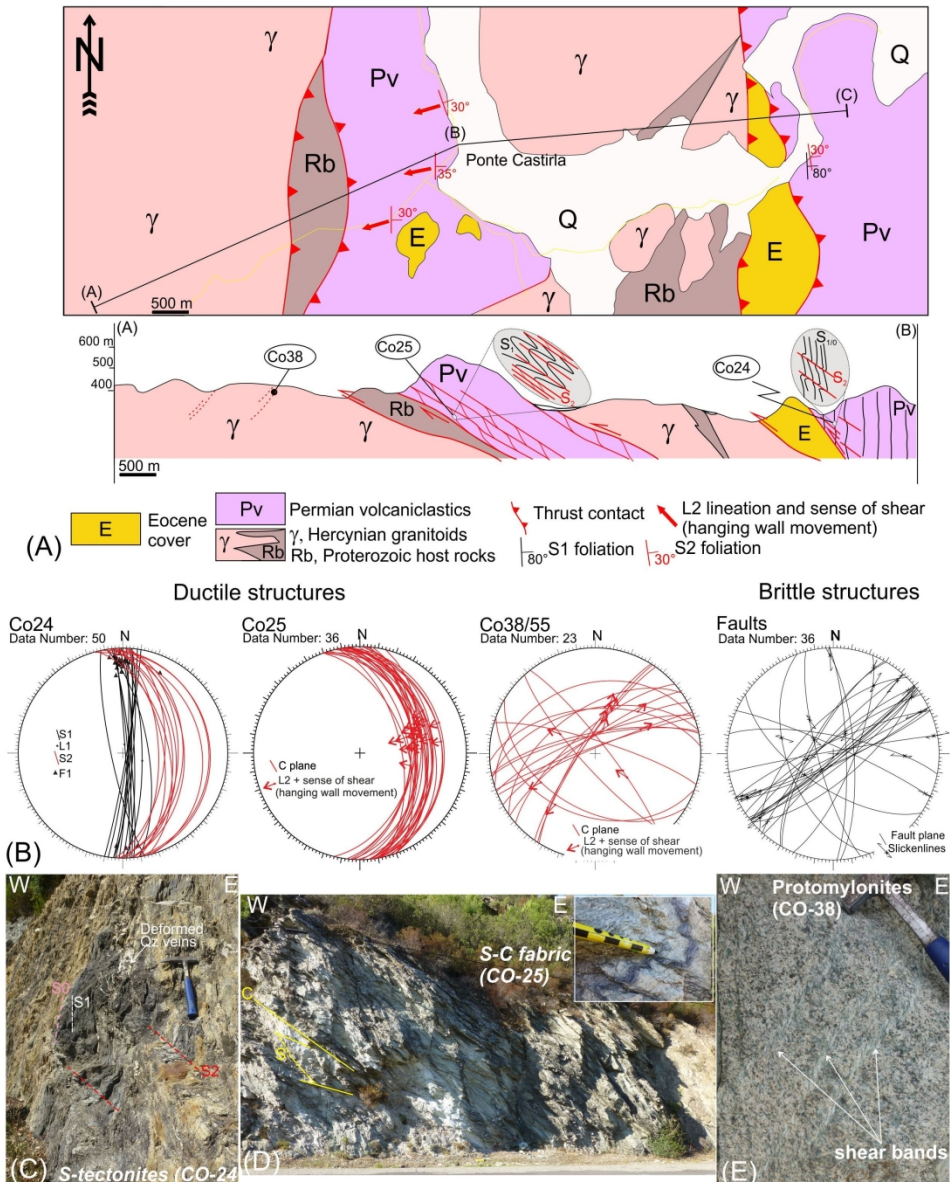
- 1211 van Hinsbergen, D., Vissers, R., & Spakman, W. (2014). Origin and consequences of western  
1212 Mediterranean subduction, rollback, and slab segmentation. *Tectonics*, 33, 393–419.
- 1213 Vignaroli, G., Minelli, L., Rossetti, F., Balestrieri, M. L., & Faccenna, C. (2012). Miocene thrusting in  
1214 the eastern Sila Massif: Implication for the evolution of the Calabria-Peloritani orogenic wedge  
1215 (southern Italy). *Tectonophysics*, 538, 105–119. <https://doi.org/10.1016/j.tecto.2012.03.011>
- 1216 Vignaroli, G., Rossetti, F., Theye, T., & Faccenna, C. (2008). Styles and regimes of orogenic thickening  
1217 in the Peloritani Mountains (Sicily, Italy): New constraints on the tectono-metamorphic evolution  
1218 of the Apennine belt. *Geological Magazine*, 145(4), 552–569.  
1219 <https://doi.org/10.1017/S0016756807004293>
- 1220 Villa, I.M., Bucher, S., Bousquet, R., Kleinhanns, I.C. & Schmid, S.M. (2014). Dating polygenetic  
1221 metamorphic assemblages along a transect across the Western Alps. *Journal of Petrology*, 55,  
1222 doi: 10.1093/petrology/egu007
- 1223 Vitale Brovarone, A., Beyssac, O., Malavieille, J., Molli, G., Beltrando, M., & Compagnoni R. (2013).  
1224 Stacking and metamorphism of continuous segments of subducted lithosphere in a high-pressure  
1225 wedge: The example of Alpine Corsica (France). *Earth Science Review*, 116, 35–56,  
1226 doi:10.1016/j.earscirev.2012.10.003.
- 1227 Vitale Brovarone, A., Herwartz, D. (2013). Timing of HP metamorphism in the Schistes Lustrés of  
1228 Alpine Corsica: New Lu–Hf garnet and lawsonite ages. *Lithos*, 172, 175–191.
- 1229 Whitney, D., & Evans B., (2010). Abbreviations for names of rock-forming minerals. *American  
1230 Mineralogist*, 95, 185–187, doi:10.2138/am.2010.3371.
- 1231 Wintsch, R.P., Christoffersen, R., & Kronenberg, A.K., (1995). Fluid-rock reaction weakening of fault  
1232 zones. *Journal of Geophysical Research*, 100, 13,021e13,032.
- 1233 Wintsch, R.P., Aleinikoff, J.N., & Yi, K. (2005). Foliation development and reaction softening by  
1234 dissolution and precipitation in the transformation of granodiorite to orthogneiss, Glastonbury  
1235 complex, Connecticut, U.S.A. *Canadian Mineralogist*, 43, 327-347.
- 1236 White R.W., Powell R. & Clarke G.L., 2002. The interpretation of reaction textures in Fe-rich  
1237 metapelitic granulites of the Musgrave Block central Australia: constraints from mineral  
1238 equilibria calculations in the system  $K_2O$ - $FeO$ - $MgO$ - $Al_2O_3$ - $SiO_2$ - $H_2O$ - $TiO_2$ - $Fe_2O_3$ . *Journal of  
1239 Metamorphic Geology*, 20, 41–55
- 1240 White, R. W., Powell, R., Holland, T. J. B., Johnson, T. E., & Green, E. C. R. (2014). New mineral  
1241 activity–composition relations for thermodynamic calculations in metapelitic systems. *Journal of  
1242 Metamorphic Geology*, 32(3), 261–286.
- 1243
- 1244
- 1245
- 1246
- 1247
- 1248
- 1249



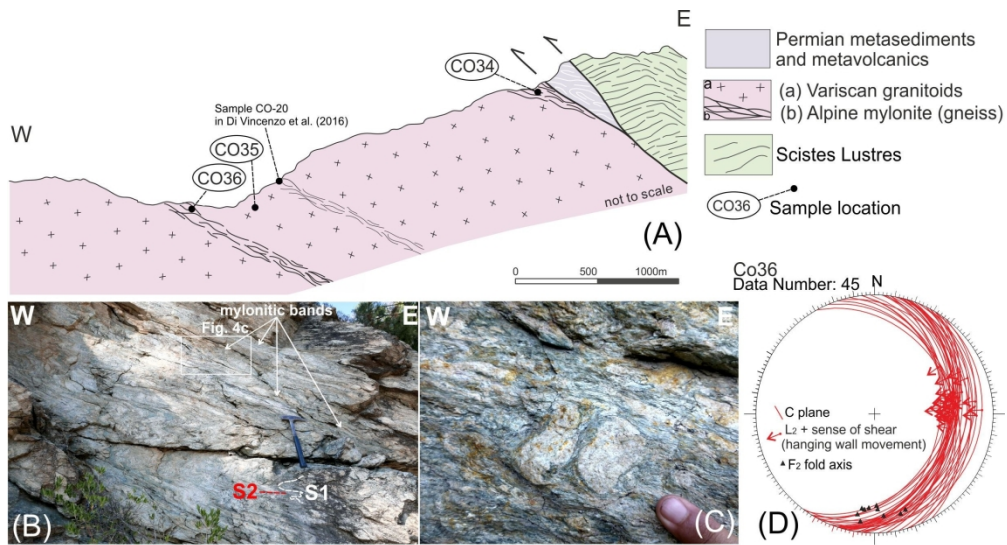
157x281mm (300 x 300 DPI)



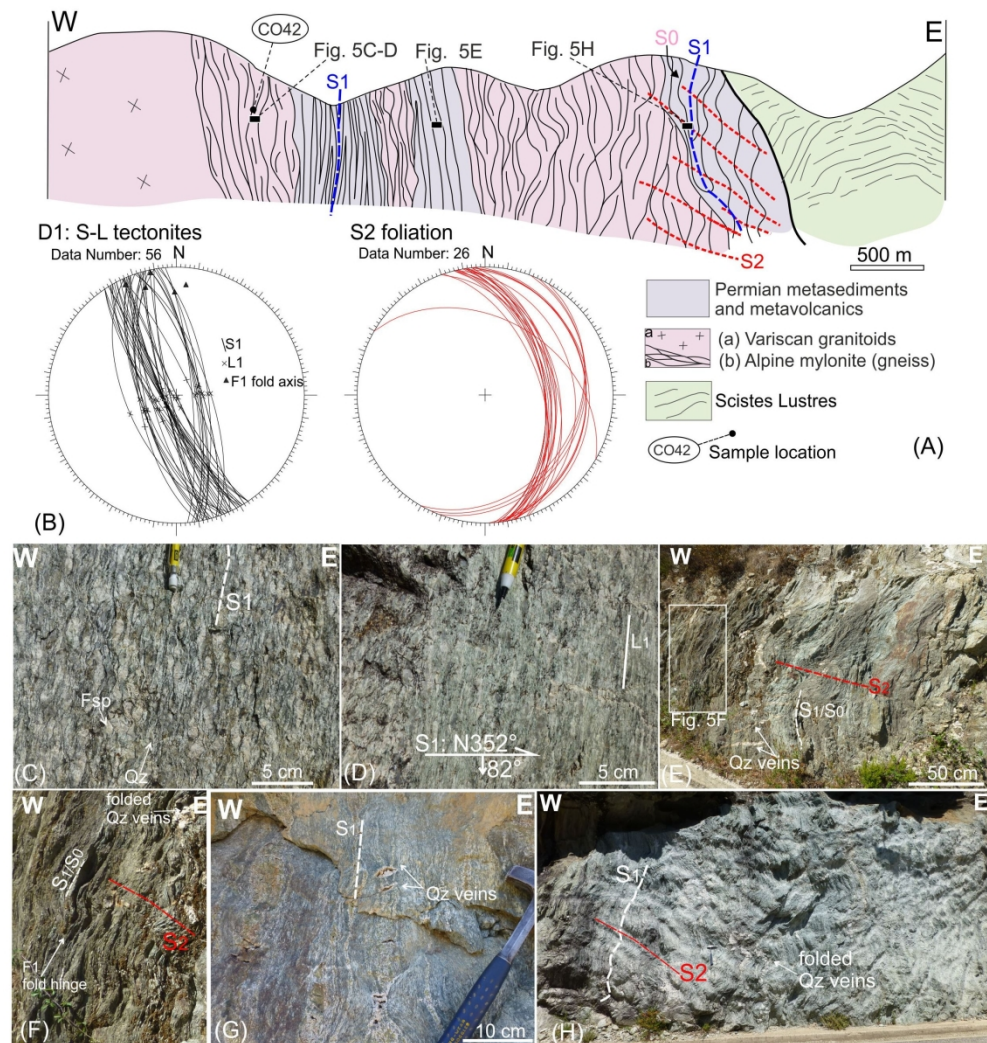
173x193mm (300 x 300 DPI)



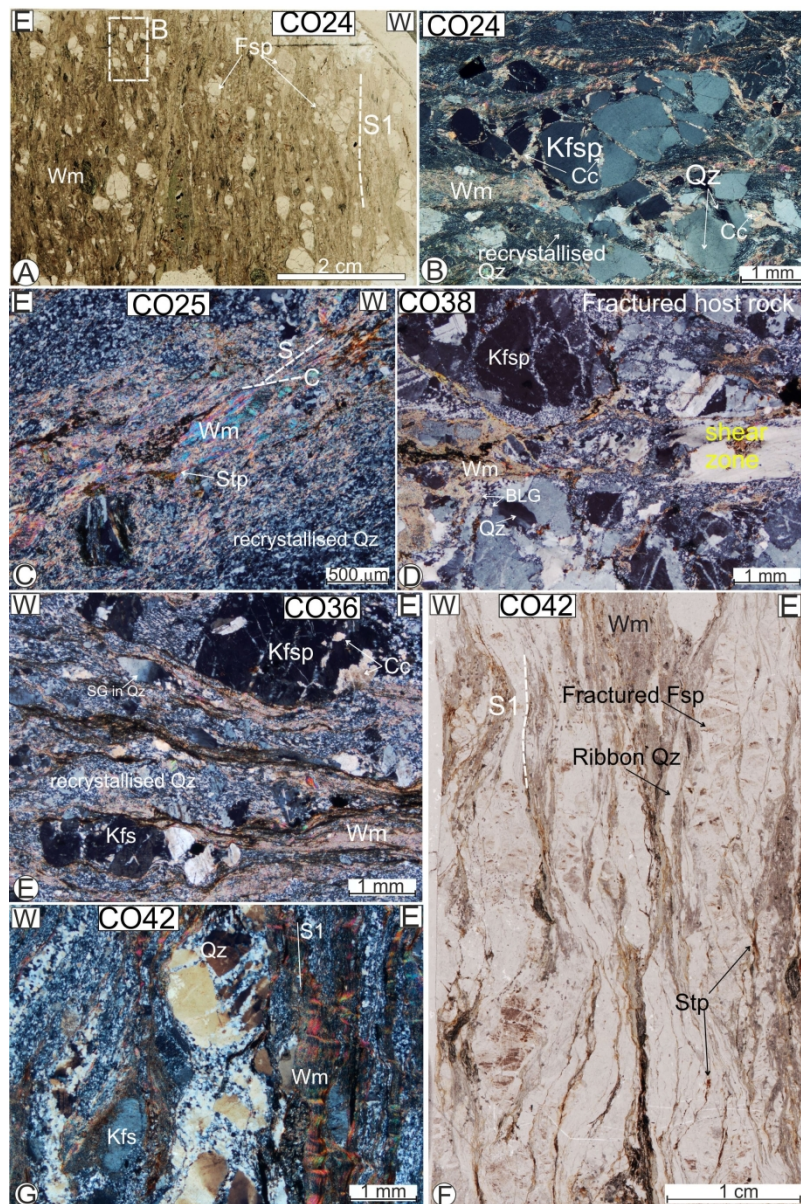
213x265mm (300 x 300 DPI)



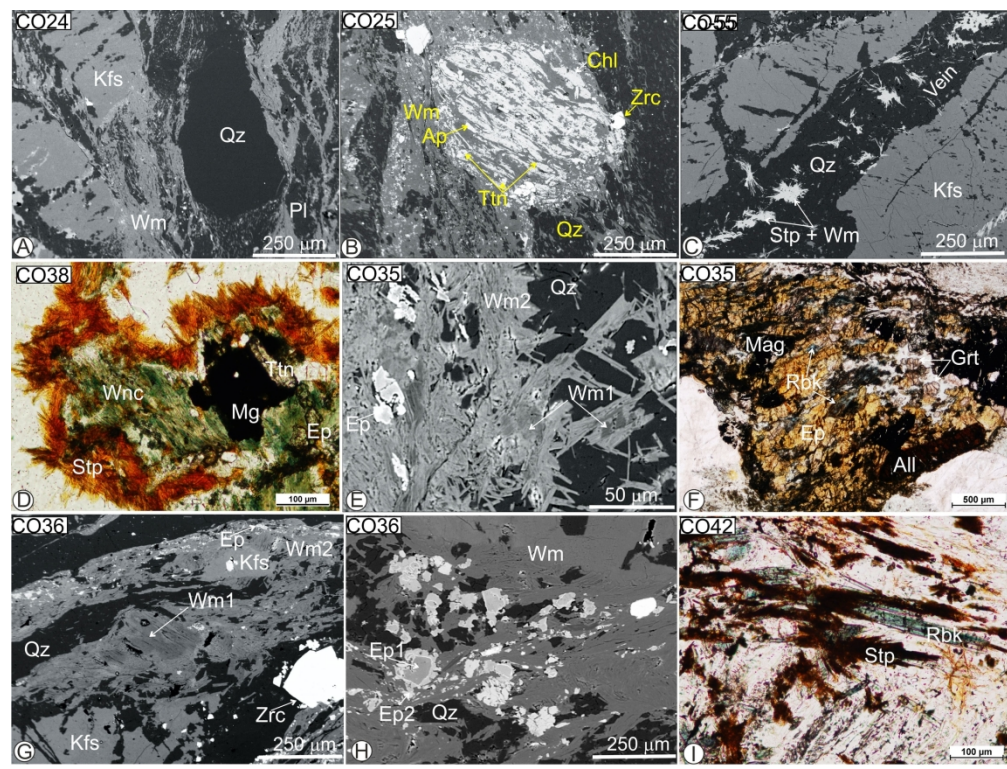
207x111mm (300 x 300 DPI)



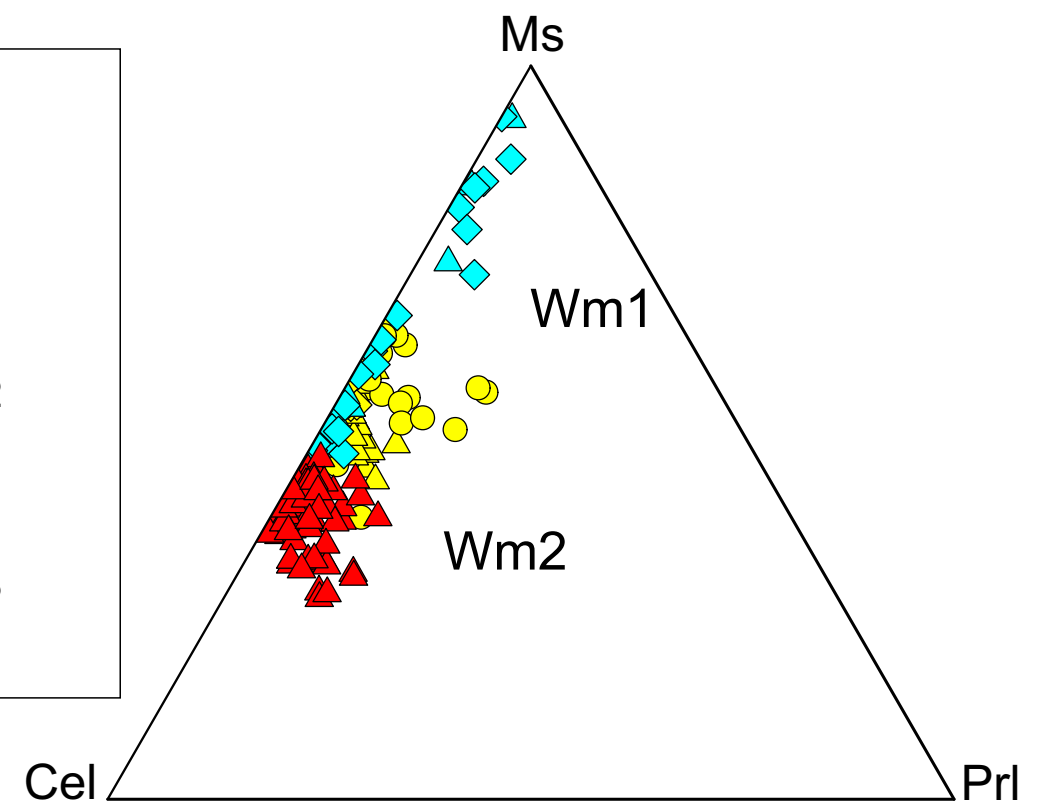
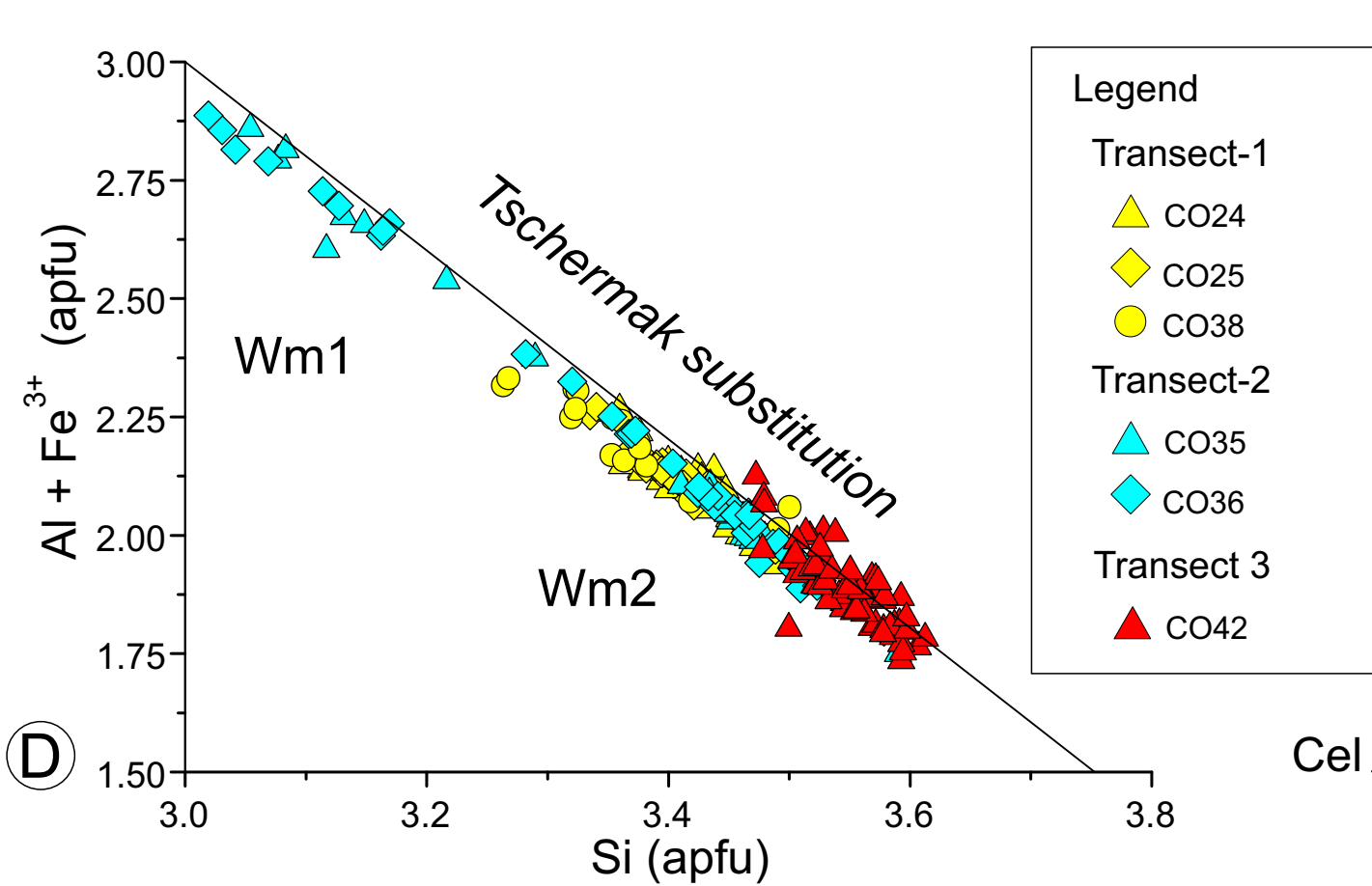
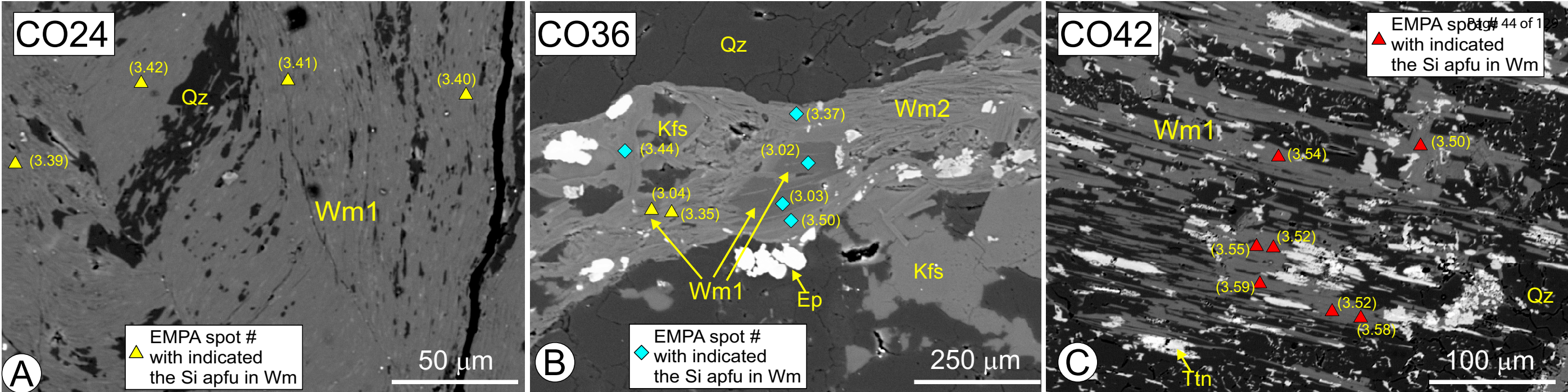
214x223mm (300 x 300 DPI)

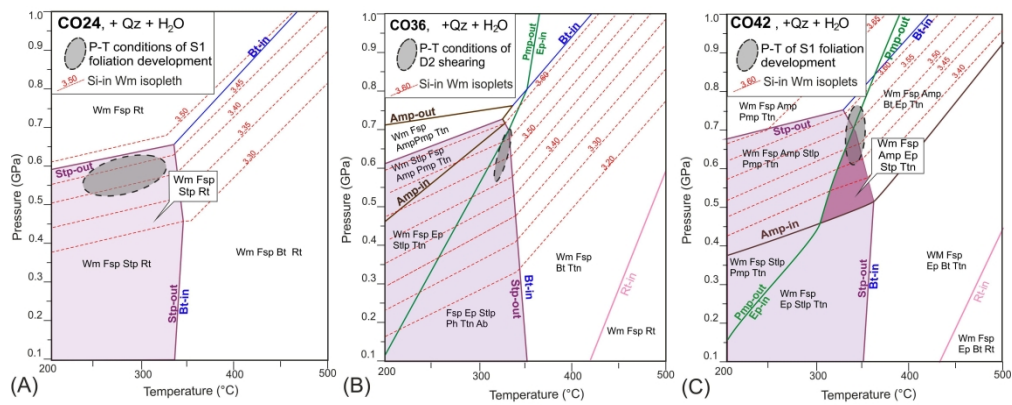


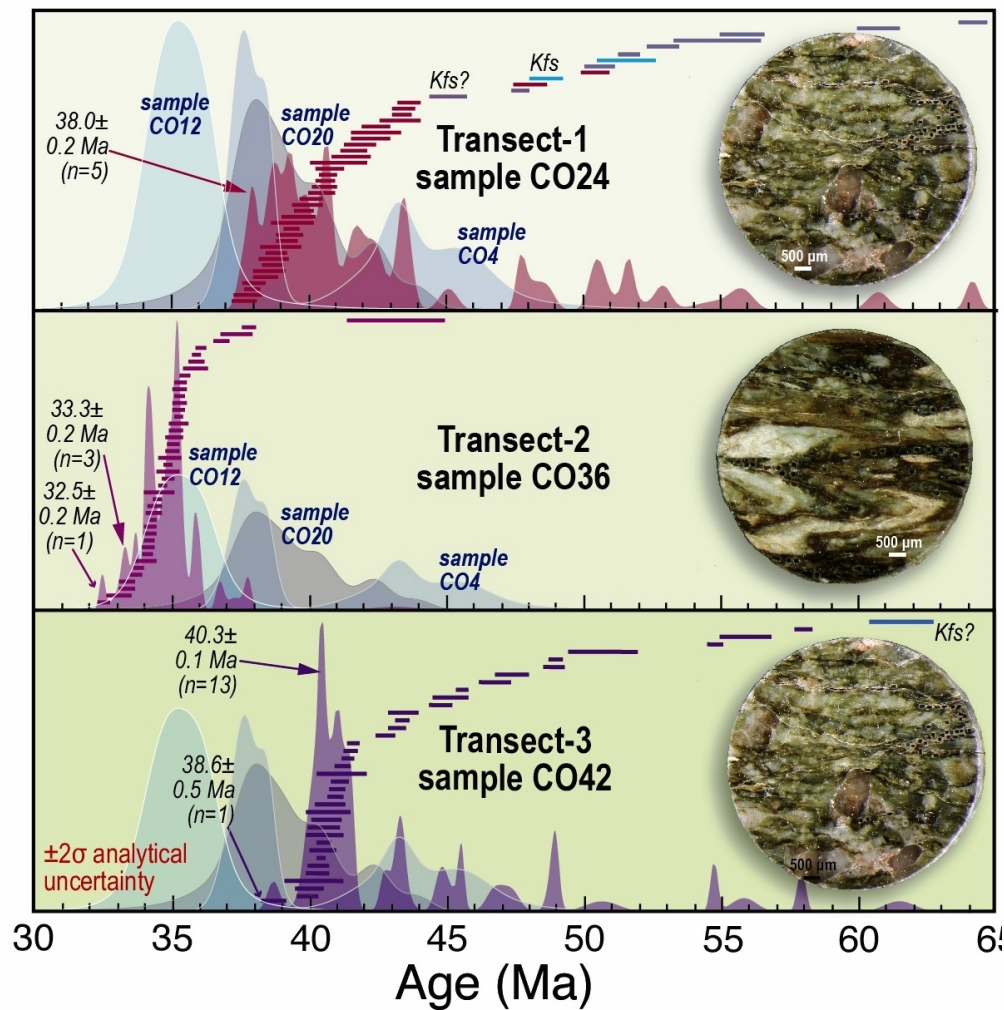
195x290mm (300 x 300 DPI)



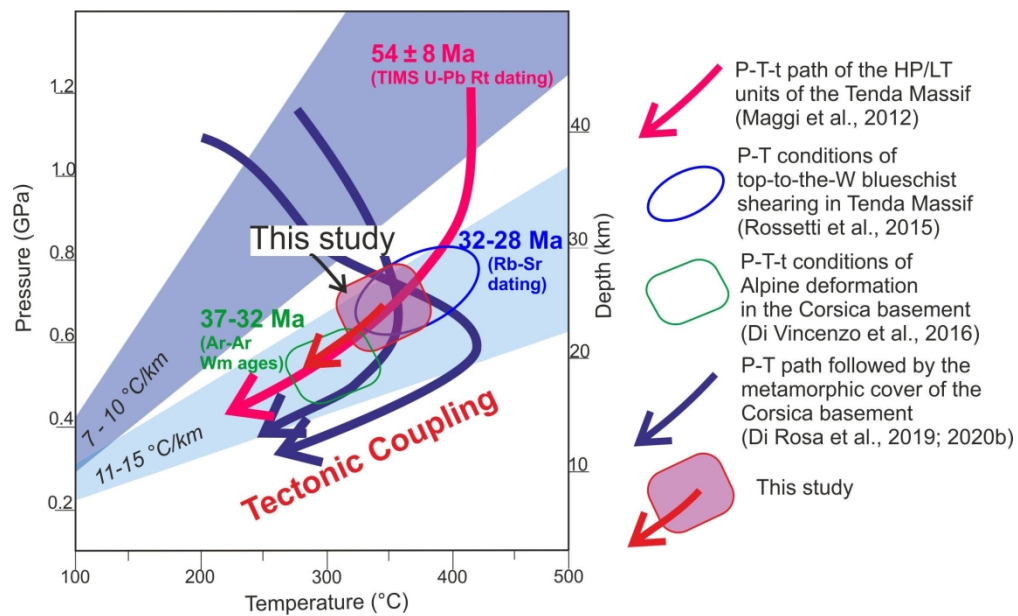
207x157mm (300 x 300 DPI)



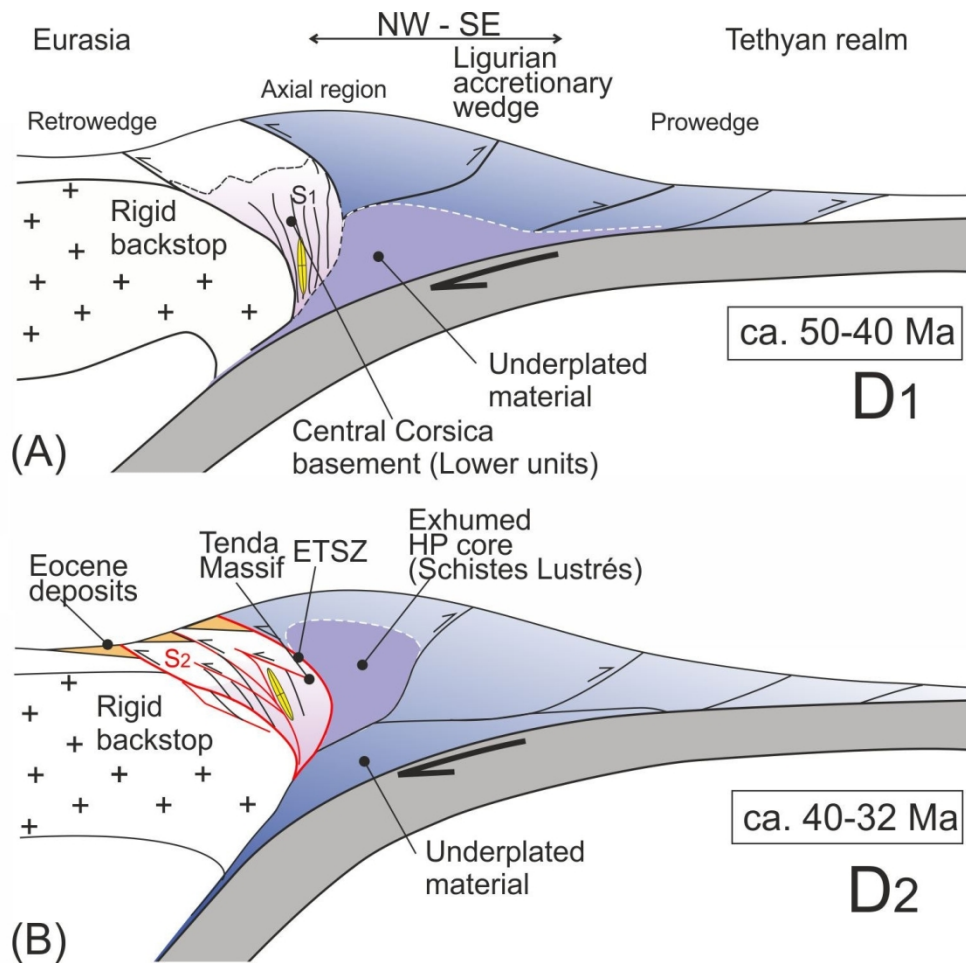




318x322mm (96 x 96 DPI)



198x122mm (300 x 300 DPI)



132x130mm (300 x 300 DPI)

**Table 1 - List of the Studied Samples, with Geographical Location and Analytical Methods**

Sample	Rock Type	Location		Metamorphic Assemblage	Analytical method		
		Latitude (°N)	Longitude (°W)		EMPA	ICP whole rock	<sup>40</sup> Ar/ <sup>39</sup> Ar in situ dating
CO24	Permian volcanics	42°23' 09.8"	09° 10' 01.5"	Qz-Wm-Ab, Stp, Rt + Cb (late)	X	X	X
CO25	Permian volcanics	42° 22' 52.1"	09°07'59.1"	Qz-Wm-Ab, Chl, Stp, Ep, Ttn, Ap + Cb (late)	X		
CO38	Granitoid	42° 22' 20.0"	09° 06' 44.8"	Qz-Wm-Ab, Stp, Ep, Ch, Ttn, Bt, Amp (Wnc), Ap + Ilv + Cb (late)	X		
C055	Granitoid	42° 22' 19.4"	09° 06' 43.4"	Qz-Wm-Ab, Stp, Ep, Chl, Ttn, Bt, Ap + Cb (late)			
CO35	Granitoid	42° 10' 24.8"	09° 09' 45.5"	Qz-Wm-Ab, Stp, Ep, Amp (Rbk), Ttn, Ab + Grt (And-Grs), Ap + Cb (late)	X		
CO36	Granitoid	42° 11' 53.9"	09° 10' 17.0"	Qz-Wm-Ab, Stp, Ep, Ttn, Amp (Act), Cb (late)	X	X	X
CO42	Granitoid	42° 06' 12.8"	09° 15' 37.0"	Wm-Qz- Ab-Stop-Amp (Rbk), Ep, Ttn, Ap, Cb (late)	X	X	X

(\*) Mineral abbreviations after Whitney and Evans (2010); Wm: white mica

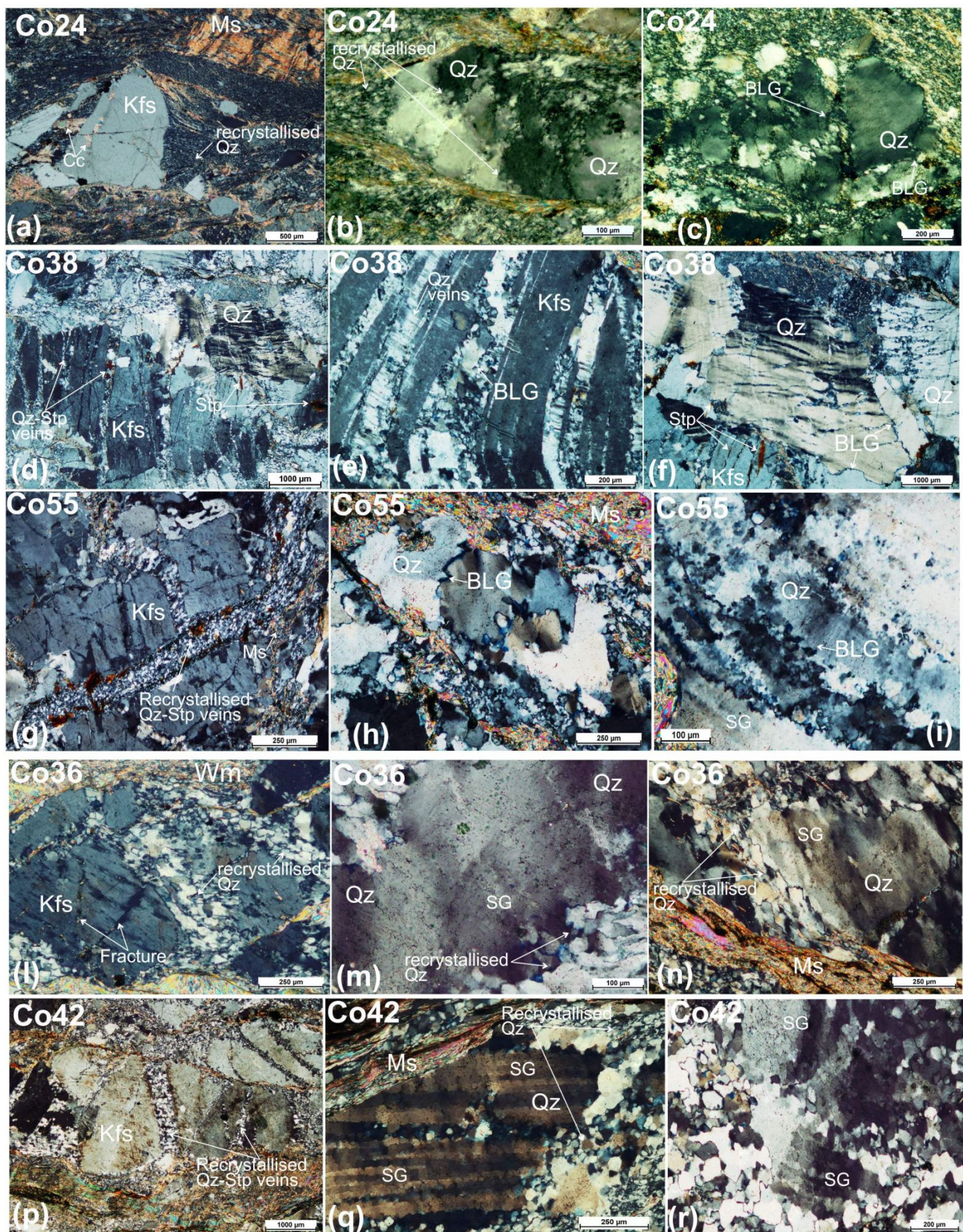
**Table 2 - Bulk and recalculated rock compositions used for pseudosection modelling**

Sample	XRF data			Recalculated(*)		
	Co-24	Co-36	Co-42	Co-24	Co-36	Co-42
Rock Type	Metavolcanic	Granitoid	Granitoid			
<b>SiO<sub>2</sub></b>	72.08	74.70	71.18	71.73	73.20	69.48
<b>TiO<sub>2</sub></b>	0.26	0.18	0.37	0.26	0.18	0.36
<b>Al<sub>2</sub>O<sub>3</sub></b>	13.19	12.26	13.65	13.13	12.01	13.32
<b>Fe<sub>2</sub>O<sub>3</sub></b>	2.57	1.09	3.35			
<b>FeO</b>				2.30	0.98	2.94
<b>MnO</b>	0.09	0.04	0.06			
<b>MgO</b>	0.47	0.46	0.45	0.47	0.45	0.44
<b>CaO</b>	1.61	0.25	1.54	0.40	0.17	0.49
<b>Na<sub>2</sub>O</b>	2.68	3.25	3.50	2.67	3.18	3.42
<b>K<sub>2</sub>O</b>	4.08	4.92	4.60	4.06	4.82	4.49
<b>P<sub>2</sub>O<sub>5</sub></b>	0.07	0.06	0.08			
<b>O<sub>2</sub></b>					0.01	0.06
<b>H<sub>2</sub>O</b>				5.00	5.00	5.00
<b>Sum</b>	97.10	97.21	98.77	100	100.00	100.00

(\*) In the NCKFMASHTO chemical system



### Supplementary Material#1 – Fsp and Qz microfabrics in the studied samples.



Sample CO24 (Crossed Polars)

(a) Fractured K-feldspar (K-Fsp) porphyroblast (igneous) in fine-grained recrystallized quartz (Qz) and white mica (Wm) shear matrix. Large Wm crystals are crenulated, and post-tectonic growth of calcite (Cc) is observed. (b) – (c) Patchy undulose extinction and dynamic recrystallisation in Qz, dominantly assisted by bulging recrystallisation (BLG).

Sample CO38 (Crossed Polars)

(d) Fractured and strained relic (igneous) K-feldspar-quartz assemblage in a fine-grained recrystallizes Qz-Wm matrix. Quartz-stilpnomelane (Stp) veins cut across the K-feldspar-Qz assemblage. (e) Enlargement showing the internal fabric of the Qz veins in K-Fsp. Qz grains show evidence of dynamic recrystallisation assisted by BLG. (f) Healed fractures in relict igneous Qz. Undulose extinction and BLG recrystallisation is observed.

Sample CO55 (Crossed Polars)

(g) Fractured (relic igneous) K-Fsp grains hosting recrystallized Qz veins. (h) – (i). Relic igneous Qz grains showing undulose extinction, deformation lamellae and evidence of dynamic recrystallisation assisted by BLG.

Sample CO36 (Crossed Polars)

(l) Fractured K-Fsp grains surrounded by fine-grained recrystallized Qz grains (early veins). Fracture in K-Fsp do not pass through the recrystallized Qz domains, indicating the differential rheological behavior during rock deformation. (m) Relic (igneous) Qz showing subgrain (SG) formation. (n) Bimodal grain size produced by subgrain rotation recrystallisation in Qz.

Sample CO42 (Crossed Polars)

(o) Fractured K-Fsp grains surrounded by fine-grained recrystallized Qz grains (early veins). (p) – (q) Bimodal grain size produced by subgrain rotation recrystallization in Qz.

## Representative EMPA and chemical formulas of White Mica

Locality Sample Type	#1	#2	#3	#4	#5	#6	#7
SiO <sub>2</sub> (wt%)	50.77	51.06	50.49	50.71	50.37	49.71	50.59
TiO <sub>2</sub>	0.44	0.48	0.39	0.36	0.47	0.37	0.34
Al <sub>2</sub> O <sub>3</sub>	25.18	25.52	25.08	25.28	25.08	24.45	25.21
FeOt	6.79	6.83	7.00	6.67	7.25	7.00	6.90
MnO	0.09	0.09	0.07	0.07	bdl	0.07	0.08
MgO	1.60	1.60	1.67	1.60	1.62	1.61	1.65
CaO	bdl	bdl	bdl	bdl	bdl	0.06	bdl
Na <sub>2</sub> O	0.05	bdl	bdl	0.05	bdl	0.04	0.05
K <sub>2</sub> O	10.55	10.79	10.66	10.32	11.04	10.84	10.82
BaO	0.11	0.14	0.09	0.09	0.12	0.08	0.13
Total	95.58	96.52	95.45	95.15	95.95	94.22	95.77
<i>Formula (11 Oxygens)</i>							
Si (apfu)	3.437	3.428	3.425	3.438	3.416	3.435	3.427
Ti	0.022	0.024	0.020	0.018	0.024	0.019	0.017
Al <sup>Tot</sup>	2.009	2.019	2.005	2.020	2.005	1.991	2.013
Al <sup>[IV]</sup>	0.563	0.572	0.575	0.562	0.584	0.565	0.573
Al <sup>[VI]</sup>	1.446	1.447	1.430	1.458	1.421	1.426	1.440
Fe <sup>2+</sup>	0.278	0.283	0.261	0.258	0.308	0.319	0.282
Fe <sup>3+</sup>	0.107	0.101	0.136	0.120	0.104	0.086	0.109
Mn	0.005	0.005	0.004	0.004	-	0.004	0.005
Mg	0.162	0.161	0.169	0.162	0.164	0.166	0.167
Ca	-	-	-	-	-	-	-
Ba	0.003	0.004	0.003	0.002	0.003	0.002	0.003
Na	0.006	-	-	0.006	-	0.006	0.007
K	0.912	0.924	0.922	0.893	0.956	0.956	0.936
<sup>(a)</sup> XPrI	0.08	0.07	0.07	0.10	0.03	0.03	0.05
<sup>(a)</sup> XTri	0.02	0.02	0.02	0.02	0.02	0.02	0.02
<sup>(a)</sup> XPg	0.01	-	-	0.01	-	0.01	0.01
<sup>(a)</sup> XCel	0.46	0.45	0.44	0.46	0.44	0.45	0.44
<sup>(a)</sup> XMs	0.44	0.46	0.47	0.43	0.51	0.49	0.48

\* FeOt total iron reported as FeO; apfu: atoms per formula unit; bdl: below detection limit.

(a) White mica molar fractions: XPrI: Pyrophyllite, XTri: Trioctahedral substitution, XPg: Paragonite

#9	#10	#11	#12	#38	#39	#1	#2	#3
50.71	51.06	49.59	50.82	49.57	51.28	50.25	50.09	49.61
0.29	0.25	0.42	0.30	0.09	0.05	0.33	0.29	0.44
24.68	25.30	25.04	24.36	25.80	24.14	23.53	24.17	24.02
7.23	6.85	6.75	8.01	7.00	8.72	7.93	8.01	8.01
0.06	0.10	0.06	0.15	0.08	<i>bdl</i>	0.08	0.05	<i>bdl</i>
1.64	1.53	1.50	1.61	1.63	1.66	1.71	1.70	1.62
<i>bdl</i>	<i>bdl</i>	<i>bdl</i>	<i>bdl</i>	0.06	0.10	<i>bdl</i>	<i>bdl</i>	<i>bdl</i>
0.07	<i>bdl</i>	0.06	<i>bdl</i>	0.09	0.07	0.06	0.07	0.06
10.71	10.87	10.77	11.31	11.05	10.97	11.35	11.03	11.07
0.10	0.11	0.11	0.10	<i>bdl</i>	<i>bdl</i>	0.07	0.09	0.09
95.50	96.07	94.30	96.68	95.36	96.99	95.30	95.49	94.91
3.447	3.447	3.418	3.438	3.376	3.447	3.458	3.424	3.418
0.015	0.013	0.022	0.015	0.005	0.002	0.017	0.015	0.023
1.977	2.013	2.034	1.942	2.071	1.913	1.909	1.947	1.951
0.553	0.553	0.582	0.562	0.624	0.553	0.542	0.576	0.582
1.425	1.460	1.452	1.380	1.447	1.360	1.367	1.371	1.369
0.302	0.308	0.305	0.324	0.253	0.308	0.366	0.298	0.319
0.109	0.079	0.084	0.129	0.146	0.182	0.090	0.160	0.142
0.004	0.006	0.003	0.009	0.004	-	0.004	0.003	-
0.166	0.154	0.154	0.163	0.165	0.166	0.176	0.173	0.167
-	-	-	-	0.004	0.007	-	-	-
0.003	0.003	0.003	0.003	-	-	0.002	0.002	0.002
0.010	-	0.009	-	0.012	0.009	0.009	0.009	0.007
0.928	0.936	0.947	0.976	0.961	0.941	0.997	0.962	0.973
0.06	0.06	0.04	0.02	0.02	0.04	-	0.03	0.02
0.02	0.02	0.02	0.02	0.02	0.02	0.02	0.02	0.02
0.01	-	0.01	-	0.01	0.01	0.01	0.01	0.01
0.46	0.46	0.44	0.45	0.38	0.45	0.48	0.44	0.44
0.46	0.47	0.50	0.51	0.57	0.48	0.50	0.51	0.52

nite, XCel: Celadonite; XMs: Muscovite. Trioctahedral substitution is fixed by stoichiometry at XTri=0.02.

CO-24								
Wm1								
#4	#5	#6	#8	#9	#10	#11	#13	#15
50.24	49.26	49.40	49.02	50.03	50.32	50.59	48.27	48.88
0.41	0.53	0.57	0.96	0.35	0.47	0.34	0.50	0.47
22.69	25.39	25.14	25.67	23.43	21.57	21.69	27.67	27.63
8.54	7.12	6.93	6.66	8.25	9.70	9.23	4.58	4.79
0.08	<i>bdl</i>	0.06	0.09	0.09	0.08	0.16	<i>bdl</i>	<i>bdl</i>
1.69	1.51	1.57	1.44	1.61	2.03	2.01	1.24	1.20
<i>bdl</i>	<i>bdl</i>	<i>bdl</i>	0.11	<i>bdl</i>	<i>bdl</i>	<i>bdl</i>	0.18	0.22
0.11	0.06	0.12	0.04	0.05	0.09	0.11	0.45	0.35
11.18	11.35	11.13	11.00	11.12	11.15	11.27	10.24	9.64
<i>bdl</i>	0.13	0.14	0.10	0.07	<i>bdl</i>	<i>bdl</i>	0.07	<i>bdl</i>
94.94	95.35	95.07	95.08	95.00	95.40	95.40	93.21	93.17
3.476	3.377	3.393	3.362	3.450	3.470	3.490	3.343	3.360
0.021	0.027	0.029	0.050	0.018	0.024	0.018	0.026	0.024
1.850	2.051	2.035	2.075	1.905	1.753	1.763	2.258	2.239
0.524	0.623	0.607	0.638	0.550	0.530	0.510	0.657	0.640
1.326	1.429	1.428	1.436	1.355	1.223	1.254	1.600	1.598
0.385	0.321	0.319	0.309	0.345	0.338	0.360	0.265	0.247
0.108	0.087	0.079	0.073	0.130	0.221	0.173	-	0.028
0.005	-	0.004	0.005	0.005	0.005	0.009	-	-
0.174	0.155	0.161	0.147	0.166	0.209	0.207	0.128	0.123
-	-	-	0.008	-	-	-	0.013	0.016
-	0.003	0.004	0.003	0.002	-	-	0.002	-
0.015	0.009	0.015	0.006	0.007	0.012	0.015	0.060	0.046
0.987	0.993	0.976	0.963	0.978	0.980	0.992	0.905	0.845
-	-	0.00	0.02	0.01	0.01	-	0.02	0.09
0.02	0.02	0.02	0.02	0.02	0.02	0.02	0.02	0.02
0.02	0.01	0.02	0.01	0.01	0.01	0.02	0.06	0.05
0.50	0.40	0.42	0.41	0.47	0.49	0.51	0.37	0.38
0.48	0.57	0.54	0.54	0.50	0.48	0.47	0.52	0.45

#17	#18	#19	#20	#21	#22	#23	#24	#25
50.32	48.89	48.87	50.10	50.05	49.51	49.62	49.29	49.70
0.29	0.67	0.21	0.28	0.19	0.17	0.14	0.15	0.19
22.07	25.91	25.00	24.83	25.33	24.51	25.03	25.11	24.31
8.94	5.76	6.85	6.59	6.93	7.60	7.46	7.01	7.90
0.07	0.09	<i>bdl</i>	0.08	<i>bdl</i>	0.07	0.08	<i>bdl</i>	0.13
1.97	1.56	1.69	1.56	1.61	1.65	1.57	1.57	1.59
<i>bdl</i>	0.07	<i>bdl</i>	0.04	<i>bdl</i>	<i>bdl</i>	0.07	<i>bdl</i>	<i>bdl</i>
0.09	0.27	0.08	0.84	0.39	0.10	<i>bdl</i>	0.09	0.17
11.21	10.78	11.19	10.40	11.01	11.00	11.09	11.48	10.95
<i>bdl</i>	0.11	0.13	0.07	0.10	0.11	0.10	0.08	0.11
94.94	94.10	94.02	94.79	95.60	94.71	95.16	94.76	95.03
3.482	3.378	3.392	3.448	3.415	3.410	3.400	3.403	3.416
0.015	0.035	0.011	0.014	0.010	0.009	0.007	0.008	0.010
1.800	2.109	2.045	2.014	2.037	1.990	2.021	2.043	1.969
0.518	0.622	0.608	0.552	0.585	0.590	0.600	0.597	0.584
1.281	1.487	1.437	1.462	1.451	1.400	1.421	1.445	1.386
0.352	0.309	0.302	0.380	0.337	0.292	0.291	0.339	0.306
0.165	0.024	0.095	-	0.059	0.146	0.136	0.065	0.148
0.004	0.005	-	0.005	-	0.004	0.005	-	0.007
0.203	0.160	0.175	0.160	0.163	0.169	0.160	0.162	0.163
-	0.005	-	0.003	-	-	0.005	-	-
-	0.003	0.004	0.002	0.003	0.003	0.003	0.002	0.003
0.012	0.036	0.011	0.112	0.052	0.013	-	0.011	0.022
0.990	0.950	0.991	0.913	0.958	0.967	0.970	1.011	0.960
-	0.01	-	-	-	0.02	0.02	-	0.01
0.02	0.02	0.02	0.02	0.02	0.02	0.02	0.02	0.02
0.01	0.04	0.01	0.11	0.05	0.01	-	0.01	0.02
0.50	0.41	0.40	0.46	0.42	0.42	0.41	0.41	0.43
0.48	0.53	0.57	0.41	0.51	0.54	0.55	0.56	0.52

		Transect-						
#26	#27	#2	#4	#5	#9	#11	#15	#16
48.75	49.67	50.56	49.66	49.85	49.70	49.84	49.61	49.42
0.46	0.41	0.07	0.10	0.08	0.09	0.08	0.12	0.06
24.51	24.31	22.88	24.51	24.53	24.47	22.31	23.38	23.58
7.30	7.33	7.44	7.00	6.91	6.91	7.86	7.52	7.49
0.07	0.11	0.10	0.04	0.07	0.07	0.08	0.10	0.11
1.47	1.55	2.77	2.38	2.48	2.46	2.59	2.65	2.39
0.09	0.06	0.09	bdl	bdl	0.04	bdl	0.05	0.08
0.39	0.24	0.21	0.08	0.07	0.10	0.07	bdl	0.06
10.63	10.87	10.86	11.50	11.37	11.24	11.14	11.41	11.20
0.10	0.08	0.06	0.20	0.14	0.14	0.08	0.10	0.04
93.76	94.62	95.03	95.47	95.50	95.22	94.05	94.94	94.42
3.399	3.431	3.458	3.395	3.396	3.395	3.461	3.410	3.412
0.024	0.021	0.004	0.005	0.004	0.004	0.004	0.006	0.003
2.015	1.979	1.844	1.975	1.970	1.971	1.825	1.894	1.919
0.601	0.569	0.542	0.605	0.604	0.605	0.539	0.590	0.588
1.414	1.410	1.303	1.370	1.366	1.366	1.286	1.304	1.332
0.344	0.349	0.226	0.244	0.214	0.211	0.257	0.216	0.230
0.081	0.075	0.200	0.156	0.180	0.184	0.199	0.217	0.202
0.004	0.006	0.006	0.003	0.004	0.004	0.005	0.006	0.006
0.152	0.160	0.282	0.242	0.252	0.251	0.268	0.272	0.246
0.006	0.004	0.007	-	-	0.003	-	0.004	0.006
0.003	0.002	0.002	0.005	0.004	0.004	0.002	0.003	0.001
0.053	0.032	0.028	0.011	0.009	0.013	0.009	-	0.007
0.945	0.958	0.947	1.003	0.988	0.980	0.987	1.001	0.986
-	0.00	0.02	-	-	0.00	-	-	-
0.02	0.02	0.02	0.02	0.02	0.02	0.02	0.02	0.02
0.05	0.03	0.03	0.01	0.01	0.01	0.01	-	0.01
0.42	0.45	0.46	0.40	0.40	0.40	0.46	0.42	0.42
0.50	0.50	0.47	0.57	0.57	0.57	0.51	0.56	0.56

<b>-1 (Castirla)</b>								
<b>CO-25</b>								
<b>Wm2</b>								
#18	#19	#21	#25	#27	#30	#33	#35	#36
50.77	49.78	49.93	49.56	49.48	49.56	50.07	51.49	49.75
0.08	0.06	0.09	0.08	0.09	0.08	0.13	<i>bdl</i>	0.06
24.58	24.43	24.19	24.29	23.82	24.25	24.48	22.48	24.61
6.22	6.71	6.95	7.08	7.12	6.64	6.52	6.73	6.71
0.10	<i>bdl</i>	0.10	0.14	0.14	0.08	<i>bdl</i>	0.07	0.08
2.67	2.41	2.46	2.26	2.33	2.27	2.53	3.11	2.36
<i>bdl</i>	<i>bdl</i>	<i>bdl</i>	0.11	<i>bdl</i>	<i>bdl</i>	0.13	<i>bdl</i>	<i>bdl</i>
0.06	<i>bdl</i>	0.07	0.13	<i>bdl</i>	0.37	0.10	<i>bdl</i>	<i>bdl</i>
11.27	11.54	11.45	11.04	11.67	11.18	10.93	11.36	11.59
<i>bdl</i>	0.14	0.09	0.16	0.12	0.15	0.07	<i>bdl</i>	0.10
95.75	95.07	95.34	94.85	94.77	94.58	94.96	95.25	95.26
3.432	3.412	3.413	3.403	3.417	3.421	3.415	3.509	3.403
0.004	0.003	0.005	0.004	0.005	0.004	0.007	-	0.003
1.958	1.973	1.949	1.966	1.939	1.973	1.967	1.806	1.984
0.568	0.588	0.587	0.597	0.583	0.579	0.585	0.491	0.597
1.390	1.385	1.361	1.370	1.356	1.394	1.382	1.315	1.387
0.204	0.250	0.234	0.237	0.273	0.294	0.209	0.245	0.242
0.148	0.134	0.163	0.169	0.138	0.090	0.163	0.138	0.142
0.006	-	0.006	0.008	0.008	0.005	-	0.004	0.005
0.269	0.246	0.251	0.231	0.240	0.234	0.258	0.316	0.241
-	-	-	0.008	-	-	0.009	-	-
-	0.004	0.003	0.004	0.003	0.004	0.002	-	0.003
0.008	-	0.010	0.017	-	0.049	0.013	-	-
0.972	1.009	0.999	0.967	1.028	0.984	0.951	0.987	1.012
0.02	-	-	0.00	-	-	0.02	0.01	-
0.02	0.02	0.02	0.02	0.02	0.02	0.02	0.02	0.02
0.01	-	0.01	0.02	-	0.05	0.01	-	-
0.44	0.42	0.42	0.41	0.42	0.43	0.42	0.51	0.41
0.53	0.57	0.56	0.55	0.56	0.51	0.52	0.47	0.58

#37	#38	#39	#40	#41	#43	#44	#45	#46
48.58	49.20	48.34	49.33	48.74	49.17	48.55	49.09	49.38
0.07	0.11	0.07	0.07	<i>bdl</i>	0.07	0.05	0.06	0.07
24.97	25.23	24.68	24.48	24.82	24.60	24.47	24.30	24.26
7.07	7.06	6.47	6.76	6.44	6.75	6.47	6.67	6.71
0.08	0.05	0.11	0.15	0.10	0.11	0.11	0.09	0.05
2.45	2.49	2.32	2.34	2.23	2.25	2.34	2.36	2.31
<i>bdl</i>								
<i>bdl</i>	0.05	0.05	0.11	0.07	0.07	0.08	0.07	0.08
11.55	11.36	11.56	11.49	11.46	11.41	11.54	11.32	11.33
0.20	0.16	0.16	0.18	0.16	0.18	0.19	0.15	0.20
94.97	95.69	93.76	94.91	94.02	94.62	93.81	94.12	94.39
3.335	3.340	3.367	3.394	3.379	3.390	3.382	3.399	3.413
0.003	0.005	0.004	0.003	-	0.003	0.003	0.003	0.003
2.020	2.019	2.026	1.985	2.028	1.999	2.009	1.982	1.976
0.665	0.660	0.633	0.606	0.621	0.610	0.618	0.601	0.587
1.355	1.359	1.392	1.379	1.408	1.389	1.390	1.381	1.389
0.172	0.149	0.227	0.243	0.236	0.238	0.245	0.232	0.257
0.234	0.252	0.149	0.146	0.137	0.151	0.132	0.154	0.130
0.005	0.003	0.007	0.009	0.006	0.007	0.007	0.005	0.003
0.251	0.252	0.240	0.240	0.231	0.232	0.243	0.244	0.237
0.005	0.004	0.004	0.005	0.004	0.005	0.005	0.004	0.005
-	0.006	0.007	0.015	0.009	0.009	0.011	0.009	0.011
1.011	0.984	1.028	1.009	1.014	1.004	1.025	1.000	0.999
-	0.01	-	-	-	-	-	-	-
0.02	0.02	0.02	0.02	0.02	0.02	0.02	0.02	0.02
-	0.01	0.01	0.01	0.01	0.01	0.01	0.01	0.01
0.34	0.35	0.37	0.40	0.38	0.39	0.38	0.40	0.42
0.64	0.63	0.61	0.57	0.60	0.58	0.59	0.57	0.56

#47	#48	#49	#1	#2	Wm1			
					#8	#9	#11	#12
49.02	49.23	49.39	50.69	49.67	49.01	49.40	48.61	48.73
0.06	0.05	<i>bdl</i>	0.07	0.11	0.23	0.09	0.10	0.11
24.25	24.49	24.46	22.68	24.58	24.23	25.85	25.43	25.87
6.43	6.45	6.40	6.76	6.89	5.56	4.62	5.41	5.11
0.17	0.14	0.09	0.09	0.13	<i>bdl</i>	<i>bdl</i>	<i>bdl</i>	<i>bdl</i>
2.39	2.54	2.47	2.87	2.34	4.34	3.83	4.35	4.16
<i>bdl</i>	<i>bdl</i>	<i>bdl</i>	<i>bdl</i>	<i>bdl</i>	0.04	0.06	0.05	0.13
0.07	<i>bdl</i>	0.08	0.07	<i>bdl</i>	0.05	0.10	0.08	0.06
11.42	11.58	11.48	11.27	11.54	10.97	9.66	9.59	9.70
0.18	0.15	0.16	0.06	0.16	<i>bdl</i>	<i>bdl</i>	<i>bdl</i>	<i>bdl</i>
93.98	94.63	94.52	94.55	95.42	94.42	93.61	93.62	93.87
3.403	3.390	3.404	3.488	3.394	3.320	3.322	3.263	3.268
0.003	0.003	-	0.003	0.005	0.012	0.005	0.005	0.005
1.984	1.988	1.987	1.840	1.980	1.934	2.049	2.012	2.045
0.597	0.610	0.596	0.512	0.606	0.680	0.678	0.737	0.732
1.387	1.377	1.391	1.328	1.374	1.254	1.372	1.276	1.313
0.239	0.214	0.239	0.259	0.237	-	-	-	-
0.134	0.157	0.130	0.130	0.157	0.315	0.260	0.304	0.287
0.010	0.008	0.005	0.005	0.008	-	-	-	-
0.247	0.261	0.253	0.294	0.239	0.438	0.384	0.435	0.415
-	-	-	-	-	0.003	0.005	0.003	0.010
0.005	0.004	0.004	0.002	0.004	-	-	-	-
0.009	-	0.011	0.009	-	0.007	0.013	0.010	0.008
1.012	1.017	1.009	0.989	1.006	0.948	0.829	0.821	0.830
-	-	-	-	-	0.04	0.15	0.17	0.15
0.02	0.02	0.02	0.02	0.02	0.02	0.02	0.02	0.02
0.01	-	0.01	0.01	-	0.01	0.01	0.01	0.01
0.41	0.39	0.41	0.49	0.40	0.33	0.33	0.27	0.27
0.57	0.59	0.57	0.48	0.58	0.61	0.49	0.54	0.54

CO-38								
#31	#34	#3	#4	#5	#7	#14	#35	Wr #38
48.37	48.40	50.16	48.89	49.70	50.09	49.72	49.78	49.15
0.17	0.41	0.23	0.24	0.28	0.23	0.13	0.41	0.13
22.11	22.27	22.97	22.22	22.67	24.07	24.80	22.66	22.98
10.67	10.12	5.72	6.51	6.17	5.03	4.89	7.63	9.18
0.14	0.14	0.06	bdl	bdl	bdl	bdl	0.14	0.11
2.68	2.78	4.73	4.74	4.80	4.36	4.09	2.94	2.63
0.16	0.22	0.05	bdl	bdl	0.09	bdl	0.28	bdl
bdl	0.08	bdl	bdl	bdl	0.04	0.06	0.05	bdl
10.93	10.99	11.02	10.46	10.65	10.46	10.24	10.98	11.19
bdl								
95.22	95.39	94.94	93.06	94.28	94.36	93.93	94.87	95.37
3.325	3.323	3.382	3.353	3.363	3.376	3.354	3.418	3.361
0.009	0.021	0.012	0.012	0.014	0.011	0.007	0.021	0.006
1.791	1.802	1.825	1.796	1.808	1.912	1.972	1.834	1.853
0.675	0.677	0.618	0.647	0.637	0.624	0.646	0.582	0.639
1.116	1.126	1.207	1.149	1.172	1.287	1.326	1.252	1.214
0.099	0.117	-	-	-	-	-	0.201	0.137
0.514	0.464	0.322	0.373	0.349	0.284	0.276	0.237	0.389
0.008	0.008	0.004	-	-	-	-	0.008	0.006
0.274	0.284	0.475	0.485	0.484	0.438	0.412	0.301	0.268
0.012	0.016	0.003	-	-	0.007	-	0.021	0.002
-	0.010	-	-	-	0.005	0.007	-	0.003
0.959	0.963	0.948	0.915	0.920	0.899	0.881	0.962	0.977
0.02	0.01	0.05	0.08	0.08	0.09	0.11	0.01	0.02
0.02	0.02	0.02	0.02	0.02	0.02	0.02	0.02	0.02
-	0.01	-	-	-	0.01	0.01	-	0.00
0.33	0.34	0.39	0.37	0.38	0.39	0.36	0.44	0.37
0.61	0.61	0.54	0.54	0.53	0.50	0.51	0.51	0.60

							#80	#81
#40	#44	#45	#3	#4	#8	#11		
48.92	49.92	50.17	51.43	50.51	51.39	51.44	46.43	47.08
0.29	<i>bdl</i>	<i>bdl</i>	<i>bdl</i>	<i>bdl</i>	<i>bdl</i>	0.06	0.27	0.12
22.49	22.16	22.29	22.43	22.78	22.90	21.48	33.26	27.61
9.02	8.57	8.37	7.97	6.62	6.91	8.90	2.20	5.51
0.15	0.19	0.15	0.30	0.19	0.34	0.22	0.06	0.11
2.61	2.37	2.37	2.69	2.64	2.78	2.71	1.03	2.49
0.18	<i>bdl</i>	<i>bdl</i>	<i>bdl</i>	<i>bdl</i>	0.04	<i>bdl</i>	<i>bdl</i>	<i>bdl</i>
0.05	0.05	<i>bdl</i>	<i>bdl</i>	<i>bdl</i>	<i>bdl</i>	<i>bdl</i>	0.18	0.16
10.87	11.22	11.46	11.37	11.15	10.98	10.29	11.11	10.77
<i>bdl</i>	0.23	0.13						
94.59	94.48	94.82	96.19	93.89	95.34	95.10	94.76	93.98
3.376	3.458	3.467	3.486	3.495	3.491	3.500	3.132	3.216
0.015	-	-	-	-	-	0.003	0.014	0.006
1.830	1.809	1.816	1.792	1.858	1.834	1.722	2.644	2.223
0.624	0.542	0.533	0.514	0.505	0.509	0.500	0.868	0.784
1.206	1.267	1.283	1.279	1.353	1.325	1.223	1.775	1.439
0.165	0.263	0.286	0.242	0.259	0.213	0.169	0.095	-
0.355	0.234	0.198	0.210	0.124	0.179	0.337	0.029	0.315
0.009	0.011	0.009	0.017	0.011	0.020	0.013	0.003	0.006
0.269	0.244	0.244	0.271	0.272	0.281	0.275	0.103	0.253
0.013	-	-	-	-	0.003	-	-	-
-	-	-	-	-	-	-	0.006	0.004
0.007	0.007	-	-	-	-	-	0.023	0.021
0.957	0.991	1.010	0.983	0.985	0.951	0.893	0.956	0.939
0.02	0.00	0.00	0.02	0.01	0.04	0.11	0.01	0.04
0.02	0.02	0.02	0.02	0.02	0.02	0.02	0.02	0.02
0.01	0.01	-	-	-	-	-	0.02	0.02
0.39	0.46	0.47	0.49	0.50	0.49	0.50	0.15	0.22
0.56	0.52	0.52	0.49	0.48	0.45	0.38	0.80	0.70

Wm1						#50	#51	#52
#82	#83	#87	#88	#95	#84			
45.73	45.27	46.64	45.07	45.60	48.73	49.79	49.77	49.66
0.44	0.04	<i>bdl</i>	0.06	<i>bdl</i>	<i>bdl</i>	<i>bdl</i>	<i>bdl</i>	0.06
28.34	35.82	32.74	34.69	35.32	28.82	21.29	21.29	20.49
5.74	1.43	2.91	1.93	1.27	3.57	7.84	7.52	7.63
0.15	<i>bdl</i>	0.17	0.12	0.36	<i>bdl</i>	0.19	0.17	0.09
2.63	0.35	0.92	0.31	0.29	2.32	3.85	3.97	4.04
<i>bdl</i>								
0.18	0.23	0.12	0.20	0.12	0.12	<i>bdl</i>	0.06	<i>bdl</i>
11.10	11.09	11.32	11.16	11.31	11.44	11.34	11.01	11.49
0.27	0.07	0.20	0.08	0.28	0.07	<i>bdl</i>	<i>bdl</i>	<i>bdl</i>
94.60	94.31	95.02	93.62	94.54	95.06	94.30	93.79	93.47
3.117	3.054	3.148	3.077	3.083	3.290	3.431	3.435	3.462
0.023	0.002	-	0.003	-	-	-	-	0.003
2.277	2.848	2.604	2.791	2.815	2.293	1.729	1.732	1.684
0.883	0.946	0.852	0.923	0.917	0.710	0.569	0.565	0.538
1.393	1.902	1.752	1.868	1.898	1.583	1.160	1.166	1.146
-	0.069	0.112	0.109	0.072	0.120	0.089	0.060	0.130
0.327	0.012	0.052	0.001	-	0.082	0.363	0.375	0.315
0.009	-	0.010	0.007	0.021	0.002	0.011	0.010	0.005
0.267	0.036	0.092	0.031	0.029	0.234	0.395	0.408	0.420
0.007	0.002	0.005	0.002	0.007	0.002	-	-	-
0.024	0.030	0.016	0.026	0.015	0.016	-	0.008	-
0.965	0.955	0.975	0.972	0.975	0.985	0.997	0.969	1.022
-	0.01	-	-	-	-	-	0.02	-
0.02	0.02	0.02	0.02	0.02	0.02	0.02	0.02	0.02
0.02	0.03	0.02	0.03	0.02	0.02	-	0.01	-
0.14	0.06	0.15	0.08	0.08	0.29	0.43	0.44	0.47
0.82	0.89	0.81	0.88	0.88	0.68	0.55	0.52	0.52

CO-35								
Wm2								
#53	#54	#55	#66	#68	#69	#70	#85	#86
50.37	50.41	50.45	51.16	49.04	49.95	51.11	49.90	51.53
<i>bdl</i>	<i>bdl</i>	<i>bdl</i>	<i>bdl</i>	0.14	0.05	<i>bdl</i>	<i>bdl</i>	<i>bdl</i>
20.93	21.43	21.33	20.74	20.46	21.35	20.02	20.78	21.25
7.64	6.58	7.05	7.07	7.84	6.82	7.61	7.64	6.98
0.10	0.13	0.10	0.20	0.18	0.16	0.07	0.11	0.14
4.00	3.74	4.12	4.05	4.42	3.86	4.17	4.13	4.02
<i>bdl</i>	<i>bdl</i>	<i>bdl</i>	<i>bdl</i>	0.09	<i>bdl</i>	<i>bdl</i>	<i>bdl</i>	<i>bdl</i>
0.10	0.12	0.04	<i>bdl</i>	0.05	<i>bdl</i>	<i>bdl</i>	0.06	<i>bdl</i>
11.51	10.95	11.26	11.30	11.26	11.24	11.30	11.53	11.42
<i>bdl</i>	0.07	<i>bdl</i>	0.06	<i>bdl</i>	0.04	<i>bdl</i>	<i>bdl</i>	<i>bdl</i>
94.64	93.43	94.36	94.57	93.49	93.48	94.29	94.15	95.34
3.466	3.494	3.462	3.510	3.410	3.467	3.522	3.451	3.504
-	-	-	-	0.007	0.003	-	-	-
1.698	1.750	1.725	1.677	1.677	1.746	1.626	1.694	1.703
0.534	0.506	0.538	0.490	0.590	0.533	0.478	0.549	0.496
1.164	1.244	1.187	1.187	1.087	1.213	1.148	1.145	1.207
0.142	0.154	0.091	0.143	0.028	0.126	0.149	0.105	0.144
0.297	0.227	0.313	0.263	0.428	0.270	0.290	0.337	0.253
0.006	0.008	0.006	0.011	0.011	0.010	0.004	0.007	0.008
0.410	0.386	0.421	0.414	0.459	0.399	0.429	0.426	0.408
-	-	-	-	0.007	0.003	-	-	-
-	0.002	-	0.002	-	0.001	-	-	-
0.013	0.015	0.006	-	0.007	-	-	0.008	-
1.010	0.968	0.986	0.989	0.999	0.996	0.994	1.017	0.990
-	0.01	0.01	-	-	-	-	-	0.01
0.02	0.02	0.02	0.02	0.02	0.02	0.02	0.02	0.02
0.01	0.02	0.01	-	0.01	-	-	0.01	-
0.47	0.49	0.46	0.51	0.42	0.47	0.52	0.45	0.50
0.51	0.46	0.51	0.47	0.56	0.51	0.46	0.53	0.48

#91	#92	#93	#96	#100	#101	#102	#7	#10
50.24	49.79	50.62	49.80	50.41	50.32	50.62	45.57	45.18
<i>bdl</i>	<i>bdl</i>	<i>bdl</i>	<i>bdl</i>	0.11	0.04	<i>bdl</i>	0.18	0.20
21.30	21.97	21.53	20.34	19.94	20.69	16.99	36.13	36.38
7.33	7.21	6.98	8.12	7.92	7.40	10.88	2.21	1.86
0.08	0.13	0.12	0.14	0.20	0.19	0.20	0.08	0.08
4.07	3.66	3.78	4.17	4.50	4.17	3.34	0.21	0.17
<i>bdl</i>	0.09	<i>bdl</i>	<i>bdl</i>	0.04	<i>bdl</i>	<i>bdl</i>	<i>bdl</i>	<i>bdl</i>
0.07	<i>bdl</i>	<i>bdl</i>	0.06	<i>bdl</i>	<i>bdl</i>	<i>bdl</i>	0.59	0.51
11.43	11.19	11.39	11.39	11.28	11.61	11.35	11.18	11.12
<i>bdl</i>								
94.53	94.04	94.42	94.02	94.39	94.42	93.37	96.14	95.50
3.452	3.434	3.480	3.449	3.469	3.470	3.590	3.031	3.019
-	-	-	-	0.006	0.002	-	0.009	0.010
1.725	1.786	1.744	1.660	1.617	1.681	1.420	2.832	2.865
0.548	0.566	0.520	0.551	0.531	0.530	0.410	0.969	0.981
1.177	1.220	1.224	1.110	1.086	1.151	1.010	1.863	1.885
0.103	0.113	0.150	0.084	0.063	0.119	0.314	0.099	0.083
0.318	0.303	0.252	0.386	0.393	0.308	0.331	0.024	0.021
0.005	0.007	0.007	0.008	0.011	0.011	0.012	0.005	0.004
0.417	0.376	0.387	0.431	0.461	0.429	0.353	0.021	0.017
-	0.007	-	-	0.003	-	-	-	-
0.010	-	-	0.008	-	-	-	0.075	0.066
1.002	0.985	0.999	1.006	0.990	1.022	1.027	0.949	0.948
-	0.01	-	-	-	-	-	-	-
0.02	0.02	0.02	0.02	0.02	0.02	0.02	0.02	0.02
0.01	-	-	0.01	-	-	-	0.07	0.07
0.45	0.43	0.48	0.45	0.47	0.47	0.59	0.04	0.03
0.53	0.54	0.51	0.53	0.51	0.52	0.40	0.88	0.90

Transect2 (Vivario-Venaco)								
Wm1								
#12	#23	#6	#7	#8	#10	#11	#1	#2
45.51	48.10	44.24	44.89	46.29	45.25	46.17	49.08	48.31
0.44	0.22	0.26	0.24	0.13	0.22	0.19	<i>bdl</i>	0.05
34.42	33.55	31.07	30.25	30.85	30.43	30.28	24.38	25.01
3.72	1.99	4.30	4.47	3.71	4.32	4.35	6.73	6.77
0.13	<i>bdl</i>	0.21	0.16	0.20	0.17	0.12	0.18	0.14
0.30	1.27	1.31	1.47	1.41	1.40	1.41	3.61	3.36
0.10	<i>bdl</i>							
0.46	0.90	0.31	0.36	0.43	0.44	0.43	0.05	0.05
11.08	9.69	10.38	10.51	10.68	10.48	10.37	11.34	11.53
<i>bdl</i>	0.13	0.07	0.05	<i>bdl</i>	<i>bdl</i>	0.05	<i>bdl</i>	0.04
96.15	95.85	92.14	92.39	93.70	92.70	93.37	95.36	95.26
3.042	3.169	3.069	3.114	3.162	3.127	3.164	3.320	3.282
0.022	0.011	0.013	0.013	0.007	0.011	0.010	-	0.003
2.712	2.605	2.540	2.473	2.484	2.478	2.446	1.944	2.003
0.958	0.831	0.931	0.886	0.838	0.873	0.836	0.680	0.718
1.753	1.775	1.609	1.587	1.646	1.606	1.610	1.264	1.285
0.105	0.056	-	0.006	0.063	0.032	0.052	-	0.005
0.103	0.054	0.250	0.254	0.149	0.218	0.198	0.381	0.380
0.007	-	0.012	0.009	0.012	0.010	0.007	0.010	0.008
0.029	0.124	0.135	0.152	0.144	0.144	0.144	0.364	0.340
0.007	-	-	-	-	-	-	-	-
-	0.003	0.002	0.001	-	-	0.001	-	0.001
0.060	0.115	0.041	0.048	0.057	0.058	0.057	0.007	0.007
0.944	0.815	0.919	0.930	0.931	0.924	0.907	0.979	0.999
0.00	0.07	0.04	0.02	0.01	0.02	0.03	0.01	-
0.02	0.02	0.02	0.02	0.02	0.02	0.02	0.02	0.02
0.06	0.12	0.04	0.05	0.06	0.06	0.06	0.01	0.01
0.06	0.18	0.08	0.13	0.17	0.14	0.17	0.32	0.28
0.86	0.62	0.82	0.79	0.75	0.77	0.72	0.65	0.70

CO-36								
#4	#5	#6	#8	#9	#11	#13	#17	#18
49.91	49.64	51.21	51.71	49.23	50.52	49.04	51.76	50.99
<i>bdl</i>	0.05	<i>bdl</i>	<i>bdl</i>	0.08	<i>bdl</i>	0.06	0.10	0.09
23.92	24.85	23.62	24.16	23.66	24.44	23.45	23.62	23.77
5.64	5.70	6.32	4.69	7.20	5.11	7.52	5.35	5.55
0.11	0.09	0.12	0.15	0.13	0.12	0.14	0.17	0.11
3.24	3.31	3.23	3.10	3.13	3.19	3.29	3.02	3.04
<i>bdl</i>	<i>bdl</i>	<i>bdl</i>	<i>bdl</i>	0.06	<i>bdl</i>	0.08	<i>bdl</i>	0.36
<i>bdl</i>	<i>bdl</i>	<i>bdl</i>	0.04	0.05	<i>bdl</i>	<i>bdl</i>	0.05	<i>bdl</i>
11.57	11.55	11.51	12.00	11.23	11.71	11.24	11.94	11.51
<i>bdl</i>	0.05	<i>bdl</i>	0.08	0.06	0.07	<i>bdl</i>	0.05	0.08
94.38	95.24	96.01	95.92	94.83	95.16	94.81	96.06	95.49
3.424	3.367	3.454	3.503	3.369	3.438	3.353	3.509	3.475
-	0.003	-	-	0.004	-	0.003	0.005	0.005
1.934	1.987	1.877	1.929	1.908	1.960	1.890	1.887	1.909
0.576	0.633	0.546	0.497	0.631	0.562	0.647	0.491	0.525
1.358	1.354	1.331	1.432	1.277	1.398	1.244	1.396	1.384
0.168	0.096	0.177	0.266	0.105	0.189	0.069	0.303	0.283
0.155	0.227	0.179	-	0.307	0.102	0.361	0.001	0.033
0.006	0.005	0.007	0.008	0.008	0.007	0.008	0.010	0.006
0.331	0.335	0.324	0.313	0.319	0.324	0.335	0.305	0.309
-	-	-	-	0.004	-	0.006	-	0.026
-	0.001	-	0.002	0.002	0.002	-	0.001	0.002
-	-	-	0.005	0.007	-	-	0.007	-
1.013	1.000	0.990	1.037	0.980	1.017	0.981	1.033	1.001
-	-	0.01	-	0.01	-	0.01	-	-
0.02	0.02	0.02	0.02	0.02	0.02	0.02	0.02	0.02
-	-	-	0.01	0.01	-	-	0.01	-
0.43	0.37	0.45	0.50	0.37	0.44	0.36	0.51	0.48
0.56	0.62	0.53	0.48	0.60	0.55	0.61	0.47	0.48

Wm2								
#19	#24	#25	#3	#4	#12	#13	#14	#15
51.49	51.19	51.24	50.71	51.03	50.49	51.70	49.71	51.33
0.08	0.18	0.06	0.04	<i>bdl</i>	0.05	<i>bdl</i>	0.06	<i>bdl</i>
23.55	23.60	24.22	24.10	23.58	24.38	23.90	25.35	23.58
5.45	6.05	5.44	5.48	5.20	5.35	4.66	5.56	5.03
0.11	0.10	0.08	0.18	0.18	0.12	0.10	<i>bdl</i>	0.12
3.32	3.10	3.10	3.24	3.13	3.16	3.19	2.96	3.25
<i>bdl</i>	0.05	<i>bdl</i>						
<i>bdl</i>	0.05	0.07	<i>bdl</i>	0.09	0.05	<i>bdl</i>	0.11	0.06
11.48	10.97	11.67	11.34	11.17	11.50	11.44	11.11	11.33
0.08	0.07	0.10	0.06	0.06	0.06	0.06	0.09	0.09
95.56	95.30	95.96	95.15	94.42	95.16	95.04	94.99	94.79
3.486	3.466	3.464	3.441	3.491	3.433	3.512	3.373	3.500
0.004	0.009	0.003	0.002	-	0.002	-	0.003	-
1.879	1.883	1.929	1.927	1.901	1.954	1.913	2.027	1.895
0.514	0.534	0.536	0.559	0.509	0.567	0.488	0.627	0.500
1.366	1.350	1.393	1.369	1.392	1.387	1.426	1.400	1.394
0.206	0.177	0.232	0.155	0.214	0.176	0.244	0.122	0.224
0.103	0.165	0.076	0.156	0.084	0.128	0.021	0.194	0.063
0.006	0.006	0.005	0.011	0.010	0.007	0.006	-	0.007
0.336	0.313	0.312	0.328	0.319	0.320	0.323	0.299	0.330
-	-	-	-	-	-	-	0.003	-
0.002	0.002	0.003	0.002	0.002	0.002	0.002	0.002	0.002
-	0.006	0.009	-	0.012	0.007	-	0.014	0.008
0.991	0.948	1.006	0.982	0.975	0.997	0.992	0.961	0.985
0.01	0.04	-	0.01	0.01	-	0.00	0.02	0.00
0.02	0.02	0.02	0.02	0.02	0.02	0.02	0.02	0.02
-	0.01	0.01	-	0.01	0.01	-	0.01	0.01
0.49	0.48	0.47	0.44	0.49	0.44	0.51	0.38	0.50
0.49	0.46	0.51	0.53	0.47	0.55	0.47	0.58	0.47

#16	#17	#18	#19	#20	#21	#22	#30	#15
50.37	50.78	50.58	50.32	51.92	51.26	53.72	52.33	52.68
0.06	<i>bdl</i>	<i>bdl</i>	<i>bdl</i>	0.04	0.04	0.10	0.08	0.06
23.08	23.98	24.00	23.97	23.65	23.63	22.80	23.52	22.38
5.61	5.33	5.57	6.15	4.94	5.62	6.10	5.58	6.41
0.11	0.08	0.13	0.12	0.11	0.09	0.20	0.15	0.15
3.34	3.30	3.52	3.45	3.13	3.42	2.97	2.97	3.16
0.05	<i>bdl</i>	<i>bdl</i>	0.05	0.04	<i>bdl</i>	<i>bdl</i>	0.06	0.05
<i>bdl</i>	0.07	0.06	0.04	0.07	<i>bdl</i>	<i>bdl</i>	<i>bdl</i>	<i>bdl</i>
11.14	11.47	11.48	11.40	11.53	11.29	11.62	11.36	11.09
0.04	<i>bdl</i>	<i>bdl</i>	<i>bdl</i>	0.05	<i>bdl</i>	0.05	0.11	0.09
93.80	95.00	95.33	95.50	95.49	95.34	97.56	96.15	96.08
3.470	3.455	3.425	3.404	3.523	3.467	3.578	3.527	3.551
0.003	-	-	-	0.002	0.002	0.005	0.004	0.003
1.874	1.922	1.915	1.911	1.891	1.884	1.790	1.868	1.778
0.530	0.545	0.575	0.596	0.477	0.533	0.422	0.473	0.449
1.345	1.377	1.341	1.315	1.414	1.351	1.369	1.395	1.329
0.177	0.183	0.129	0.108	0.278	0.159	0.333	0.278	0.258
0.146	0.120	0.187	0.240	0.002	0.159	0.007	0.036	0.103
0.006	0.004	0.007	0.007	0.006	0.005	0.011	0.008	0.009
0.343	0.334	0.356	0.348	0.317	0.345	0.295	0.299	0.318
0.004	-	-	0.003	0.003	-	-	0.004	0.003
0.001	-	-	-	0.001	-	0.001	0.003	0.002
-	0.009	0.007	0.005	0.009	-	-	-	-
0.979	0.996	0.992	0.984	0.998	0.974	0.988	0.977	0.954
0.01	-	-	0.01	-	0.02	0.01	0.01	0.04
0.02	0.02	0.02	0.02	0.02	0.02	0.02	0.02	0.02
-	0.01	0.01	0.01	0.01	-	-	-	-
0.47	0.46	0.43	0.41	0.53	0.47	0.58	0.53	0.55
0.50	0.52	0.55	0.57	0.45	0.49	0.39	0.44	0.39

#16	#19	#21	#27	#28	#29	#30	#32	#33
51.11	53.29	50.96	52.83	52.41	53.04	52.84	52.20	52.00
0.05	<i>bdl</i>	<i>bdl</i>	<i>bdl</i>	<i>bdl</i>	0.05	0.07	0.05	<i>bdl</i>
21.33	22.08	22.43	20.71	18.80	20.74	21.36	19.63	18.78
7.73	7.13	8.03	7.36	8.71	6.54	6.53	7.67	8.33
0.20	0.17	0.18	0.08	0.17	0.12	0.17	0.14	0.22
2.88	3.00	2.73	3.15	4.62	3.90	3.91	3.97	3.90
0.21	0.05	0.12	<i>bdl</i>	0.07	<i>bdl</i>	<i>bdl</i>	0.09	0.08
0.09	0.04	0.05	<i>bdl</i>	<i>bdl</i>	<i>bdl</i>	<i>bdl</i>	0.10	<i>bdl</i>
9.54	10.47	9.87	11.16	10.97	11.00	11.02	10.37	10.01
0.11	0.09	0.10	0.08	<i>bdl</i>	0.06	<i>bdl</i>	0.05	0.07
93.24	96.32	94.47	95.37	95.76	95.46	95.89	94.27	93.41
3.528	3.568	3.473	3.607	3.549	3.591	3.554	3.578	3.593
0.003	-	-	-	-	0.002	0.004	0.003	-
1.735	1.743	1.801	1.667	1.500	1.655	1.693	1.586	1.529
0.472	0.432	0.527	0.393	0.451	0.409	0.446	0.422	0.407
1.263	1.311	1.274	1.273	1.049	1.246	1.248	1.164	1.122
0.172	0.231	0.133	0.322	0.094	0.212	0.169	0.163	0.142
0.274	0.168	0.324	0.098	0.399	0.158	0.199	0.277	0.340
0.011	0.010	0.011	0.004	0.010	0.007	0.009	0.008	0.013
0.296	0.300	0.278	0.321	0.467	0.394	0.392	0.405	0.402
0.016	0.003	0.009	-	0.005	-	-	0.007	0.006
0.003	0.002	0.003	0.002	-	0.002	-	0.001	0.002
0.012	0.006	0.007	-	-	-	-	0.014	-
0.840	0.895	0.858	0.972	0.948	0.950	0.946	0.907	0.883
0.13	0.09	0.12	0.02	0.04	0.04	0.05	0.07	0.11
0.02	0.02	0.02	0.02	0.02	0.02	0.02	0.02	0.02
0.01	0.01	0.01	-	-	-	-	0.01	-
0.53	0.57	0.47	0.61	0.55	0.59	0.56	0.58	0.59
0.29	0.31	0.37	0.35	0.39	0.35	0.38	0.31	0.28

#41	#42	#43	#44	#49	#51	#53	#1	#2
54.17	52.84	51.83	52.84	52.16	53.08	52.30	52.41	52.24
<i>bdl</i>	<i>bdl</i>	0.05	<i>bdl</i>	0.08	0.04	<i>bdl</i>	0.04	0.06
21.45	22.11	21.81	21.73	19.41	21.74	22.06	20.90	20.58
6.82	6.16	6.98	6.07	8.80	6.24	7.18	6.76	6.69
0.18	0.10	0.10	0.18	0.15	0.18	0.15	0.12	0.16
3.32	3.30	3.51	3.27	3.54	3.33	3.46	3.81	3.65
0.05	<i>bdl</i>	0.08	<i>bdl</i>	0.37	<i>bdl</i>	<i>bdl</i>	0.05	0.12
<i>bdl</i>	<i>bdl</i>	<i>bdl</i>	<i>bdl</i>	0.10	<i>bdl</i>	<i>bdl</i>	<i>bdl</i>	<i>bdl</i>
11.03	10.40	10.42	11.20	9.75	11.15	10.69	10.93	11.08
0.08	0.11	0.11	0.08	0.05	0.09	0.05	0.04	<i>bdl</i>
97.10	95.02	94.88	95.37	94.41	95.87	95.89	95.07	94.57
3.613	3.571	3.517	3.591	3.574	3.587	3.514	3.565	3.586
-	-	0.003	-	0.004	0.002	-	0.002	0.003
1.686	1.761	1.744	1.741	1.567	1.732	1.747	1.675	1.665
0.387	0.429	0.483	0.409	0.426	0.413	0.486	0.435	0.414
1.299	1.332	1.261	1.332	1.141	1.319	1.261	1.240	1.251
0.283	0.201	0.143	0.288	0.190	0.274	0.146	0.195	0.263
0.097	0.147	0.253	0.057	0.315	0.079	0.258	0.190	0.121
0.010	0.006	0.006	0.010	0.008	0.011	0.008	0.007	0.009
0.330	0.333	0.355	0.331	0.362	0.336	0.346	0.386	0.373
0.004	-	0.006	-	0.027	-	-	0.004	0.009
0.002	0.003	0.003	0.002	0.001	0.002	0.001	0.001	-
-	-	-	-	0.013	-	-	-	-
0.938	0.896	0.902	0.972	0.852	0.962	0.917	0.948	0.971
0.06	0.10	0.09	0.03	0.11	0.03	0.08	0.04	0.01
0.02	0.02	0.02	0.02	0.02	0.02	0.02	0.02	0.02
-	-	-	-	0.01	-	-	-	-
0.61	0.57	0.52	0.59	0.58	0.59	0.51	0.57	0.59
0.31	0.31	0.37	0.37	0.26	0.36	0.39	0.37	0.37

#3	#4	#5	#6	#7	#8	#9	#11	#12
50.86	52.20	51.58	51.02	51.59	51.24	51.07	51.19	51.79
0.04	0.05	0.05	<i>bdl</i>	0.06	0.04	<i>bdl</i>	0.05	<i>bdl</i>
19.96	19.96	20.73	22.37	20.77	21.12	22.10	21.79	20.40
7.16	7.20	7.04	6.64	6.56	7.19	7.10	6.92	7.48
0.16	0.13	0.15	0.10	0.20	0.14	0.09	0.10	0.09
3.91	3.74	3.47	3.53	3.53	3.46	3.50	3.43	3.64
0.15	<i>bdl</i>	0.05	0.12	0.09	0.12	0.07	0.11	0.07
<i>bdl</i>	0.07	<i>bdl</i>	0.07	<i>bdl</i>	<i>bdl</i>	<i>bdl</i>	0.05	<i>bdl</i>
10.99	11.22	11.09	10.24	11.18	10.56	10.55	10.62	10.73
<i>bdl</i>	0.06	<i>bdl</i>	0.06	0.14	0.08	0.11	0.07	0.05
93.23	94.63	94.17	94.16	94.11	93.94	94.59	94.32	94.23
3.545	3.593	3.559	3.479	3.568	3.527	3.479	3.507	3.559
0.002	0.003	0.003	-	0.003	0.002	-	0.002	-
1.640	1.619	1.686	1.797	1.693	1.713	1.775	1.759	1.652
0.455	0.407	0.441	0.521	0.432	0.473	0.521	0.493	0.441
1.185	1.212	1.245	1.276	1.262	1.241	1.254	1.266	1.212
0.199	0.262	0.243	0.096	0.267	0.177	0.113	0.167	0.198
0.218	0.153	0.163	0.283	0.112	0.237	0.292	0.229	0.232
0.009	0.008	0.009	0.006	0.012	0.008	0.005	0.006	0.005
0.406	0.384	0.357	0.359	0.364	0.355	0.355	0.350	0.372
0.011	-	0.003	0.009	0.007	0.009	0.005	0.008	0.005
-	0.002	-	0.002	0.004	0.002	0.003	0.002	0.001
-	0.009	-	0.009	-	-	-	0.007	-
0.977	0.985	0.976	0.891	0.986	0.927	0.917	0.928	0.941
0.01	0.00	0.02	0.09	-	0.06	0.07	0.06	0.05
0.02	0.02	0.02	0.02	0.02	0.02	0.02	0.02	0.02
-	0.01	-	0.01	-	-	-	0.01	-
0.55	0.60	0.56	0.48	0.57	0.53	0.48	0.51	0.56
0.42	0.38	0.40	0.40	0.40	0.39	0.43	0.41	0.37

Transect-3 (Inzecca)								
CO-42								
#14	#15	#16	#17	#18	#19	#21	#22	#23
51.34	50.61	50.99	50.91	50.07	51.51	51.24	51.47	50.94
0.22	0.39	0.25	0.34	0.46	0.11	0.33	0.17	0.12
20.01	20.14	20.15	19.85	19.92	20.74	21.02	20.70	20.30
7.87	7.79	7.24	7.93	8.25	6.20	6.83	7.04	7.08
0.16	0.16	0.15	0.22	0.10	0.11	0.10	0.11	0.18
3.96	3.76	3.72	4.12	3.89	3.70	3.73	4.05	3.68
<i>bdl</i>	<i>bdl</i>	0.06	<i>bdl</i>	0.05	0.13	0.27	0.07	<i>bdl</i>
0.07	0.08	0.07	0.07	0.09	0.06	0.06	0.06	<i>bdl</i>
11.20	11.02	10.91	10.95	10.88	10.89	10.70	10.99	11.27
<i>bdl</i>	<i>bdl</i>	<i>bdl</i>	0.05	0.05	0.08	0.08	<i>bdl</i>	0.07
94.84	93.94	93.54	94.44	93.74	93.51	94.35	94.65	93.63
3.524	3.506	3.543	3.502	3.478	3.571	3.521	3.521	3.545
0.012	0.020	0.013	0.018	0.024	0.005	0.017	0.008	0.006
1.618	1.645	1.650	1.609	1.631	1.695	1.702	1.669	1.665
0.476	0.494	0.457	0.498	0.522	0.429	0.479	0.479	0.455
1.142	1.151	1.192	1.111	1.108	1.267	1.223	1.189	1.210
0.178	0.179	0.208	0.118	0.140	0.242	0.199	0.147	0.231
0.274	0.273	0.213	0.338	0.339	0.117	0.193	0.256	0.180
0.009	0.010	0.009	0.013	0.006	0.006	0.006	0.006	0.011
0.405	0.388	0.385	0.423	0.403	0.382	0.382	0.413	0.382
-	-	0.005	-	0.003	0.009	0.020	0.005	-
-	-	-	0.001	0.001	0.002	0.002	-	0.002
0.010	0.011	0.009	0.009	0.012	0.008	0.008	0.008	-
0.980	0.974	0.967	0.961	0.965	0.963	0.938	0.959	1.000
0.01	0.01	0.02	0.03	0.02	0.02	0.03	0.03	-
0.02	0.02	0.02	0.02	0.02	0.02	0.02	0.02	0.02
0.01	0.01	0.01	0.01	0.01	0.01	0.01	0.01	-
0.54	0.53	0.56	0.52	0.50	0.58	0.54	0.53	0.55
0.44	0.44	0.40	0.43	0.45	0.38	0.39	0.42	0.43

#24	#25	#26	#27	#28	#29	#31	#32	#33
52.10	51.06	51.96	51.65	50.67	51.47	50.60	50.60	50.69
0.34	0.30	0.20	0.19	1.34	0.14	0.33	0.36	0.30
20.07	20.51	19.97	20.71	20.28	19.17	18.74	18.54	18.70
6.89	7.35	7.04	6.84	7.69	7.96	8.83	8.41	8.74
0.21	0.11	0.14	0.23	0.16	0.09	0.19	0.11	0.12
3.59	3.74	3.87	3.82	3.37	4.08	4.20	4.29	4.15
0.17	0.08	<i>bdl</i>	0.05	0.32	<i>bdl</i>	<i>bdl</i>	<i>bdl</i>	<i>bdl</i>
<i>bdl</i>	<i>bdl</i>	0.10	<i>bdl</i>	<i>bdl</i>	<i>bdl</i>	<i>bdl</i>	<i>bdl</i>	<i>bdl</i>
11.06	11.08	11.01	11.10	10.88	11.04	10.95	11.07	10.97
0.08	0.07	<i>bdl</i>	0.06	0.13	0.09	0.06	0.04	0.06
94.50	94.30	94.29	94.65	94.83	94.04	93.90	93.41	93.73
3.593	3.522	3.578	3.541	3.500	3.562	3.512	3.532	3.526
0.017	0.016	0.010	0.010	0.069	0.007	0.017	0.019	0.015
1.631	1.668	1.621	1.673	1.651	1.563	1.533	1.525	1.533
0.407	0.478	0.422	0.459	0.500	0.438	0.488	0.468	0.474
1.224	1.189	1.199	1.215	1.150	1.126	1.045	1.058	1.059
0.293	0.198	0.224	0.193	0.290	0.189	0.122	0.154	0.148
0.105	0.226	0.181	0.199	0.154	0.272	0.390	0.336	0.360
0.012	0.006	0.008	0.013	0.009	0.005	0.011	0.007	0.007
0.369	0.385	0.398	0.390	0.347	0.421	0.435	0.446	0.430
0.012	0.006	-	0.003	0.024	-	-	-	-
0.002	0.002	-	0.002	0.004	0.002	0.002	0.001	0.002
-	-	0.013	-	-	-	-	-	-
0.973	0.975	0.967	0.971	0.958	0.975	0.969	0.986	0.973
0.01	0.02	0.02	0.02	0.01	0.02	0.02	0.01	0.02
0.02	0.02	0.02	0.02	0.02	0.02	0.02	0.02	0.02
-	-	0.01	-	-	-	-	-	-
0.61	0.54	0.59	0.55	0.57	0.57	0.53	0.55	0.54
0.35	0.43	0.37	0.41	0.38	0.40	0.43	0.42	0.42

#34	#35	#36	#37	#38	#39	#40	#41	#42
51.01	52.01	51.27	51.67	51.63	51.87	51.64	51.10	51.25
0.26	0.08	0.13	0.10	0.12	0.11	0.08	0.16	0.16
20.97	20.34	19.97	20.72	20.60	21.02	20.52	20.87	21.05
6.86	6.39	8.03	6.47	6.41	6.35	6.65	6.70	6.40
0.06	0.12	0.08	0.15	0.12	0.14	0.14	0.16	0.07
3.96	3.77	3.86	4.04	4.02	3.80	3.89	3.94	4.04
<i>bdl</i>	0.05	0.05	<i>bdl</i>	<i>bdl</i>	<i>bdl</i>	<i>bdl</i>	<i>bdl</i>	<i>bdl</i>
<i>bdl</i>	<i>bdl</i>	<i>bdl</i>	0.05	0.07	<i>bdl</i>	0.07	0.07	0.05
10.86	11.29	11.01	11.00	11.25	11.27	10.63	10.95	10.85
0.05	0.08	0.06	<i>bdl</i>	0.05	<i>bdl</i>	0.07	<i>bdl</i>	<i>bdl</i>
94.03	94.13	94.46	94.19	94.29	94.56	93.68	93.95	93.86
3.505	3.594	3.530	3.546	3.554	3.556	3.559	3.518	3.522
0.013	0.004	0.007	0.005	0.006	0.006	0.004	0.008	0.008
1.698	1.657	1.620	1.676	1.671	1.698	1.666	1.694	1.705
0.495	0.406	0.470	0.454	0.446	0.444	0.441	0.482	0.478
1.204	1.251	1.150	1.222	1.225	1.254	1.225	1.213	1.227
0.134	0.273	0.180	0.162	0.201	0.219	0.167	0.149	0.138
0.260	0.097	0.282	0.209	0.168	0.145	0.216	0.237	0.230
0.004	0.007	0.005	0.009	0.007	0.008	0.008	0.009	0.004
0.405	0.388	0.396	0.413	0.413	0.388	0.399	0.404	0.413
-	0.004	0.004	-	-	-	-	-	-
0.001	0.002	0.002	-	0.001	-	0.002	-	-
-	-	-	0.007	0.009	-	0.010	0.010	0.007
0.952	0.995	0.967	0.963	0.988	0.985	0.935	0.961	0.951
0.04	-	0.02	0.03	0.00	0.01	0.05	0.03	0.04
0.02	0.02	0.02	0.02	0.02	0.02	0.02	0.02	0.02
-	-	-	0.01	0.01	-	0.01	0.01	0.01
0.52	0.60	0.54	0.55	0.56	0.56	0.56	0.53	0.53
0.42	0.38	0.42	0.40	0.42	0.41	0.36	0.42	0.41

#43	#44	#45	#46	#49	#50	#51	#53	#54
51.88	51.90	51.52	52.28	51.37	50.96	51.58	51.82	51.90
0.06	0.08	0.05	<i>bdl</i>	<i>bdl</i>	<i>bdl</i>	<i>bdl</i>	0.07	0.05
20.65	20.73	21.68	20.41	21.65	21.44	21.18	21.48	20.58
6.67	6.39	6.34	6.58	6.60	6.41	6.46	6.75	6.64
0.20	0.14	0.15	0.18	0.13	0.13	0.18	0.14	0.16
3.45	3.67	3.44	3.67	3.47	3.39	3.60	3.29	3.63
0.12	0.06	0.10	0.16	0.11	0.14	0.14	0.09	0.07
0.05	0.06	0.07	0.07	0.05	0.05	0.09	<i>bdl</i>	<i>bdl</i>
10.81	11.18	9.67	10.55	10.35	10.51	10.59	10.34	10.38
0.07	0.06	0.06	<i>bdl</i>	0.05	0.04	0.05	0.07	<i>bdl</i>
93.94	94.28	93.08	93.90	93.78	93.07	93.86	94.06	93.40
3.584	3.578	3.538	3.598	3.526	3.535	3.550	3.551	3.579
0.003	0.004	0.003	-	-	-	-	0.004	0.002
1.681	1.684	1.755	1.656	1.751	1.753	1.718	1.735	1.673
0.416	0.422	0.462	0.402	0.474	0.465	0.450	0.449	0.421
1.265	1.262	1.293	1.254	1.277	1.289	1.268	1.285	1.252
0.260	0.260	0.115	0.234	0.157	0.199	0.197	0.196	0.186
0.125	0.108	0.249	0.144	0.222	0.173	0.175	0.190	0.197
0.011	0.008	0.008	0.010	0.007	0.007	0.010	0.008	0.009
0.356	0.377	0.352	0.376	0.355	0.351	0.369	0.336	0.373
0.009	0.004	0.008	0.012	0.008	0.010	0.010	0.007	0.005
0.002	0.002	0.002	-	0.001	0.001	0.001	0.002	-
0.007	0.008	0.009	0.010	0.007	0.007	0.012	-	-
0.952	0.983	0.847	0.926	0.906	0.930	0.929	0.904	0.913
0.03	-	0.13	0.05	0.08	0.05	0.05	0.08	0.08
0.02	0.02	0.02	0.02	0.02	0.02	0.02	0.02	0.02
0.01	0.01	0.01	0.01	0.01	0.01	0.01	-	-
0.59	0.58	0.54	0.60	0.53	0.54	0.55	0.55	0.58
0.36	0.39	0.29	0.32	0.37	0.38	0.37	0.34	0.32

---

---

---

---

**#55            #56**

---

52.42	51.85
<i>bdl</i>	0.07
20.13	20.68
6.89	7.02
0.19	<i>bdl</i>
3.79	3.47
0.10	0.23
0.05	0.05
10.44	9.79
0.05	0.05
94.07	93.19

3.597	3.574
-	0.003
1.628	1.680
0.403	0.426
1.225	1.253
0.197	0.182
0.198	0.222
0.011	-
0.388	0.356
0.008	0.017
0.001	0.001
0.006	0.007
0.914	0.860

0.07	0.11
0.02	0.02
0.01	0.01
0.60	0.58
<u>0.30</u>	<u>0.27</u>

## Representative EMPA and chemical formulas of Feldspar

Locality	Sample					Transect 1 (Casti	
		CO-24		CO-25			
Type	Igneous	Metamorphic	Igneous	Metamorphic	#1	Igne	
Analysis	#13	#14	#14	#26	#1	#37	
SiO <sub>2</sub> (wt%)	64.34	69.70	62.07	67.34	64.45	64.16	
Al <sub>2</sub> O <sub>3</sub>	18.56	19.94	18.85	19.53	18.36	18.63	
FeOt	bdl	0.06	0.83	bdl	0.08	0.47	
CaO	bdl	0.28	bdl	0.05	bdl	0.09	
Na <sub>2</sub> O	0.12	10.84	0.51	11.73	0.20	0.19	
K <sub>2</sub> O	16.83	0.31	15.94	0.09	17.11	17.06	
BaO	0.47	bdl	0.36	bdl	0.04	0.10	
Total	100.31	101.13	98.56	98.74	100.25	100.70	
<i>Fe<sub>2</sub>O<sub>3</sub></i>	0.00	0.07	0.93	-	0.09	0.53	
<i>Formula (8 Oxygens)</i>							
Si (apfu)	2.983	3.002	2.923	2.981	2.986	2.963	
Al	1.014	1.012	1.046	1.019	1.003	1.014	
Fe <sup>3+</sup>	-	0.002	0.033	-	0.003	0.018	
Ba	0.008	-	0.007	-	0.001	0.002	
Ca	-	0.013	-	0.002	-	0.004	
Na	0.012	0.905	0.046	1.007	0.018	0.017	
K	0.996	0.017	0.957	0.005	1.011	1.005	
XAn	-	0.01	0.01	0.00	-	0.01	
XAb	0.02	0.97	0.05	0.99	0.02	0.02	
XOr	0.98	0.02	0.95	0.00	0.98	0.98	

\* FeOt total iron reported as FeO; apfu: atoms per formula unit; bdl: below detection limit.

\*\* TiO<sub>2</sub>, MnO and MgO always below detection limit.

irla)						Transer	
		CO-38				CO-35	
ous		Metamorphic				Metamorphic	
#42	#14	#2	#43	#1	#2	#94	#97
64.27	64.56	68.35	67.04	70.68	67.84	68.31	67.86
18.69	18.24	19.79	20.09	20.24	19.86	19.66	19.89
0.05	0.14	0.15	0.10	0.27	0.22	0.16	0.10
<i>bdl</i>	<i>bdl</i>	0.07	0.62	0.66	0.41	<i>bdl</i>	0.44
0.34	0.27	11.78	10.88	8.68	11.84	11.88	11.61
17.12	16.86	0.08	0.30	1.24	0.15	0.14	0.12
<i>bdl</i>	<i>bdl</i>	<i>bdl</i>	<i>bdl</i>	<i>bdl</i>	<i>bdl</i>	<i>bdl</i>	<i>bdl</i>
100.47	100.08	100.22	99.02	101.76	100.31	100.15	100.02
0.05	0.16	0.17	0.11	0.30	0.24	0.17	0.11
2.974	2.993	2.981	2.961	3.016	2.964	2.983	2.969
1.019	0.997	1.017	1.046	1.018	1.023	1.012	1.026
0.002	0.006	0.005	0.004	0.010	0.008	0.006	0.004
-	-	-	-	-	-	0.000	0.000
-	-	0.003	0.029	0.030	0.019	-	0.021
0.031	0.024	0.996	0.932	0.718	1.003	1.006	0.985
1.010	0.997	0.005	0.017	0.067	0.008	0.008	0.007
-	-	0.00	0.03	0.04	0.02	-	0.02
0.03	0.02	0.99	0.95	0.88	0.97	0.99	0.97
0.97	0.98	0.00	0.02	0.08	0.01	0.01	0.01

ct-2 (Vivario-Venaco)			transect-3 (Inzecca)				
CO-36			CO-42				
Igneous		Metamorphic	Igneous				M
#1	#27	#23	#25	#37	#47	#9	#26
64.71	65.18	69.23	64.01	63.87	63.70	64.25	69.35
18.34	18.21	19.28	18.11	18.46	18.30	18.30	19.56
<i>bdl</i>	0.08	0.05	0.51	0.54	0.08	<i>bdl</i>	0.11
<i>bdl</i>	<i>bdl</i>	<i>bdl</i>	<i>bdl</i>	<i>bdl</i>	<i>bdl</i>	<i>bdl</i>	<i>bdl</i>
<i>bdl</i>	0.25	11.31	0.20	0.32	0.14	0.21	11.98
16.23	17.08	0.09	17.15	16.91	17.05	16.79	0.08
0.21	0.11	<i>bdl</i>	<i>bdl</i>	0.24	0.15	0.12	<i>bdl</i>
99.48	100.91	99.97	99.99	100.34	99.41	99.67	101.07
-	0.09	0.05	0.57	0.60	0.09	-	0.12
3.003	2.999	3.016	2.980	2.966	2.981	2.991	2.997
1.003	0.987	0.990	0.994	1.011	1.009	1.004	0.996
-	0.003	0.002	0.020	0.021	0.003	-	0.004
0.004	0.002	0.000	-	0.004	0.003	0.002	-
-	-	-	-	-	-	-	-
-	0.022	0.956	0.018	0.029	0.012	0.019	1.004
0.964	1.003	0.005	1.019	1.002	1.018	0.997	0.004
-	-	-	-	-	-	-	-
-	0.02	0.99	0.02	0.03	0.01	0.02	1.00
1.00	0.98	0.01	0.98	0.97	0.99	0.98	-

<hr/> <hr/>	
Metamorphic	
#3	#10
70.09	69.87
19.50	19.06
0.18	<i>bdl</i>
<i>bdl</i>	<i>bdl</i>
11.47	10.98
<i>bdl</i>	0.05
<i>bdl</i>	<i>bdl</i>
101.24	99.96
0.20	-
3.014	3.034
0.988	0.975
0.006	-
-	-
-	-
0.957	0.925
-	0.003
-	-
1.00	1.00
-	-

## Representative EMPA and chemical formulas of Stilpnomela

Locality						Tra
Sample	CO-24	CO-25				
Analysis	#36	#37	#14	#15	#16	#17
SiO <sub>2</sub> (wt%)	43.93	43.99	44.54	46.28	43.98	42.84
TiO <sub>2</sub>	bdl	bdl	0.24	0.19	0.12	0.15
Al <sub>2</sub> O <sub>3</sub>	5.85	6.08	5.87	5.75	6.42	7.09
FeOt	34.19	33.90	29.96	29.52	29.52	29.61
MnO	0.45	0.41	2.19	2.24	2.17	2.12
MgO	2.07	1.91	3.25	3.16	3.46	3.51
CaO	0.10	0.13	0.23	0.22	0.12	0.20
Na <sub>2</sub> O	0.21	0.37	0.53	0.52	0.48	0.49
K <sub>2</sub> O	2.04	2.19	1.98	1.84	2.44	2.96
Total	88.83	88.98	88.79	89.72	88.71	88.98
FeO	22.45	22.07	17.81	17.22	17.54	17.63
Fe <sub>2</sub> O <sub>3</sub>	13.05	13.16	13.50	13.66	13.32	13.31
<i>Formula (120 Cations)</i>						
Si (apfu)	63.60	63.83	64.09	65.73	63.34	61.86
Al <sup>[IV]</sup>	8.40	8.17	7.91	6.27	8.66	10.14
Ti	-	-	0.26	0.20	0.13	0.17
Al <sup>[VI]</sup>	1.58	2.23	2.05	3.36	2.24	1.92
Fe <sup>2+</sup>	27.18	26.78	21.43	20.46	21.12	21.29
Fe <sup>3+</sup>	14.22	14.36	14.62	14.60	14.43	14.47
Mn	0.55	0.50	2.67	2.70	2.64	2.59
Mg	4.46	4.13	6.97	6.68	7.43	7.56
Ca	0.15	0.20	0.35	0.33	0.19	0.32
Na	0.58	1.03	1.47	1.44	1.34	1.37
K	3.77	4.06	3.64	3.34	4.47	5.46
(OH)	32.19	31.41	31.08	29.84	31.20	31.44

\* FeOt total iron reported as FeO; apfu: atoms per formula unit; bdl: below detection lim

\*\*(OH) by stoichiometry

**ine****ansect-1 (Castirla)**

CO-38								
#18	#19	#23	#24	#25	#5	#6	#7	#19
44.44	43.80	47.20	43.59	42.78	45.47	45.47	44.29	47.62
0.13	<i>bdl</i>	0.17	0.12	<i>bdl</i>	<i>bdl</i>	<i>bdl</i>	<i>bdl</i>	<i>bdl</i>
6.46	6.23	5.69	6.52	6.46	5.86	5.51	5.46	6.44
30.77	29.92	29.16	30.85	31.09	29.68	29.86	27.89	27.58
2.02	2.00	2.05	2.00	2.21	1.86	2.20	3.41	3.21
3.57	3.90	2.91	3.85	3.40	3.60	3.54	4.41	4.40
0.23	0.23	1.00	0.44	0.11	0.23	0.26	0.20	0.19
0.48	0.57	0.61	0.59	0.50	0.62	0.36	0.34	0.12
2.34	1.95	2.02	1.92	1.86	1.62	1.33	1.53	0.64
90.45	88.61	90.82	89.88	88.40	88.94	88.52	87.51	90.19
18.50	17.87	16.01	18.63	19.41	17.52	17.86	15.93	16.06
13.63	13.39	14.62	13.59	12.98	13.51	13.33	13.28	12.80
62.80	62.80	67.03	61.83	61.60	64.83	64.90	63.64	65.27
9.20	9.20	4.97	10.17	10.40	7.17	7.10	8.36	6.73
0.14	-	0.18	0.12	-	-	-	-	-
1.55	1.33	4.55	0.73	0.57	2.68	2.17	0.88	3.67
21.87	21.43	19.01	22.09	23.37	20.89	21.32	19.15	18.41
14.50	14.45	15.63	14.51	14.06	14.50	14.32	14.36	13.21
2.42	2.43	2.46	2.41	2.69	2.25	2.65	4.15	3.72
7.53	8.33	6.16	8.14	7.30	7.66	7.53	9.44	8.99
0.35	0.35	1.52	0.67	0.17	0.35	0.39	0.30	0.28
1.33	1.59	1.69	1.61	1.40	1.70	1.01	0.93	0.31
4.22	3.56	3.66	3.48	3.41	2.95	2.42	2.80	1.12
31.81	32.19	27.64	32.64	33.36	30.80	31.51	32.74	31.12

nit.

Transect-2 (Vivario-Venaco)								
CO-36								
#20	#21	#22	#24	#25	#26	#34	#35	#13
47.03	48.56	46.55	47.14	46.90	46.75	49.04	47.33	48.76
<i>bdl</i>	<i>bdl</i>	<i>bdl</i>	<i>bdl</i>	<i>bdl</i>	<i>bdl</i>	<i>bdl</i>	<i>bdl</i>	0.07
5.98	6.92	5.74	5.94	5.93	5.95	5.97	5.87	7.83
28.00	25.84	28.89	28.50	28.38	28.15	28.37	28.61	24.25
3.58	3.32	3.55	3.82	3.86	3.64	3.55	3.20	1.02
4.54	4.29	4.49	4.46	4.40	4.17	4.07	4.43	4.88
0.29	0.16	0.20	0.23	0.21	0.32	0.17	0.29	0.31
0.08	0.87	0.09	0.09	0.10	0.10	0.08	0.20	0.19
0.91	1.17	0.94	0.87	0.96	0.70	0.88	1.04	2.35
90.41	91.12	90.45	91.05	90.73	89.77	92.12	90.97	89.65
16.12	13.73	16.96	16.57	16.47	16.44	16.35	16.49	12.52
13.21	13.45	13.26	13.26	13.23	13.02	13.36	13.47	13.03
64.66	66.58	64.08	64.38	64.36	64.77	66.21	64.90	67.68
7.34	5.42	7.92	7.62	7.64	7.23	5.79	7.10	4.32
-	-	-	-	-	-	-	-	0.07
2.34	5.76	1.38	1.94	1.95	2.49	3.71	2.38	8.49
18.53	15.75	19.52	18.93	18.90	19.05	18.46	18.91	14.54
13.66	13.88	13.73	13.63	13.66	13.58	13.57	13.90	13.61
4.17	3.85	4.14	4.42	4.48	4.27	4.05	3.72	1.20
9.30	8.76	9.22	9.08	9.00	8.62	8.20	9.05	10.09
0.43	0.23	0.29	0.34	0.30	0.47	0.25	0.42	0.46
0.21	2.32	0.25	0.24	0.26	0.26	0.21	0.52	0.50
1.60	2.04	1.66	1.51	1.68	1.24	1.51	1.82	4.16
32.00	28.36	32.88	32.42	32.39	31.93	30.71	31.68	25.83

Transect-3 (Inzecca)								
CO-42								
#58	#59	#14	#20	#23	#24	#34	#35	#36
45.59	47.37	46.29	44.86	45.93	44.78	47.28	46.22	45.97
0.06	<i>bdl</i>	<i>bdl</i>	0.07	0.04	0.14	<i>bdl</i>	<i>bdl</i>	<i>bdl</i>
6.63	7.80	5.90	10.87	7.88	8.16	6.51	6.51	6.24
26.25	26.58	30.83	25.67	28.18	31.67	30.15	30.61	31.50
1.48	1.38	1.19	0.98	1.45	0.89	1.02	0.88	1.07
4.84	5.75	4.13	4.11	5.10	3.89	4.97	5.08	4.93
0.34	0.15	0.15	0.42	0.30	0.66	0.35	0.41	0.32
0.22	<i>bdl</i>	0.08	0.22	0.19	0.33	0.16	0.19	0.26
0.71	1.15	0.98	3.06	1.36	0.43	0.47	0.55	0.66
86.10	90.17	89.55	90.27	90.45	90.96	90.93	90.46	90.95
15.16	15.38	19.16	14.91	16.78	20.46	18.41	18.83	19.54
12.32	12.44	12.97	11.96	12.67	12.46	13.05	13.09	13.28
65.23	64.19	64.42	62.49	62.88	61.38	64.14	63.16	62.74
6.77	7.81	7.58	9.51	9.12	10.62	7.86	8.84	9.26
0.06	-	-	0.08	0.04	0.15	-	-	-
4.41	4.65	2.10	8.32	3.60	2.56	2.56	1.64	0.77
18.14	17.43	22.31	17.37	19.21	23.45	20.88	21.52	22.31
13.27	12.69	13.58	12.53	13.05	12.85	13.32	13.47	13.64
1.79	1.59	1.41	1.16	1.68	1.04	1.17	1.02	1.24
10.33	11.62	8.58	8.54	10.42	7.95	10.06	10.35	10.04
0.52	0.21	0.22	0.62	0.44	0.97	0.51	0.61	0.47
0.62	-	0.20	0.61	0.51	0.88	0.43	0.50	0.68
1.29	1.99	1.73	5.45	2.38	0.76	0.82	0.96	1.16
30.26	30.64	32.29	27.07	31.31	32.44	32.12	32.89	33.59

#45	#46	#54
45.80	45.37	46.41
0.08	0.04	<i>bdl</i>
6.20	6.13	6.72
29.66	29.89	29.53
1.01	1.69	1.01
5.02	5.41	4.83
0.30	0.19	0.28
0.10	0.05	0.38
0.54	0.47	1.19
88.71	89.25	90.33
18.15	18.40	17.62
12.79	12.77	13.23
63.68	62.50	63.96
8.32	9.50	8.04
0.09	0.05	-
1.84	0.45	2.87
21.10	21.20	20.31
13.38	13.23	13.72
1.19	1.97	1.17
10.40	11.11	9.92
0.44	0.29	0.42
0.27	0.13	1.01
0.96	0.83	2.08
32.69	34.27	31.40

## Representative EMPA and chemical formulas of Biotite

Locality Sample Analysis	Transect1 (Castirla)			
	#26	#27	CO-38 #39	#41
SiO <sub>2</sub> (wt%)	39.03	39.56	35.99	37.17
TiO <sub>2</sub>	0.55	0.58	0.68	0.92
Al <sub>2</sub> O <sub>3</sub>	17.86	18.93	16.88	17.18
FeOt	22.50	21.56	26.69	24.42
MnO	0.30	0.30	0.47	0.40
MgO	4.01	3.90	5.08	4.37
CaO	bdl	bdl	bdl	bdl
Na <sub>2</sub> O	bdl	0.04	0.06	bdl
K <sub>2</sub> O	10.44	10.49	8.29	10.05
Total	94.71	95.37	94.15	94.51
<i>Formula (11 Oxygens; Fe<sub>total</sub> = Fe<sup>2+</sup>)</i>				
Si (apfu)	3.019	3.015	2.858	2.925
Al <sup>[IV]</sup>	0.981	0.985	1.142	1.075
Ti	0.032	0.033	0.041	0.055
Al <sup>[VI]</sup>	0.647	0.715	0.438	0.518
Fe <sup>2+</sup>	1.455	1.374	1.772	1.607
Mn	0.020	0.019	0.031	0.027
Mg	0.463	0.443	0.602	0.512
Ca	-	-	-	-
Na	-	0.007	0.009	-
K	1.030	1.020	0.840	1.009
<sup>(a)</sup> XMg	0.24	0.24	0.25	0.24

\* FeOt total iron reported as FeO; apfu: atoms per formula unit; bdl: below detection limit.

(a) XMg as [Mg/(Mg+Fe<sup>2+</sup>)]



## Representative EMPA and chemical formulas of Chlorite

Locality Sample Analysis	Transect1 (Castirla)					
	CO-25					
	#7	#8	#10	#12	#14	#20
SiO <sub>2</sub> (wt%)	25.04	24.57	24.61	24.86	25.52	24.61
TiO <sub>2</sub>	<i>bdl</i>	<i>bdl</i>	0.04	0.05	0.05	<i>bdl</i>
Al <sub>2</sub> O <sub>3</sub>	18.33	18.60	18.57	17.63	17.63	17.96
FeOt	35.45	35.49	36.57	36.52	35.31	36.68
MnO	1.22	1.15	1.08	1.00	1.01	1.16
MgO	7.74	7.26	7.44	7.34	7.39	6.74
CaO	<i>bdl</i>	0.06	0.04	0.34	0.45	<i>bdl</i>
Na <sub>2</sub> O	<i>bdl</i>	<i>bdl</i>	<i>bdl</i>	<i>bdl</i>	<i>bdl</i>	<i>bdl</i>
K <sub>2</sub> O	<i>bdl</i>	<i>bdl</i>	<i>bdl</i>	<i>bdl</i>	0.07	<i>bdl</i>
Total	87.77	87.13	88.34	87.74	87.42	87.15
<i>Formula (14 Oxygens)</i>						
Si (apfu)	2.818	2.793	2.762	2.825	2.909	2.812
Al <sup>[IV]</sup>	1.182	1.207	1.238	1.175	1.091	1.188
Ti	-	-	0.003	0.005	0.004	-
Al <sup>[VI]</sup>	1.249	1.285	1.218	1.185	1.277	1.232
Fe <sup>2+</sup>	3.336	3.373	3.418	3.471	3.366	3.506
Fe <sup>3+</sup>	-	-	0.014	-	-	-
Mn	0.116	0.111	0.103	0.096	0.097	0.112
Mg	1.298	1.230	1.245	1.243	1.255	1.148
( <sup>a</sup> ) XMg	0.27	0.26	0.26	0.26	0.27	0.24

\* FeOt total iron reported as FeO; apfu: atoms per formula unit; bdl: below detection limit

(a) XMg as [Mg / (Mg + Fe<sup>2+</sup>)].

		CO-38
#23	#32	#22
24.55	24.85	24.12
0.10	0.17	0.10
18.59	17.39	16.41
36.82	36.89	39.94
0.90	0.78	1.29
6.81	6.43	5.82
0.15	0.35	0.85
<i>bdl</i>	<i>bdl</i>	<i>bdl</i>
<i>bdl</i>	0.18	<i>bdl</i>
87.91	87.04	88.53
2.782	2.871	2.782
1.218	1.129	1.218
0.008	0.015	0.009
1.265	1.238	1.012
3.490	3.564	3.664
-	-	0.189
0.086	0.076	0.126
1.151	1.107	1.000
0.24	0.23	0.20
nit.		

## Representative EMPA and chemical formulas of Epidote

Locality Sample Analysis	Transect-1					
	CO-25		CO-38			
	#2	#36	#71	#72	#73	#74
SiO <sub>2</sub> (wt%)	36.34	37.33	36.65	36.19	36.47	36.50
TiO <sub>2</sub>	bdl	0.10	0.04	bdl	bdl	0.04
Al <sub>2</sub> O <sub>3</sub>	20.34	20.93	21.76	18.63	19.59	19.03
FeOt	15.13	15.32	13.12	17.19	16.05	16.84
MnO	0.35	0.29	0.64	0.18	0.16	0.23
MgO	bdl	bdl	bdl	bdl	bdl	0.07
CaO	22.55	21.54	22.65	22.78	23.02	23.00
Total	94.72	95.52	94.86	94.97	95.29	95.71
<i>Fe<sub>2</sub>O<sub>3</sub></i>	16.82	17.04	14.59	19.11	17.83	18.72
<i>Mn<sub>2</sub>O<sub>3</sub></i>	0.39	0.33	0.71	0.20	0.18	0.25
<i>Formula (12.5 Oxygens)</i>						
Si (apfu)	2.983	3.021	2.987	2.984	2.988	2.985
Ti	-	0.006	0.003	-	-	0.003
Al <sup>Tot</sup>	1.968	1.996	2.090	1.810	1.891	1.834
Fe <sup>3+</sup>	1.039	1.037	0.894	1.185	1.099	1.152
Mn <sup>3+</sup>	0.025	0.020	0.044	0.013	0.011	0.016
Mg	-	-	-	-	-	0.008
Ca	1.984	1.867	1.978	2.012	2.020	2.015
<sup>(a)</sup> XPs	0.35	0.34	0.30	0.40	0.37	0.39

\* FeOt total iron reported as FeO; apfu: atoms per formula unit; bdl: below detection limit.

\*\* Na<sub>2</sub>O and K<sub>2</sub>O always below detection limit.

(a) XPs: Pistacite as [Fe<sup>3+</sup> / (Fe<sup>3+</sup> + Al<sup>3+</sup>)] atomic ratio.

Transect-2 (Vivario-Venaco)								
CO-35						CO-36		
#98	#6	#7	#11	#12	#17	#2	#15	#21
36.78	36.59	36.34	37.93	36.47	36.93	37.39	37.19	37.22
<i>bdl</i>	0.07	0.08	0.04	0.05	<i>bdl</i>	0.18	0.11	0.12
20.71	20.65	19.51	21.32	20.99	21.86	21.65	21.85	21.72
14.36	14.53	16.22	14.67	14.82	13.50	13.95	13.49	14.15
0.28	0.31	0.50	0.21	0.16	0.22	0.20	0.06	0.09
<i>bdl</i>	<i>bdl</i>	<i>bdl</i>	<i>bdl</i>	<i>bdl</i>	<i>bdl</i>	<i>bdl</i>	<i>bdl</i>	<i>bdl</i>
22.61	22.69	22.62	22.75	22.96	23.19	23.18	23.16	23.47
94.75	94.83	95.27	96.92	95.45	95.69	96.55	95.87	96.77
15.99	16.15	18.03	16.30	16.47	15.01	15.53	15.01	15.73
0.31	0.34	0.55	0.23	0.18	0.24	0.22	0.07	0.10
3.009	2.993	2.978	3.025	2.968	2.987	2.996	2.999	2.981
-	0.004	0.005	0.003	0.003	-	0.011	0.007	0.007
1.997	1.991	1.885	2.005	2.013	2.083	2.045	2.077	2.050
0.983	0.994	1.112	0.978	1.009	0.913	0.935	0.910	0.947
0.019	0.021	0.035	0.014	0.011	0.015	0.013	0.004	0.006
-	-	-	-	-	-	-	-	-
1.982	1.989	1.986	1.944	2.003	2.009	1.991	2.001	2.016
0.33	0.33	0.37	0.33	0.33	0.30	0.31	0.30	0.32

		Transect-3 (Inzecca)	
		CO-42	
#31	#32	#105	#106
37.18	37.29	37.42	38.53
0.16	0.26	<i>bdl</i>	0.18
23.49	23.66	26.00	28.22
11.01	11.45	8.45	6.41
0.37	0.25	0.26	0.06
<i>bdl</i>	<i>bdl</i>	<i>bdl</i>	<i>bdl</i>
21.18	22.20	23.67	24.14
93.39	95.11	95.81	97.55
12.26	12.74	9.40	7.13
0.42	0.28	0.29	0.07
3.035	3.002	2.976	2.987
0.010	0.016	-	0.010
2.260	2.245	2.437	2.578
0.752	0.771	0.562	0.415
0.026	0.017	0.018	0.004
-	-	-	-
1.852	1.915	2.017	2.005
0.25	0.26	0.19	0.14

## Representative EMPA and chemical formulas of Garnet

Locality Sample Analysis	#56	#57	#60	#62	#63	#77
SiO <sub>2</sub> (wt%)	33.96	33.70	34.32	34.76	34.13	33.65
TiO <sub>2</sub>	0.24	0.08	1.12	0.19	0.18	0.17
Al <sub>2</sub> O <sub>3</sub>	5.61	5.13	6.89	8.85	6.49	6.23
FeOt	20.22	20.94	17.64	17.02	18.71	19.52
MnO	0.43	0.40	1.39	2.54	0.68	0.66
MgO	0.05	0.05	bdl	0.05	bdl	0.10
CaO	34.49	34.35	33.02	32.59	33.86	32.93
Total	94.99	94.65	94.36	95.99	94.06	93.25
<i>Fe<sub>2</sub>O<sub>3</sub></i>	22.47	23.27	19.01	18.69	20.79	21.68
<i>FeO</i>	-	-	0.54	0.20	-	0.01
<i>H<sub>2</sub>O</i>	1.62	1.68	1.11	1.45	1.22	1.33
<i>Formula (8 Cations)</i>						
Si (apfu)	2.779	2.770	2.847	2.805	2.831	2.814
H /4	0.221	0.230	0.153	0.195	0.169	0.186
Ti	0.015	0.005	0.070	0.012	0.011	0.011
Al <sup>Tot</sup>	0.541	0.497	0.674	0.842	0.634	0.614
Fe <sup>3+</sup>	1.384	1.439	1.187	1.135	1.298	1.365
Fe <sup>2+</sup>	-	-	0.037	0.014	-	0.001
Mn <sup>3+</sup>	0.030	0.028	0.098	0.174	0.048	0.047
Mg	0.006	0.006	-	0.006	-	0.013
Ca	3.024	3.025	2.935	2.818	3.009	2.951
<sup>(a)</sup> Grs	0.275	0.247	0.341	0.365	0.317	0.294
<sup>(a)</sup> Hgr	0.074	0.077	0.051	0.065	0.056	0.062
<sup>(a)</sup> Adr	0.713	0.742	0.615	0.571	0.668	0.686
<sup>(a)</sup> Alm	-	-	0.012	0.005	-	-
<sup>(a)</sup> Prp	0.002	0.002	-	0.002	-	0.004
<sup>(a)</sup> Sps	0.010	0.009	0.032	0.058	0.016	0.016

\* FeOt total iron reported as FeO; apfu: atoms per formula unit; bdl: below detection limit

\*\* Na<sub>2</sub>O and K<sub>2</sub>O always below detection limit.

(a) Grs: Grossular; Hgr: Hydrogrossular; Adr: Andradite; Alm: Almandine; Prp: Pyrope; Sps:

Transect-2 (Vivario-Venaco)								
CO-35								
#78	#3	#4	#5	#6	#9	#10	#13	#14
34.53	33.45	34.70	34.30	35.63	34.71	34.78	34.78	33.73
0.19	0.43	0.31	0.18	0.41	0.06	0.13	<i>bdl</i>	<i>bdl</i>
6.83	7.05	8.32	6.35	8.98	4.50	7.92	5.53	8.16
19.32	19.11	17.59	20.18	16.83	22.05	17.81	20.70	17.77
0.34	0.44	1.05	0.34	3.79	0.37	1.05	1.29	0.41
0.15	<i>bdl</i>	<i>bdl</i>	0.07	<i>bdl</i>	<i>bdl</i>	<i>bdl</i>	<i>bdl</i>	<i>bdl</i>
33.50	34.83	34.02	34.48	30.97	33.92	34.16	33.81	35.18
94.86	95.32	95.99	95.89	96.62	95.62	95.85	96.11	95.24
21.22	21.22	19.35	22.43	17.73	24.51	19.79	23.00	19.75
0.23	0.02	0.18	-	0.87	-	-	-	-
1.15	2.36	1.53	1.68	0.71	0.93	1.39	1.14	2.27
2.842	2.684	2.794	2.774	2.903	2.871	2.813	2.844	2.698
0.158	0.316	0.206	0.226	0.097	0.129	0.187	0.156	0.302
0.012	0.026	0.019	0.011	0.025	0.004	0.008	-	-
0.663	0.667	0.790	0.605	0.862	0.439	0.755	0.533	0.769
1.314	1.281	1.173	1.365	1.087	1.525	1.205	1.416	1.189
0.016	0.001	0.012	-	0.060	-	-	-	-
0.024	0.030	0.072	0.023	0.262	0.026	0.072	0.089	0.028
0.018	-	-	0.008	-	-	-	-	-
2.954	2.995	2.935	2.987	2.704	3.006	2.960	2.962	3.015
0.320	0.341	0.380	0.301	0.343	0.216	0.364	0.244	0.384
0.053	0.105	0.069	0.075	0.032	0.043	0.062	0.052	0.101
0.661	0.649	0.592	0.689	0.551	0.775	0.612	0.727	0.607
0.005	-	0.004	-	0.020	-	-	-	-
0.006	-	-	0.003	-	-	-	-	-
0.008	0.010	0.024	0.008	0.087	0.009	0.024	0.029	0.009

mit.

ps: Spessartine.

#15	#16	#19
33.29	33.12	33.95
<i>bdl</i>	<i>bdl</i>	0.11
7.61	5.73	5.73
18.68	20.94	20.75
0.52	0.63	0.60
<i>bdl</i>	0.09	0.23
34.92	34.42	33.91
95.02	94.93	95.27
 20.76	 23.27	 23.06
-	-	-
2.51	2.38	1.72
 2.666	 2.679	 2.766
0.335	0.321	0.234
-	-	0.007
0.718	0.546	0.550
1.251	1.417	1.414
-	-	-
0.035	0.043	0.041
-	0.011	0.028
2.996	2.983	2.960
 0.353	 0.261	 0.260
0.112	0.107	0.078
0.635	0.722	0.717
-	-	-
-	0.004	0.009
0.012	0.014	0.014

## Representative EMPA and chemical formulas of Amphibole

Locality Sample Analysis	Transect-1		Transect-2		
	CO-38		CO-35	CO-36	
	#28	#29	#13	#29	#33
SiO <sub>2</sub> (wt%)	53.36	53.36	52.98	55.13	57.28
TiO <sub>2</sub>	0.10	0.09	0.37	0.05	0.05
Al <sub>2</sub> O <sub>3</sub>	1.29	1.07	1.48	0.56	0.55
FeOt	21.04	20.99	29.32	20.13	18.18
MnO	0.92	0.90	0.39	0.75	0.82
MgO	9.24	9.50	4.52	9.46	10.39
CaO	6.38	7.09	0.22	10.80	11.38
Na <sub>2</sub> O	3.31	3.19	6.61	0.16	0.15
K <sub>2</sub> O	0.85	0.79	0.25	0.13	0.06
Total	96.49	96.98	96.15	97.17	98.85
<i>Normalization Scheme: 13-CNK</i>					
Si (apfu)	7.625	7.608	7.953	8.000	8.000
Al	0.375	0.392	0.047	0.000	0.000
$\Sigma T$	8.000	8.000	8.000	8.000	8.000
Ti	0.018	0.018	0.042	0.006	0.005
Al	0.074	0.090	0.215	0.095	0.090
Fe <sup>3+</sup>	1.196	1.173	1.705	1.101	1.488
Mn <sup>2+</sup>	0.115	0.108	0.050	0.092	0.097
Fe <sup>2+</sup>	2.598	2.689	1.976	1.343	0.636
Mg	0.999	0.922	1.012	2.046	2.163
$\Sigma C$	5.000	5.000	5.000	4.683	4.479
Ca	1.021	0.962	0.036	1.680	1.702
Na	0.873	1.013	1.924	0.046	0.040
$\Sigma B$	1.894	1.975	1.960	1.726	1.742
Na	-	-	-	0.000	0.000
K	0.153	0.157	0.048	0.023	0.110
$\Sigma A$	0.153	0.157	0.048	0.023	0.110
O (non-W)	22.000	22.000	22.000	22.000	22.000
W (OH)	2.000	2.000	2.000	2.000	2.000
$\Sigma(T, C, B, A)$	15.047	15.132	15.008	14.432	14.331
<sup>(a)</sup> Species	Wnc	Wnc	Rbk	Act	Act

\* FeOt total iron reported as FeO; apfu: atoms per formula unit; bdl: below detection limit.  
 (a) IMA-2012 classification (Hawthorne et al., 2012), amphibole abbreviation follow Whitney et al.



Transect-3								
CO-42								
#11	#12	#1	#2	#5	6	#7	8	#17
52.03	52.11	53.36	53.36	52.87	54.02	52.47	53.71	52.80
0.31	0.18	0.10	0.09	0.07	0.09	0.09	0.00	0.07
1.74	2.13	1.29	1.07	1.29	0.84	1.29	0.96	1.30
30.33	30.35	21.04	20.99	21.94	20.45	21.93	21.71	21.72
0.30	0.38	0.92	0.90	0.97	1.00	0.87	0.95	0.78
4.33	4.08	9.24	9.50	8.87	9.82	8.89	8.89	8.50
0.71	0.52	6.38	7.09	6.33	8.08	6.51	7.12	7.08
6.00	6.03	3.31	3.19	3.59	2.70	3.24	3.14	3.55
0.32	0.29	0.85	0.79	0.93	0.76	1.09	1.17	0.88
96.06	96.06	96.49	96.98	96.86	97.75	96.38	97.66	96.68
7.830	7.827	7.964	7.957	7.915	8.000	7.896	8.000	7.993
0.170	0.173	0.036	0.043	0.085	0.000	0.104	0.000	0.007
8.000	8.000	8.000	8.000	8.000	8.000	8.000	8.000	8.000
0.035	0.021	0.012	0.010	0.008	0.010	0.010	0.001	0.008
0.139	0.205	0.190	0.145	0.142	0.146	0.125	0.169	0.224
1.922	1.950	0.663	0.539	0.677	0.385	0.709	0.492	0.258
0.038	0.048	0.117	0.113	0.123	0.126	0.111	0.119	0.100
1.895	1.863	1.963	2.079	2.070	2.148	2.052	2.212	2.491
0.972	0.914	2.055	2.113	1.980	2.168	1.995	1.975	1.919
5.001	5.001	5.000	4.999	5.000	4.983	5.002	4.968	5.000
0.114	0.083	1.019	1.133	1.016	1.283	1.049	1.136	1.149
1.751	1.755	0.959	0.867	0.984	0.717	0.945	0.864	0.851
1.865	1.838	1.978	2.000	2.000	2.000	1.994	2.000	2.000
-	-	-	0.055	0.057	0.059	-	0.043	0.191
0.061	0.055	0.162	0.151	0.177	0.143	0.208	0.223	0.170
0.061	0.055	0.162	0.206	0.234	0.202	0.208	0.266	0.361
22.000	22.000	22.000	22.000	22.000	22.000	22.000	22.000	22.000
2.000	2.000	2.000	2.000	2.000	2.000	2.000	2.000	2.000
14.927	14.894	15.140	15.205	15.234	15.185	15.204	15.234	15.361
Rbk	Rbk	Wnc						

ey and Evans (2010): riebeckite (Rbk), winchite (Wnc), actinolite (Act).



---

---

#18

51.61

1.58

1.94

21.97

0.84

7.50

8.19

2.77

0.80

97.19

7.848

0.152

*8.000*

0.181

0.196

-

0.108

2.794

1.699

*4.978*

1.334

0.666

*2.000*

0.149

0.156

*0.305*

22.000

2.000

*15.283*

Wnc



## Representative EMPA and chemical formula of Titanite

Locality Sample Analysis	Transect-1						
	CO-24		CO-25		CO-38		
	#6	#22	#34	#6	#12	#13	#30
SiO <sub>2</sub> (wt%)	30.27	29.09	29.71	29.74	30.30	29.72	30.28
TiO <sub>2</sub>	39.30	40.19	25.68	31.45	35.27	30.91	34.28
Al <sub>2</sub> O <sub>3</sub>	1.29	1.96	8.25	5.08	2.94	5.02	2.89
Fe <sub>2</sub> O <sub>3</sub>	0.69	0.95	6.70	2.54	1.39	2.11	2.37
Mn <sub>2</sub> O <sub>3</sub>	bdl	bdl	0.21	bdl	bdl	0.12	0.09
CaO	28.04	26.61	23.33	27.46	27.92	26.56	26.92
Total	100.76	100.04	94.70	97.28	98.98	95.40	97.87

<i>Formula (5 Oxygens; Si = 1 apfu)</i>							
Si (apfu)	1.000	1.000	1.000	1.000	1.000	1.000	1.000
Al	0.050	0.079	0.327	0.201	0.114	0.199	0.112
Ti	0.977	1.039	0.650	0.795	0.876	0.782	0.852
Fe <sup>3+</sup>	0.017	0.025	0.170	0.064	0.035	0.054	0.059
Ca	0.993	0.980	0.841	0.989	0.987	0.958	0.952

\* FeOt total iron reported as FeO; apfu: atoms per formula unit; bdl: below detection limit.

Transect-2							
CO-35							CO-36
#58	#59	#61	#64	#75	#79	#8	#3
31.83	30.58	30.72	30.30	29.21	31.10	31.12	30.29
26.37	29.71	27.34	28.44	32.83	29.43	27.82	36.51
5.68	4.20	6.53	5.68	6.00	4.70	6.76	2.62
4.84	4.15	3.08	2.99	4.83	3.98	3.14	0.39
0.17	0.07	<i>bdl</i>	<i>bdl</i>	<i>bdl</i>	<i>bdl</i>	<i>bdl</i>	<i>bdl</i>
26.79	28.62	27.90	28.16	22.72	27.69	28.35	27.50
96.55	98.21	96.41	96.43	96.57	97.85	98.04	98.38
1.000	1.000	1.000	1.000	1.000	1.000	1.000	1.000
0.210	0.162	0.251	0.221	0.242	0.178	0.256	0.102
0.623	0.731	0.669	0.706	0.846	0.712	0.672	0.906
0.114	0.102	0.075	0.074	0.124	0.096	0.076	0.010
0.902	1.003	0.973	0.996	0.834	0.954	0.976	0.973

Transect-3  
CO-42  
#60

27.78

30.15

4.40

7.07

0.06

23.88

94.22

1.000

0.187

0.816

0.191

0.921

## Representative EMPA and chemical formulaa of Ilvaite

Locality	Transect-1 (Castirla)						
Sample	CO-38						
Analysis	#1	#2	#5	#7	#10	#20	#21
SiO <sub>2</sub> (wt%)	28.68	29.24	29.13	28.85	28.72	29.06	28.91
TiO <sub>2</sub>	0.20	0.42	0.11	0.49	0.40	0.21	0.18
Al <sub>2</sub> O <sub>3</sub>	0.23	bdl	0.09	0.38	0.07	0.14	0.18
FeOt	49.06	48.73	49.59	48.40	49.82	48.74	48.08
MnO	2.86	3.02	3.11	2.90	2.97	2.67	2.77
MgO	0.18	0.11	0.14	0.25	0.11	0.16	0.16
CaO	13.54	13.68	13.50	13.20	13.51	13.87	13.52
Total	94.75	95.21	95.67	94.47	95.59	94.85	93.79
FeO	33.03	32.26	33.21	32.53	33.46	32.50	32.06
Fe <sub>2</sub> O <sub>3</sub>	17.82	18.30	18.21	17.64	18.18	18.05	17.81
<i>Formula (8.5 Oxygens; Al + Fe<sup>3+</sup> = 1 apfu)</i>							
Si (apfu)	2.096	2.119	2.110	2.104	2.087	2.114	2.123
Al	0.020	-	0.008	0.032	0.006	0.012	0.016
Ti	0.011	0.023	0.006	0.027	0.022	0.012	0.010
Fe <sup>2+</sup>	2.018	1.955	2.011	1.983	2.033	1.977	1.969
Fe <sup>3+</sup>	0.980	0.998	0.992	0.968	0.994	0.988	0.984
Mn	0.177	0.185	0.191	0.179	0.183	0.165	0.172
Mg	0.019	0.012	0.015	0.027	0.012	0.017	0.017
Ca	1.060	1.062	1.047	1.031	1.052	1.081	1.064

\* FeOt total iron reported as FeO; apfu: atoms per formula unit; bdl: below detection limit.

\*\* Na<sub>2</sub>O and K<sub>2</sub>O always below detection limit.



## Representative EMPA and chemical formula of Magnetite and Il

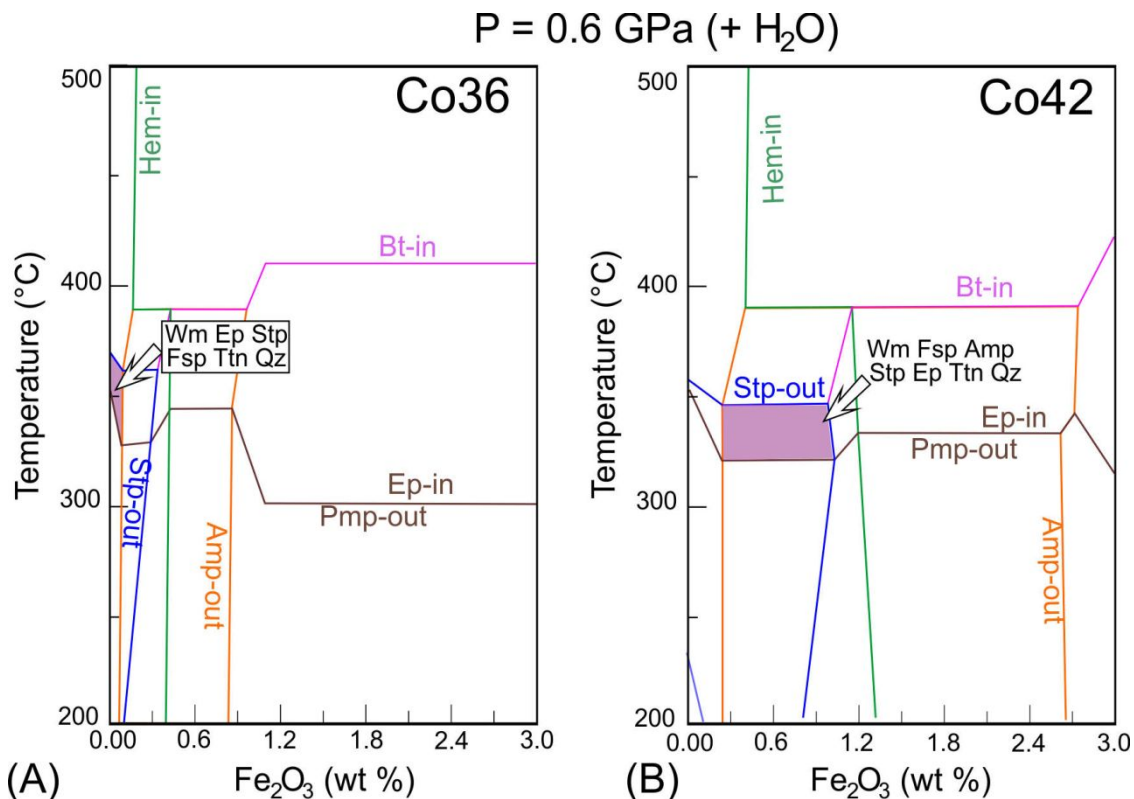
Locality	Transect-1 (Castirla)		
	CO-38		
Analysis	#8	#9	#11
SiO <sub>2</sub> (wt%)	<i>bdl</i>	<i>bdl</i>	<i>bdl</i>
TiO <sub>2</sub>	51.24	51.88	51.96
Al <sub>2</sub> O <sub>3</sub>	<i>bdl</i>	<i>bdl</i>	0.16
FeOt	39.50	38.45	37.09
MnO	7.90	7.90	8.06
MgO	0.03	0.03	0.03
Total	98.67	98.26	97.29
<i>FeO</i>	38.03	38.45	37.09
<i>Fe<sub>2</sub>O<sub>3</sub></i>	1.64	-	-
<i>Formula (3 cations)</i>			
Si (apfu)	-	-	-
Ti	0.984	1.002	1.013
Al	-	-	0.005
Fe <sup>3+</sup>	0.031	-	-
Fe <sup>2+</sup>	0.812	0.825	0.804
Mn	0.171	0.172	0.177
Mg	0.001	0.001	0.001
Ca	-	-	-

\* FeOt total iron reported as FeO; apfu: atoms per formula unit; bdl: below detection limit.

\*\* CaO, BaO, Na<sub>2</sub>O and K<sub>2</sub>O always below detection limit.

## **Imenite**

**Supplementary Material#3 – T-  $\text{Fe}_2\text{O}_3$  pseudosections calculated at 0.6 GPa for samples CO36 and CO42.**



The FeO content (wt.%) is calculated as  $\text{FeO} = \text{FeO}(\text{total}) - (\text{Fe}_2\text{O}_3 / 1.11135)$  (wt.%). Accordingly, the surplus  $\text{O}_2$  used in P-T pseudosection calculation (Table 2) is obtained as in  $\text{Fe}_2\text{O}_3$  as  $\text{O}_2 = \text{Fe}_2\text{O}_3 / (1.11125 * 0.11135) = 0.100193$  (rounded: 0.1).

## Supplementary Material#4 - Ar-Ar in-situ data, Relative abundances.

area μm <sup>2</sup>	description	<sup>36</sup> Ar [fA]	%1σ	<sup>37</sup> Ar [fA]	%1σ	<sup>38</sup> Ar [fA]	%1σ	<sup>39</sup> Ar [fA]	%1σ	<sup>40</sup> Ar [fA]	%1σ	
<b>CO24 (J = 0.00577542±0.00000347, ±1σ)</b>												
101G	60x160	Wm	0.0104	10.5	0.0075	861	0.2189	15	14.633	0.10	55.885	0.059
101H	60x160	Wm	0.0097	8.9	0.0130	390	0.1031	36	7.697	0.16	34.085	0.082
101J	100x100	Wm	0.0039	15.5	0.0375	139	0.1043	25	13.451	0.11	50.104	0.053
101K	60x160	Wm	0.0011	56.6	0.0320	134	0.0528	59	9.463	0.15	35.398	0.076
101L	60x160	Wm	0.0015	43.7	0.0759	48	0.0887	32	10.623	0.12	39.979	0.084
101N	60x160	Wm	0.0016	41.7	0.0257	261	0.1591	16	13.896	0.10	52.904	0.063
101O	60x160	Wm	0.0053	12.0	0.0025	2540	0.1105	29	11.100	0.12	47.786	0.080
101P	100x100	Wm	0.0020	30.1	0.0073	956	0.1671	15	12.186	0.12	48.187	0.083
101R	60x160	Wm	0.0436	1.6	0.0485	118	0.1383	18	12.604	0.09	61.110	0.044
101S	100x100	Wm	0.1545	0.5	0.0159	362	0.2289	10	14.964	0.07	104.382	0.027
101T	60x160	Wm	0.0021	30.0	0.0716	81	0.1336	26	10.482	0.10	40.004	0.069
101V	100x100	K-Fsp?	0.0350	2.0	0.1165	43	0.0866	33	6.972	0.21	61.019	0.064
101W	100x100	Wm	0.0028	29.6	0.0065	925	0.1575	15	12.903	0.11	54.603	0.079
216B	~60x200	Wm	-0.0003	220.5	0.5996	40	0.1050	29	5.798	0.22	23.947	0.171
216H	100x100	Wm	0.0023	24.9	0.1543	177	0.0976	39	9.162	0.12	39.040	0.064
216I	60x160	Wm	0.0097	7.1	0.2530	104	0.1286	28	8.648	0.17	34.163	0.097
216K	60x160	Wm	0.0080	8.1	0.0690	486	0.1463	18	8.577	0.15	35.664	0.100
216L	60x160	Wm	0.0162	4.5	0.1332	185	0.1219	25	8.935	0.18	39.048	0.092
216O	60x160	K-Fsp?	-0.0023	34.2	-0.0274	1256	0.1141	28	6.724	0.21	38.658	0.073
216P	100x100	K-Fsp	-0.0050	13.8	0.0894	573	0.1247	28	7.355	0.20	32.865	0.083
216R	100x100	Wm	0.0063	9.4	0.1428	284	0.0775	38	6.523	0.20	28.071	0.105
216S	100x100	Wm	0.0044	15.1	0.1416	250	0.1354	21	8.366	0.11	34.699	0.086
216U	100x100	K-Fsp	0.0346	2.0	0.6038	37	0.1980	14	12.462	0.11	180.459	0.019
216V	100x100	Wm	0.0034	18.8	0.2614	133	0.0614	58	6.780	0.16	32.277	0.105
216X	60x160	Wm	-0.0011	47.2	0.1469	207	0.0977	39	6.894	0.24	33.065	0.112
216Y	100x100	Wm(±K-Fsp?)	-0.0008	71.9	0.1523	163	0.1430	27	11.750	0.15	53.590	0.072
216Z	100x100	K-Fsp?	0.0038	17.3	0.0604	556	0.1385	26	9.824	0.20	61.924	0.062
217E	~60x160	Wm	0.0073	9.4	0.1630	197	0.0597	49	6.385	0.32	26.029	0.164
217F	30x200	K-Fsp?	0.0119	4.7	0.5410	60	0.1071	31	6.470	0.25	36.422	0.090
217H	~100x100	K-Fsp?	0.0167	3.3	0.1919	238	0.1298	25	10.295	0.15	56.088	0.053
217I	~100x100	K-Fsp?	0.0177	3.2	0.4439	98	0.0256	137	6.442	0.17	36.572	0.076
217K	~160x50	K-Fsp?	0.0060	12.2	-0.0259	1217	0.0836	50	3.046	0.46	17.851	0.247
217L	100x100	K-Fsp	0.0079	8.6	-0.0883	389	0.0620	73	4.201	0.32	23.179	0.158
217N	100x100	Wm	0.0013	42.3	0.0985	388	0.1015	38	8.692	0.14	32.033	0.090
217O	50x200	Wm	0.0004	139.8	0.1916	142	0.0499	76	4.936	0.28	18.744	0.230
217T	~60x160	Wm	0.0124	4.8	0.0715	539	0.0962	32	7.087	0.25	29.908	0.121
217U	100x100	Wm	0.0134	3.3	0.3041	91	0.0923	37	7.628	0.21	33.299	0.114
217W	100x100	Wm	-0.0021	23.5	0.1228	291	0.0893	49	7.058	0.24	25.950	0.133
217X	100x100	Wm	0.0025	25.6	0.3170	77	0.1139	32	7.646	0.20	29.098	0.123
218A	100x100	Wm	0.0035	17.7	0.1586	164	0.0972	35	9.267	0.22	35.138	0.124
218B	100x100	Wm	0.0056	9.1	0.1440	288	0.0497	66	7.908	0.22	32.399	0.123
218D	100x100	Wm(±K-Fsp?)	0.0005	107.2	0.0919	391	0.0588	68	5.387	0.24	23.449	0.154
218E	100x100	Wm	0.0022	21.4	0.1230	147	0.0393	122	4.557	0.32	18.821	0.176
218G	~160*65	K-Fsp?	0.0066	12.0	0.2895	83	0.1157	32	6.498	0.26	36.830	0.108
218H	100x100	Wm	0.0058	12.5	0.1409	150	0.1206	31	9.227	0.23	37.782	0.091
218J	100x100	Wm	0.0013	46.9	0.3835	75	0.1239	34	6.618	0.20	25.482	0.115
218K	100x100	Wm	0.0044	14.2	0.3705	87	0.1203	27	7.774	0.16	32.940	0.111
218Q	60x160	Wm	0.0026	30.3	0.0399	898	0.0808	44	4.787	0.29	19.622	0.182
218R	100x100	Wm	0.0037	19.5	0.1152	202	0.0719	49	4.911	0.24	21.078	0.124
<b>CO36 (J=0.00577996±0.00000231, ±1σ)</b>												
area μm <sup>2</sup>	description	<sup>36</sup> Ar [fA]	%1σ	<sup>37</sup> Ar [fA]	%1σ	<sup>38</sup> Ar [fA]	%1σ	<sup>39</sup> Ar [fA]	%1σ	<sup>40</sup> Ar [fA]	%1σ	
84A	100x100	Wm	0.0134	5.0	0.3587	7.94	0.1940	15	17.584	0.1	63.060	0.04
84B	100x100	Wm	0.0048	13.1	0.0023	1203.51	0.0929	36	10.588	0.1	35.906	0.06
84C	100x100	Wm	0.0187	2.6	1.4755	2.33	0.2302	12	20.425	0.1	75.577	0.04
84E	~200x60	Wm	0.0166	4.1	0.5207	4.89	0.2463	11	20.071	0.1	67.299	0.04
84F	100x100	Wm	0.0169	4.7	0.2520	11.18	0.2752	11	23.560	0.1	81.973	0.04
84G	100x100	Wm	0.0214	3.3	0.7907	3.92	0.3375	8	25.376	0.0	93.870	0.03
84I	~100x100	Wm	0.0107	7.6	1.4448	2.09	0.1372	31	12.221	0.1	44.987	0.07
84J	60x60	Wm	0.0078	9.0	0.2672	11.14	0.0726	41	7.757	0.2	27.913	0.11
84N	100x100	Wm	0.0149	4.5	0.6922	3.15	0.2343	11	16.699	0.1	60.798	0.05
84O	200x60	Wm	0.0167	3.3	1.0071	2.49	0.3304	8	24.660	0.0	85.830	0.03
84Q	~200x60	Wm	0.0099	6.6	1.4072	2.21	0.2499	14	18.754	0.1	65.353	0.06
84R	~200x60	Wm	0.0117	5.6	0.4379	6.79	0.2106	15	18.463	0.1	62.959	0.05
84S	~100x100	Wm	0.0252	3.5	0.8151	3.18	0.2127	17	17.174	0.1	63.865	0.05
84U	~100x100	Wm	0.0192	2.5	0.8859	2.92	0.1727	16	19.197	0.1	69.682	0.04

84V	~100x100	Wm	0.0209	3.6	0.7972	3.85	0.2449	14	23.686	0.1	86.167	0.04
84W	~100x100	Wm	0.0393	1.9	1.3369	2.24	0.2774	10	26.452	0.0	98.845	0.04
84Z	~100x60	Wm	0.0440	1.6	0.8061	3.69	0.2281	10	17.634	0.1	70.748	0.05
85A	100x100	Wm	0.0072	9.8	0.2735	11.30	0.2199	13	16.303	0.1	54.146	0.06
85B	~300x30	Wm	0.0243	2.3	2.3917	1.32	0.2165	14	14.452	0.1	59.391	0.05
85G	~100x60	Wm	0.0161	4.0	1.6908	1.96	0.2177	12	19.086	0.1	69.024	0.04
85H	100x100	Wm	0.0145	4.9	1.1291	2.76	0.2809	8	23.229	0.1	82.663	0.04
85I	100x100	Wm	0.0181	2.9	0.2022	13.35	0.2641	11	24.008	0.1	84.997	0.03
85K	200x60	Wm	0.0234	4.1	2.8140	0.95	0.1650	19	13.863	0.1	53.078	0.05
85L	100x100	Wm	0.0139	5.5	2.6793	1.08	0.2473	11	24.051	0.1	82.528	0.04
85M	100x100	Wm	0.0209	3.4	1.2726	2.71	0.3257	9	29.053	0.1	104.047	0.03
85O	100x100	Wm	0.0355	2.0	3.2612	0.83	0.3183	15	25.368	0.0	93.080	0.04
85P	100x100	Wm	0.0159	4.5	3.0275	0.87	0.2636	16	17.783	0.1	64.088	0.05
85Q	100x100	Wm	0.0140	4.5	3.8033	0.67	0.2093	22	14.507	0.1	54.935	0.07
235A	160x60	Wm	0.0036	20.9	0.6046	105.33	0.0373	75	2.770	0.6	12.478	0.21
235C	100x100	Wm	0.0104	5.1	1.6528	26.06	0.1515	27	9.764	0.1	35.847	0.09
235D	100x100	Wm	0.0050	11.3	0.5859	73.28	0.1017	35	9.451	0.1	32.961	0.09
235F	100x100	Wm	0.0108	5.8	1.6621	36.61	0.2250	14	14.618	0.1	49.690	0.06
235G	100x100	Wm	0.0129	5.3	0.7949	75.97	0.2720	11	18.580	0.1	66.484	0.04
235I	100x100	Wm	0.0186	2.9	0.9965	33.30	0.2481	12	18.096	0.1	66.907	0.06
235J	~200x60	Wm	0.0178	2.5	0.8791	37.38	0.1290	21	9.783	0.1	38.829	0.08
235O	100x100	Wm	0.0049	12.8	0.2563	262.88	0.1599	19	9.126	0.1	30.332	0.11
235P	100x100	Wm	0.0099	6.4	0.1753	335.10	0.2310	15	17.391	0.1	59.851	0.05
235R	100x100	Wm	0.0214	3.4	0.1201	422.30	0.0372	101	0.157	7.9	6.897	0.32
235S	100x100	Wm	0.0275	2.2	1.9890	24.27	0.1611	22	15.192	0.1	58.001	0.06
235U	100x100	Wm	0.0282	2.4	1.2144	49.58	0.2712	13	23.625	0.1	84.561	0.04
235V	200x50	Wm	0.0198	2.8	0.8121	76.57	0.1356	30	11.237	0.1	43.548	0.08
235X	200x50	Wm	0.0520	1.3	1.3289	25.64	0.2993	9	20.704	0.1	84.820	0.04
235Y	100x100	Wm	0.0054	9.4	0.1872	325.50	0.0968	29	6.058	0.2	23.266	0.14

area μm <sup>2</sup>	description	<sup>36</sup> Ar	%1σ	<sup>37</sup> Ar	%1σ	<sup>38</sup> Ar	%1σ	<sup>39</sup> Ar	%1σ	<sup>40</sup> Ar	%1σ	
		[fA]		[fA]		[fA]		[fA]		[fA]		
<b>CO42 (J=0.00577784±0.00000347, ±1σ)</b>												
91A	100x100	Wm	0.0050	12.4	0.0253	111.68	0.1883	20	12.285	0.1	52.292	0.07
91B	100x100	Wm	0.0087	6.9	0.0177	218.10	0.1802	18	11.981	0.1	51.621	0.09
91P	100x100	Wm	0.0006	141.5	0.0202	146.70	0.1956	21	17.353	0.1	68.167	0.06
91Q	100x100	Wm	0.0038	17.7	0.0720	40.06	0.1327	32	13.068	0.1	52.542	0.07
91S	100x100	Wm	0.0063	11.6	0.0386	92.68	0.0911	31	7.044	0.2	29.189	0.13
91T	100x100	Wm	0.0069	10.5	0.1198	29.82	0.2628	7	21.568	0.1	87.459	0.04
91U	100x100	Wm	0.0167	3.7	0.6444	6.73	0.0648	39	7.098	0.2	34.419	0.11
91W	100x100	Wm	0.0020	33.8	0.1960	22.08	0.2105	13	18.824	0.1	75.504	0.04
91X	100x100	Wm	0.0028	20.2	0.0293	99.99	0.2388	16	21.127	0.1	82.518	0.04
91Y	100x100	Wm	0.0028	21.0	0.0090	400.12	0.2143	12	17.441	0.1	76.909	0.04
92A	100x100	Wm	0.0058	11.0	0.1488	24.06	0.2340	16	15.338	0.1	62.175	0.06
92B	50x50	Wm	0.0018	39.3	-0.0020	2102.11	0.0960	27	7.453	0.2	34.365	0.10
92C	50x50	Wm	0.0028	25.3	0.0346	109.15	0.0844	38	4.988	0.3	27.586	0.14
92I	50x50	Wm	0.0005	147.8	0.0858	41.07	0.1262	32	6.193	0.2	24.261	0.14
92J	100x100	Wm	0.0046	13.6	0.8148	5.25	0.0816	56	6.274	0.2	28.407	0.11
92K	100x100	Wm	0.0065	11.0	0.0919	33.62	0.1593	29	8.537	0.2	35.208	0.11
92M	100x100	Wm	0.0017	36.6	0.0800	36.18	0.1154	22	13.248	0.1	74.278	0.03
92N	100x100	Wm	0.0061	11.7	0.1307	27.37	0.0170	160	8.739	0.2	35.247	0.10
92O	100x100	Wm	0.0048	14.2	0.0321	110.57	0.1256	22	14.483	0.1	58.274	0.05
92Q	100x100	Wm	0.0047	13.5	0.0426	68.20	0.1748	31	9.652	0.1	38.599	0.08
92R	~100x60	Wm	0.0159	2.9	0.0242	118.97	0.0532	101	5.331	0.3	28.624	0.10
233C	100x100	Wm	0.0006	110.1	0.3107	152.53	0.0480	105	3.539	0.4	17.350	0.38
233D	100x100	Wm	0.0055	12.7	0.1102	479.74	0.0682	67	4.297	0.3	18.146	0.26
233F	100x100	Wm	0.0070	9.0	0.4934	84.09	0.1544	16	10.329	0.2	46.358	0.11
233G	100x100	Wm	0.0136	4.6	0.8773	48.81	0.0916	33	7.477	0.2	33.030	0.13
233I	100x100	K-Fsp?	0.0088	7.7	0.2768	133.51	0.0498	117	3.924	0.3	25.830	0.16
233J	100x100	Wm	0.0020	36.5	0.1174	293.60	0.1624	37	11.871	0.1	56.194	0.07
233M	100x100	Pl	0.0095	6.4	0.4393	104.78	0.0293	120	0.061	22.5	4.676	0.71
233N	100x100	Wm	0.0048	12.2	0.0122	4607.78	0.1102	30	8.777	0.1	33.918	0.10
233Q	~200x65	Wm	0.0121	6.8	0.4346	134.25	0.1012	30	5.969	0.2	27.104	0.15
233R	100x100	Wm	0.0033	19.1	0.7987	66.68	0.2088	14	16.404	0.1	87.185	0.04
233T	100x100	Wm	0.0037	19.5	-0.4818	147.98	0.1890	16	16.672	0.1	70.385	0.04
233V	100x100	Wm	0.0017	44.8	-0.2066	306.22	0.1713	21	12.596	0.1	48.634	0.06
233X	100x100	Wm	0.0039	16.5	0.3795	198.79	0.0960	30	7.591	0.1	30.554	0.14
233Y	100x100	Wm	0.0024	19.3	0.1122	691.54	0.1275	22	8.286	0.2	32.666	0.12
234A	100x100	Wm	0.0037	15.6	0.3115	196.46	0.1691	28	15.054	0.1	59.392	0.06
234B	~100x100	Wm	0.0085	9.1	0.3768	169.12	0.2299	22	20.868	0.1	85.339	0.04
234H	100x100	Wm	0.0005	161.6	0.3347	217.40	0.1527	27	9.937	0.2	38.595	0.09
234I	100x100	Wm	0.0094	7.1	0.3371	153.37	0.2474	17	17.916	0.1	86.906	0.05
234K	160x60	K-Fsp?	-0.0011	64.4	0.5661	113.63	0.0066	775	1.747	0.9	11.537	0.33

Decay Constant 40K = 5.463 ± 0.214 E-10 1/a  
 Decay Constant 39Ar = 2.940 ± 0.016 E-07 1/h  
 Decay Constant 37Ar = 8.230 ± 0.012 E-04 1/h

Atmospheric Ratio 40/36(a) = 298.56 ± 0.30  
 Atmospheric Ratio 38/36(a) = 0.1869 ± 0.0003

Production Ratio 39/37(ca) = 0.000696 ± 0.000015  
 Production Ratio 38/37(ca) = 0.000058 ± 0.000005  
 Production Ratio 36/37(ca) = 0.000269 ± 0.000005  
 Production Ratio 40/39(k) = 0.00973 ± 0.00012  
 Production Ratio 38/39(k) = 0.01265 ± 0.00014

$^{40}\text{Ar}^*/^{39}\text{Ar}_{(\text{K})}$	$\pm 2\sigma$	Age	$\pm 2\sigma$	$^{40}\text{Ar}^*$	$^{39}\text{Ar}_{(\text{K})}$	K/Ca	$\pm 2\sigma$
		(Ma)		(%)	(%)		
3.5978	0.0453	<b>37.64</b>	<b>0.47</b>	94.2	3.5	1037	17864
4.0420	0.0685	<b>42.24</b>	<b>0.71</b>	91.3	1.9	313	2440
3.6285	0.0282	<b>37.96</b>	<b>0.29</b>	97.4	3.2	190	530
3.6980	0.0399	<b>38.68</b>	<b>0.41</b>	98.9	2.3	157	421
3.7133	0.0373	<b>38.84</b>	<b>0.39</b>	98.7	2.6	74	72
3.7631	0.0302	<b>39.36</b>	<b>0.31</b>	98.8	3.3	287	1499
4.1527	0.0363	<b>43.38</b>	<b>0.37</b>	96.5	2.7	2330	118378
3.8946	0.0322	<b>40.71</b>	<b>0.33</b>	98.5	2.9	881	16831
3.8071	0.0339	<b>39.81</b>	<b>0.35</b>	78.5	3.0	138	325
3.8828	0.0343	<b>40.59</b>	<b>0.36</b>	55.7	3.6	498	3598
3.7483	0.0366	<b>39.20</b>	<b>0.38</b>	98.2	2.5	78	125
7.2462	0.0686	<b>75.03</b>	<b>0.70</b>	82.8	1.7	32	27
4.1568	0.0402	<b>43.42</b>	<b>0.42</b>	98.2	3.1	1045	19342
4.1453	0.0738	<b>43.31</b>	<b>0.76</b>	100.4	1.4	5	4
4.1774	0.0396	<b>43.64</b>	<b>0.41</b>	98.0	2.2	31	112
3.6080	0.0499	<b>37.75</b>	<b>0.52</b>	91.3	2.1	18	38
3.8715	0.0478	<b>40.48</b>	<b>0.49</b>	93.1	2.1	66	641
3.8192	0.0518	<b>39.94</b>	<b>0.54</b>	87.4	2.2	36	132
5.8428	0.0758	<b>60.74</b>	<b>0.78</b>	101.6	1.6	-130	3264
4.6632	0.0607	<b>48.64</b>	<b>0.62</b>	104.4	1.8	44	500
4.0060	0.0580	<b>41.87</b>	<b>0.60</b>	93.1	1.6	24	138
3.9829	0.0491	<b>41.63</b>	<b>0.51</b>	96.0	2.0	31	156
13.6460	0.0459	<b>138.81</b>	<b>0.45</b>	94.2	3.0	11	8
4.6045	0.0596	<b>48.04</b>	<b>0.61</b>	96.7	1.6	14	37
4.8368	0.0529	<b>50.43</b>	<b>0.54</b>	100.8	1.7	25	103
4.5725	0.0332	<b>47.71</b>	<b>0.34</b>	100.3	2.8	41	133
6.1780	0.0483	<b>64.17</b>	<b>0.49</b>	98.0	2.4	86	958
3.7271	0.0702	<b>38.98</b>	<b>0.73</b>	91.4	1.5	21	82
5.0767	0.0585	<b>52.89</b>	<b>0.60</b>	90.2	1.6	6	8
4.9551	0.0363	<b>51.64</b>	<b>0.37</b>	90.9	2.5	28	135
4.8521	0.0563	<b>50.59</b>	<b>0.58</b>	85.5	1.5	8	15
5.2667	0.1541	<b>54.84</b>	<b>1.58</b>	89.9	0.7	-62	1518
4.9483	0.1040	<b>51.57</b>	<b>1.07</b>	89.7	1.0	-25	196
3.6311	0.0411	<b>37.99</b>	<b>0.43</b>	98.5	2.1	47	363
3.7664	0.0754	<b>39.39</b>	<b>0.78</b>	99.2	1.2	14	39
3.6870	0.0548	<b>38.57</b>	<b>0.57</b>	87.4	1.7	53	567
3.8325	0.0404	<b>40.07</b>	<b>0.42</b>	87.8	1.8	13	24
3.7559	0.0467	<b>39.28</b>	<b>0.48</b>	102.2	1.7	30	177
3.7002	0.0541	<b>38.70</b>	<b>0.56</b>	97.2	1.8	13	20
3.6708	0.0442	<b>38.40</b>	<b>0.46</b>	96.8	2.2	31	102
3.8783	0.0440	<b>40.55</b>	<b>0.45</b>	94.7	1.9	29	167
4.3172	0.0638	<b>45.08</b>	<b>0.66</b>	99.2	1.3	31	243
3.9760	0.0695	<b>41.56</b>	<b>0.72</b>	96.3	1.1	20	58
5.3576	0.0793	<b>55.78</b>	<b>0.81</b>	94.5	1.6	12	20
3.8977	0.0513	<b>40.75</b>	<b>0.53</b>	95.2	2.2	35	104
3.7868	0.0588	<b>39.60</b>	<b>0.61</b>	98.3	1.6	9	14
4.0630	0.0507	<b>42.46</b>	<b>0.52</b>	95.9	1.9	11	19
3.9310	0.1014	<b>41.09</b>	<b>1.05</b>	95.9	1.2	64	1142
4.0626	0.0899	<b>42.45</b>	<b>0.93</b>	94.6	1.2	23	91
$^{40}\text{Ar}^*/^{39}\text{Ar}_{(\text{K})}$	$\pm 2\sigma$	Age	$\pm 2\sigma$	$^{40}\text{Ar}^*$	$^{39}\text{Ar}_{(\text{K})}$	K/Ca	$\pm 2\sigma$
		(Ma)		(%)	(%)		
3.35	0.02	<b>35.12</b>	<b>0.25</b>	93.5	2.4	26.0	4.9
3.25	0.04	<b>34.03</b>	<b>0.38</b>	95.7	1.5	2490	59933
3.42	0.02	<b>35.87</b>	<b>0.16</b>	92.5	2.8	7.34	0.81
3.10	0.02	<b>32.50</b>	<b>0.22</b>	92.4	2.8	20.4	2.9
3.26	0.02	<b>34.13</b>	<b>0.22</b>	93.6	3.2	50	12
3.44	0.02	<b>36.04</b>	<b>0.18</b>	93.0	3.5	17.0	2.2
3.42	0.04	<b>35.84</b>	<b>0.43</b>	92.9	1.7	4.48	0.49
3.29	0.06	<b>34.51</b>	<b>0.58</b>	91.5	1.1	15.4	3.8
3.37	0.02	<b>35.28</b>	<b>0.26</b>	92.5	2.3	12.8	1.5
3.27	0.01	<b>34.29</b>	<b>0.15</b>	94.0	3.4	13.0	1.5
3.32	0.02	<b>34.83</b>	<b>0.22</b>	95.4	2.6	7.06	0.77
3.21	0.02	<b>33.68</b>	<b>0.23</b>	94.2	2.5	22.3	3.8
3.27	0.03	<b>34.32</b>	<b>0.32</b>	88.0	2.4	11.2	1.3
3.33	0.02	<b>34.85</b>	<b>0.17</b>	91.6	2.6	11.5	1.3

3.37	0.02	<b>35.29</b>	<b>0.20</b>	92.6	3.3	15.7	2.0
3.29	0.02	<b>34.45</b>	<b>0.18</b>	88.0	3.6	10.5	1.1
3.26	0.02	<b>34.19</b>	<b>0.26</b>	81.3	2.4	11.6	1.4
3.18	0.03	<b>33.35</b>	<b>0.28</b>	95.8	2.2	31.6	7.8
3.61	0.02	<b>37.81</b>	<b>0.26</b>	87.8	2.0	3.20	0.33
3.36	0.02	<b>35.22</b>	<b>0.22</b>	92.9	2.6	5.98	0.64
3.37	0.02	<b>35.27</b>	<b>0.20</b>	94.6	3.2	10.9	1.2
3.31	0.01	<b>34.65</b>	<b>0.15</b>	93.4	3.3	63	18
3.33	0.04	<b>34.91</b>	<b>0.44</b>	87.0	1.9	2.61	0.27
3.26	0.02	<b>34.15</b>	<b>0.20</b>	94.9	3.3	4.76	0.49
3.36	0.02	<b>35.22</b>	<b>0.16</b>	93.8	4.0	12.1	1.4
3.25	0.02	<b>34.09</b>	<b>0.18</b>	88.6	3.5	4.12	0.42
3.34	0.02	<b>35.02</b>	<b>0.26</b>	92.7	2.4	3.11	0.32
3.51	0.03	<b>36.78</b>	<b>0.28</b>	92.7	2.0	2.02	0.20
4.13	0.17	<b>43.16</b>	<b>1.79</b>	91.6	0.4	2.4	5.1
3.36	0.03	<b>35.20</b>	<b>0.36</b>	91.5	1.3	3.1	1.7
3.32	0.04	<b>34.84</b>	<b>0.40</b>	95.3	1.3	8.5	12.6
3.18	0.03	<b>33.33</b>	<b>0.29</b>	93.5	2.0	4.7	3.4
3.36	0.02	<b>35.26</b>	<b>0.24</b>	94.0	2.6	12	19
3.39	0.02	<b>35.47</b>	<b>0.20</b>	91.6	2.5	9.6	6.5
3.42	0.03	<b>35.86</b>	<b>0.31</b>	86.2	1.3	5.9	4.4
3.15	0.04	<b>33.08</b>	<b>0.46</b>	94.9	1.3	19	99
3.26	0.02	<b>34.19</b>	<b>0.24</b>	94.8	2.4	53	352
3.34	2.85	<b>35.03</b>	<b>29.63</b>	7.6	0.0	0.7	5.9
3.28	0.03	<b>34.36</b>	<b>0.27</b>	85.9	2.1	4.0	2.0
3.22	0.02	<b>33.73</b>	<b>0.19</b>	89.9	3.2	10.3	10.3
3.35	0.03	<b>35.07</b>	<b>0.33</b>	86.4	1.5	7.3	11.3
3.34	0.02	<b>35.02</b>	<b>0.21</b>	81.6	2.8	8.3	4.3
3.57	0.06	<b>37.33</b>	<b>0.58</b>	92.8	0.8	17	112

$^{40}\text{Ar}^*/^{39}\text{Ar}_{(\text{K})}$	$\pm 2\sigma$	Age (Ma)	$\pm 2\sigma$	$^{40}\text{Ar}^*$	$^{39}\text{Ar}_{(\text{K})}$	K/Ca	$\pm 2\sigma$
				(%)	(%)		
4.13	0.03	<b>43.12</b>	<b>0.33</b>	96.9	2.8	257	576
4.08	0.03	<b>42.68</b>	<b>0.34</b>	94.8	2.8	359	1568
3.91	0.03	<b>40.88</b>	<b>0.30</b>	99.5	4.0	455	1335
3.92	0.03	<b>41.05</b>	<b>0.33</b>	97.6	3.0	96	78
3.87	0.07	<b>40.45</b>	<b>0.67</b>	93.3	1.6	97	179
3.95	0.02	<b>41.30</b>	<b>0.22</b>	97.4	5.0	95	58
4.15	0.06	<b>43.32</b>	<b>0.57</b>	85.5	1.6	5.8	1.0
3.97	0.02	<b>41.52</b>	<b>0.23</b>	99.0	4.4	51	23
3.86	0.02	<b>40.34</b>	<b>0.18</b>	98.7	4.9	382	764
4.35	0.02	<b>45.46</b>	<b>0.22</b>	98.7	4.0	1021	8175
3.93	0.03	<b>41.12</b>	<b>0.27</b>	97.0	3.6	55	27
4.53	0.06	<b>47.28</b>	<b>0.62</b>	98.2	1.7	-1978	83151
5.36	0.09	<b>55.78</b>	<b>0.93</b>	96.8	1.2	76	167
3.88	0.08	<b>40.62</b>	<b>0.80</b>	99.1	1.4	38	32
4.31	0.06	<b>45.04</b>	<b>0.65</b>	95.2	1.5	4.08	0.59
3.89	0.05	<b>40.67</b>	<b>0.54</b>	94.3	2.0	49	33
5.56	0.03	<b>57.87</b>	<b>0.31</b>	99.2	3.1	88	64
3.82	0.05	<b>39.94</b>	<b>0.52</b>	94.7	2.0	35	20
3.92	0.03	<b>40.94</b>	<b>0.31</b>	97.3	3.4	239	529
3.84	0.04	<b>40.20</b>	<b>0.42</b>	96.1	2.2	120	164
4.47	0.06	<b>46.68</b>	<b>0.60</b>	83.3	1.2	117	277
4.85	0.12	<b>50.60</b>	<b>1.24</b>	99.0	0.8	6	18
3.83	0.10	<b>40.09</b>	<b>1.08</b>	90.8	1.0	21	198
4.28	0.04	<b>44.72</b>	<b>0.42</b>	95.4	2.4	11	19
3.88	0.05	<b>40.54</b>	<b>0.57</b>	87.7	1.7	4.5	4.4
5.91	0.11	<b>61.45</b>	<b>1.16</b>	89.8	0.9	8	20
4.68	0.04	<b>48.79</b>	<b>0.40</b>	98.8	2.8	54	315
31.22	15.41	<b>303.34</b>	<b>137.81</b>	40.3	0.0	0.07	0.16
3.69	0.04	<b>38.62</b>	<b>0.45</b>	95.5	2.0	383	35263
3.93	0.09	<b>41.10</b>	<b>0.90</b>	86.5	1.4	7	20
5.25	0.03	<b>54.69</b>	<b>0.27</b>	98.8	3.8	11	15
4.14	0.03	<b>43.30</b>	<b>0.29</b>	98.1	3.9	-18	54
3.81	0.04	<b>39.86</b>	<b>0.39</b>	98.7	2.9	-32	198
3.87	0.05	<b>40.45</b>	<b>0.56</b>	96.1	1.8	11	42
3.85	0.04	<b>40.25</b>	<b>0.41</b>	97.6	1.9	39	541
3.86	0.03	<b>40.42</b>	<b>0.26</b>	97.9	3.5	26	101
3.96	0.02	<b>41.40</b>	<b>0.24</b>	96.8	4.8	29	99
3.86	0.05	<b>40.41</b>	<b>0.49</b>	99.5	2.3	16	68
4.69	0.02	<b>48.90</b>	<b>0.26</b>	96.6	4.2	28	86
6.81	0.28	<b>70.62</b>	<b>2.84</b>	103.1	0.4	1.6	3.7

Table SM 1. Ar-Ar in-situ data. Relative abundances.

area μm <sup>2</sup>	description	<sup>36</sup> Ar [fA]	%1σ	<sup>37</sup> Ar [fA]	%1σ	<sup>38</sup> Ar [fA]	%1σ	<sup>39</sup> Ar [fA]	%1σ	<sup>40</sup> Ar [fA]	%1σ	
<b>CO24 (J = 0.00577542±0.00000347, ±1σ)</b>												
101G	60x160	WM	0.0104	10.5	0.0075	861	0.2189	15	14.633	0.10	55.885	0.059
101H	60x160	WM	0.0097	8.9	0.0130	390	0.1031	36	7.697	0.16	34.085	0.082
101J	100x100	WM	0.0039	15.5	0.0375	139	0.1043	25	13.451	0.11	50.104	0.053
101K	60x160	WM	0.0011	56.6	0.0320	134	0.0528	59	9.463	0.15	35.398	0.076
101L	60x160	WM	0.0015	43.7	0.0759	48	0.0887	32	10.623	0.12	39.979	0.084
101N	60x160	WM	0.0016	41.7	0.0257	261	0.1591	16	13.896	0.10	52.904	0.063
101O	60x160	WM	0.0053	12.0	0.0025	2540	0.1105	29	11.100	0.12	47.786	0.080
101P	100x100	WM	0.0020	30.1	0.0073	956	0.1671	15	12.186	0.12	48.187	0.083
101R	60x160	WM	0.0436	1.6	0.0485	118	0.1383	18	12.604	0.09	61.110	0.044
101S	100x100	WM	0.1545	0.5	0.0159	362	0.2289	10	14.964	0.07	104.382	0.027
101T	60x160	WM	0.0021	30.0	0.0716	81	0.1336	26	10.482	0.10	40.004	0.069
101V	100x100	Kfs?	0.0350	2.0	0.1165	43	0.0866	33	6.972	0.21	61.019	0.064
101W	100x100	WM	0.0028	29.6	0.0065	925	0.1575	15	12.903	0.11	54.603	0.079
216B	~60x200	WM	-0.0003	220.5	0.5996	40	0.1050	29	5.798	0.22	23.947	0.171
216H	100x100	WM	0.0023	24.9	0.1543	177	0.0976	39	9.162	0.12	39.040	0.064
216I	60x160	WM	0.0097	7.1	0.2530	104	0.1286	28	8.648	0.17	34.163	0.097
216K	60x160	WM	0.0080	8.1	0.0690	486	0.1463	18	8.577	0.15	35.664	0.100
216L	60x160	WM	0.0162	4.5	0.1332	185	0.1219	25	8.935	0.18	39.048	0.092
216O	60x160	Kfs?	-0.0023	34.2	-0.0274	1256	0.1141	28	6.724	0.21	38.658	0.073
216P	100x100	WM(±Kfs?)	-0.0050	13.8	0.0894	573	0.1247	28	7.355	0.20	32.865	0.083
216R	100x100	WM	0.0063	9.4	0.1428	284	0.0775	38	6.523	0.20	28.071	0.105
216S	100x100	WM	0.0044	15.1	0.1416	250	0.1354	21	8.366	0.11	34.699	0.086
216U	100x100	Kfs	0.0346	2.0	0.6038	37	0.1980	14	12.462	0.11	180.459	0.019
216V	100x100	WM	0.0034	18.8	0.2614	133	0.0614	58	6.780	0.16	32.277	0.105
216X	60x160	WM	-0.0011	47.2	0.1469	207	0.0977	39	6.894	0.24	33.065	0.112
216Y	100x100	WM(±Kfs?)	-0.0008	71.9	0.1523	163	0.1430	27	11.750	0.15	53.590	0.072
216Z	100x100	Kfs?	0.0038	17.3	0.0604	556	0.1385	26	9.824	0.20	61.924	0.062
217E	~60x160	WM	0.0073	9.4	0.1630	197	0.0597	49	6.385	0.32	26.029	0.164
217F	30x200	Kfs?	0.0119	4.7	0.5410	60	0.1071	31	6.470	0.25	36.422	0.090
217H	~100x100	Kfs?	0.0167	3.3	0.1919	238	0.1298	25	10.295	0.15	56.088	0.053
217I	~100x100	Kfs?	0.0177	3.2	0.4439	98	0.0256	137	6.442	0.17	36.572	0.076
217K	~160x50	Kfs?	0.0060	12.2	-0.0259	1217	0.0836	50	3.046	0.46	17.851	0.247
217L	100x100	Kfs	0.0079	8.6	-0.0883	389	0.0620	73	4.201	0.32	23.179	0.158
217N	100x100	WM	0.0013	42.3	0.0985	388	0.1015	38	8.692	0.14	32.033	0.090
217O	50x200	WM	0.0004	139.8	0.1916	142	0.0499	76	4.936	0.28	18.744	0.230
217T	~60x160	WM	0.0124	4.8	0.0715	539	0.0962	32	7.087	0.25	29.908	0.121
217U	100x100	WM	0.0134	3.3	0.3041	91	0.0923	37	7.628	0.21	33.299	0.114
217W	100x100	WM	-0.0021	23.5	0.1228	291	0.0893	49	7.058	0.24	25.950	0.133
217X	100x100	WM	0.0025	25.6	0.3170	77	0.1139	32	7.646	0.20	29.098	0.123
218A	100x100	WM	0.0035	17.7	0.1586	164	0.0972	35	9.267	0.22	35.138	0.124
218B	100x100	WM	0.0056	9.1	0.1440	288	0.0497	66	7.908	0.22	32.399	0.123
218D	100x100	WM(±Kfs?)	0.0005	107.2	0.0919	391	0.0588	68	5.387	0.24	23.449	0.154
218E	100x100	WM	0.0022	21.4	0.1230	147	0.0393	122	4.557	0.32	18.821	0.176
218G	~160*65	Kfs?	0.0066	12.0	0.2895	83	0.1157	32	6.498	0.26	36.830	0.108
218H	100x100	WM	0.0058	12.5	0.1409	150	0.1206	31	9.227	0.23	37.782	0.091
218J	100x100	WM	0.0013	46.9	0.3835	75	0.1239	34	6.618	0.20	25.482	0.115
218K	100x100	WM	0.0044	14.2	0.3705	87	0.1203	27	7.774	0.16	32.940	0.111
218Q	60x160	WM	0.0026	30.3	0.0399	898	0.0808	44	4.787	0.29	19.622	0.182
218R	100x100	WM	0.0037	19.5	0.1152	202	0.0719	49	4.911	0.24	21.078	0.124
area μm <sup>2</sup>	description	<sup>36</sup> Ar [fA]	%1σ	<sup>37</sup> Ar [fA]	%1σ	<sup>38</sup> Ar [fA]	%1σ	<sup>39</sup> Ar [fA]	%1σ	<sup>40</sup> Ar [fA]	%1σ	
<b>CO36 (J=0.00577996±0.00000231, ±1σ)</b>												
84A	100x100	WM	0.0134	5.0	0.3587	7.94	0.1940	15	17.584	0.1	63.060	0.04
84B	100x100	WM	0.0048	13.1	0.0023	1203.51	0.0929	36	10.588	0.1	35.906	0.06
84C	100x100	WM	0.0187	2.6	1.4755	2.33	0.2302	12	20.425	0.1	75.577	0.04
84E	~200x60	WM	0.0166	4.1	0.5207	4.89	0.2463	11	20.071	0.1	67.299	0.04
84F	100x100	WM	0.0169	4.7	0.2520	11.18	0.2752	11	23.560	0.1	81.973	0.04
84G	100x100	WM	0.0214	3.3	0.7907	3.92	0.3375	8	25.376	0.0	93.870	0.03
84I	~100x100	WM	0.0107	7.6	1.4448	2.09	0.1372	31	12.221	0.1	44.987	0.07
84J	60x60	WM	0.0078	9.0	0.2672	11.14	0.0726	41	7.757	0.2	27.913	0.11
84N	100x100	WM	0.0149	4.5	0.6922	3.15	0.2343	11	16.699	0.1	60.798	0.05
84O	200x60	WM	0.0167	3.3	1.0071	2.49	0.3304	8	24.660	0.0	85.830	0.03
84Q	~200x60	WM	0.0099	6.6	1.4072	2.21	0.2499	14	18.754	0.1	65.353	0.06
84R	~200x60	WM	0.0117	5.6	0.4379	6.79	0.2106	15	18.463	0.1	62.959	0.05
84S	~100x100	WM	0.0252	3.5	0.8151	3.18	0.2127	17	17.174	0.1	63.865	0.05
84U	~100x100	WM	0.0192	2.5	0.8859	2.92	0.1727	16	19.197	0.1	69.682	0.04

84V	~100x100	WM	0.0209	3.6	0.7972	3.85	0.2449	14	23.686	0.1	86.167	0.04
84W	~100x100	WM	0.0393	1.9	1.3369	2.24	0.2774	10	26.452	0.0	98.845	0.04
84Z	~100x60	WM	0.0440	1.6	0.8061	3.69	0.2281	10	17.634	0.1	70.748	0.05
85A	100x100	WM	0.0072	9.8	0.2735	11.30	0.2199	13	16.303	0.1	54.146	0.06
85B	~300x30	WM	0.0243	2.3	2.3917	1.32	0.2165	14	14.452	0.1	59.391	0.05
85G	~100x60	WM	0.0161	4.0	1.6908	1.96	0.2177	12	19.086	0.1	69.024	0.04
85H	100x100	WM	0.0145	4.9	1.1291	2.76	0.2809	8	23.229	0.1	82.663	0.04
85I	100x100	WM	0.0181	2.9	0.2022	13.35	0.2641	11	24.008	0.1	84.997	0.03
85K	200x60	WM	0.0234	4.1	2.8140	0.95	0.1650	19	13.863	0.1	53.078	0.05
85L	100x100	WM	0.0139	5.5	2.6793	1.08	0.2473	11	24.051	0.1	82.528	0.04
85M	100x100	WM	0.0209	3.4	1.2726	2.71	0.3257	9	29.053	0.1	104.047	0.03
85O	100x100	WM	0.0355	2.0	3.2612	0.83	0.3183	15	25.368	0.0	93.080	0.04
85P	100x100	WM	0.0159	4.5	3.0275	0.87	0.2636	16	17.783	0.1	64.088	0.05
85Q	100x100	WM	0.0140	4.5	3.8033	0.67	0.2093	22	14.507	0.1	54.935	0.07
235A	160x60	WM	0.0036	20.9	0.6046	105.33	0.0373	75	2.770	0.6	12.478	0.21
235C	100x100	WM	0.0104	5.1	1.6528	26.06	0.1515	27	9.764	0.1	35.847	0.09
235D	100x100	WM	0.0050	11.3	0.5859	73.28	0.1017	35	9.451	0.1	32.961	0.09
235F	100x100	WM	0.0108	5.8	1.6621	36.61	0.2250	14	14.618	0.1	49.690	0.06
235G	100x100	WM	0.0129	5.3	0.7949	75.97	0.2720	11	18.580	0.1	66.484	0.04
235I	100x100	WM	0.0186	2.9	0.9965	33.30	0.2481	12	18.096	0.1	66.907	0.06
235J	~200x60	WM	0.0178	2.5	0.8791	37.38	0.1290	21	9.783	0.1	38.829	0.08
235O	100x100	WM	0.0049	12.8	0.2563	262.88	0.1599	19	9.126	0.1	30.332	0.11
235P	100x100	WM	0.0099	6.4	0.1753	335.10	0.2310	15	17.391	0.1	59.851	0.05
235R	100x100	WM	0.0214	3.4	0.1201	422.30	0.0372	101	0.157	7.9	6.897	0.32
235S	100x100	WM	0.0275	2.2	1.9890	24.27	0.1611	22	15.192	0.1	58.001	0.06
235U	100x100	WM	0.0282	2.4	1.2144	49.58	0.2712	13	23.625	0.1	84.561	0.04
235V	200x50	WM	0.0198	2.8	0.8121	76.57	0.1356	30	11.237	0.1	43.548	0.08
235X	200x50	WM	0.0520	1.3	1.3289	25.64	0.2993	9	20.704	0.1	84.820	0.04
235Y	100x100	WM	0.0054	9.4	0.1872	325.50	0.0968	29	6.058	0.2	23.266	0.14

area μm <sup>2</sup>	description	<sup>36</sup> Ar	%1σ	<sup>37</sup> Ar	%1σ	<sup>38</sup> Ar	%1σ	<sup>39</sup> Ar	%1σ	<sup>40</sup> Ar	%1σ	
		[fA]		[fA]		[fA]		[fA]		[fA]		
<b>CO42 (J=0.00577784±0.00000347, ±1σ)</b>												
91A	100x100	WM	0.0050	12.4	0.0253	111.68	0.1883	20	12.285	0.1	52.292	0.07
91B	100x100	WM	0.0087	6.9	0.0177	218.10	0.1802	18	11.981	0.1	51.621	0.09
91P	100x100	WM	0.0006	141.5	0.0202	146.70	0.1956	21	17.353	0.1	68.167	0.06
91Q	100x100	WM	0.0038	17.7	0.0720	40.06	0.1327	32	13.068	0.1	52.542	0.07
91S	100x100	WM	0.0063	11.6	0.0386	92.68	0.0911	31	7.044	0.2	29.189	0.13
91T	100x100	WM	0.0069	10.5	0.1198	29.82	0.2628	7	21.568	0.1	87.459	0.04
91U	100x100	WM	0.0167	3.7	0.6444	6.73	0.0648	39	7.098	0.2	34.419	0.11
91W	100x100	WM	0.0020	33.8	0.1960	22.08	0.2105	13	18.824	0.1	75.504	0.04
91X	100x100	WM	0.0028	20.2	0.0293	99.99	0.2388	16	21.127	0.1	82.518	0.04
91Y	100x100	WM	0.0028	21.0	0.0090	400.12	0.2143	12	17.441	0.1	76.909	0.04
92A	100x100	WM	0.0058	11.0	0.1488	24.06	0.2340	16	15.338	0.1	62.175	0.06
92B	50x50	WM	0.0018	39.3	-0.0020	2102.11	0.0960	27	7.453	0.2	34.365	0.10
92C	50x50	WM	0.0028	25.3	0.0346	109.15	0.0844	38	4.988	0.3	27.586	0.14
92I	50x50	WM	0.0005	147.8	0.0858	41.07	0.1262	32	6.193	0.2	24.261	0.14
92J	100x100	WM	0.0046	13.6	0.8148	5.25	0.0816	56	6.274	0.2	28.407	0.11
92K	100x100	WM	0.0065	11.0	0.0919	33.62	0.1593	29	8.537	0.2	35.208	0.11
92M	100x100	WM	0.0017	36.6	0.0800	36.18	0.1154	22	13.248	0.1	74.278	0.03
92N	100x100	WM	0.0061	11.7	0.1307	27.37	0.0170	160	8.739	0.2	35.247	0.10
92O	100x100	WM	0.0048	14.2	0.0321	110.57	0.1256	22	14.483	0.1	58.274	0.05
92Q	100x100	WM	0.0047	13.5	0.0426	68.20	0.1748	31	9.652	0.1	38.599	0.08
92R	~100x60	WM	0.0159	2.9	0.0242	118.97	0.0532	101	5.331	0.3	28.624	0.10
233C	100x100	WM	0.0006	110.1	0.3107	152.53	0.0480	105	3.539	0.4	17.350	0.38
233D	100x100	WM	0.0055	12.7	0.1102	479.74	0.0682	67	4.297	0.3	18.146	0.26
233F	100x100	WM	0.0070	9.0	0.4934	84.09	0.1544	16	10.329	0.2	46.358	0.11
233G	100x100	WM	0.0136	4.6	0.8773	48.81	0.0916	33	7.477	0.2	33.030	0.13
233I	100x100	Kfs?	0.0088	7.7	0.2768	133.51	0.0498	117	3.924	0.3	25.830	0.16
233J	100x100	WM	0.0020	36.5	0.1174	293.60	0.1624	37	11.871	0.1	56.194	0.07
233M	100x100	PI	0.0095	6.4	0.4393	104.78	0.0293	120	0.061	22.5	4.676	0.71
233N	100x100	WM	0.0048	12.2	0.0122	4607.78	0.1102	30	8.777	0.1	33.918	0.10
233Q	~200x65	WM	0.0121	6.8	0.4346	134.25	0.1012	30	5.969	0.2	27.104	0.15
233R	100x100	WM	0.0033	19.1	0.7987	66.68	0.2088	14	16.404	0.1	87.185	0.04
233T	100x100	WM	0.0037	19.5	-0.4818	147.98	0.1890	16	16.672	0.1	70.385	0.04
233V	100x100	WM	0.0017	44.8	-0.2066	306.22	0.1713	21	12.596	0.1	48.634	0.06
233X	100x100	WM	0.0039	16.5	0.3795	198.79	0.0960	30	7.591	0.1	30.554	0.14
233Y	100x100	WM	0.0024	19.3	0.1122	691.54	0.1275	22	8.286	0.2	32.666	0.12
234A	100x100	WM	0.0037	15.6	0.3115	196.46	0.1691	28	15.054	0.1	59.392	0.06
234B	~100x100	WM	0.0085	9.1	0.3768	169.12	0.2299	22	20.868	0.1	85.339	0.04
234H	100x100	WM	0.0005	161.6	0.3347	217.40	0.1527	27	9.937	0.2	38.595	0.09
234I	100x100	WM	0.0094	7.1	0.3371	153.37	0.2474	17	17.916	0.1	86.906	0.05
234K	160x60	Kfs?	-0.0011	64.4	0.5661	113.63	0.0066	775	1.747	0.9	11.537	0.33

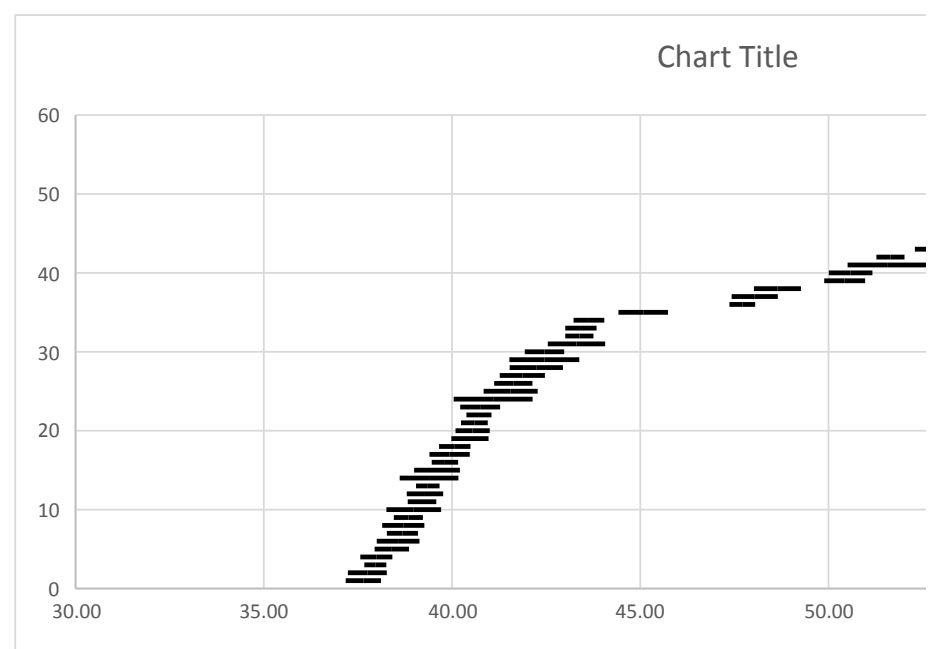
$^{40}\text{Ar}^*/^{39}\text{Ar}_{(\text{K})}$	$\pm 2\sigma$	Age	$\pm 2\sigma$	$^{40}\text{Ar}^*$	$^{39}\text{Ar}_{(\text{K})}$	K/Ca	$\pm 2\sigma$
		(Ma)		(%)	(%)		
3.5978	0.0453	<b>37.64</b>	<b>0.47</b>	94.2	3.5	1037	17864
4.0420	0.0685	<b>42.24</b>	<b>0.71</b>	91.3	1.9	313	2440
3.6285	0.0282	<b>37.96</b>	<b>0.29</b>	97.4	3.2	190	530
3.6980	0.0399	<b>38.68</b>	<b>0.41</b>	98.9	2.3	157	421
3.7133	0.0373	<b>38.84</b>	<b>0.39</b>	98.7	2.6	74	72
3.7631	0.0302	<b>39.36</b>	<b>0.31</b>	98.8	3.3	287	1499
4.1527	0.0363	<b>43.38</b>	<b>0.37</b>	96.5	2.7	2330	118378
3.8946	0.0322	<b>40.71</b>	<b>0.33</b>	98.5	2.9	881	16831
3.8071	0.0339	<b>39.81</b>	<b>0.35</b>	78.5	3.0	138	325
3.8828	0.0343	<b>40.59</b>	<b>0.36</b>	55.7	3.6	498	3598
3.7483	0.0366	<b>39.20</b>	<b>0.38</b>	98.2	2.5	78	125
7.2462	0.0686	<b>75.03</b>	<b>0.70</b>	82.8	1.7	32	27
4.1568	0.0402	<b>43.42</b>	<b>0.42</b>	98.2	3.1	1045	19342
4.1453	0.0738	<b>43.31</b>	<b>0.76</b>	100.4	1.4	5	4
4.1774	0.0396	<b>43.64</b>	<b>0.41</b>	98.0	2.2	31	112
3.6080	0.0499	<b>37.75</b>	<b>0.52</b>	91.3	2.1	18	38
3.8715	0.0478	<b>40.48</b>	<b>0.49</b>	93.1	2.1	66	641
3.8192	0.0518	<b>39.94</b>	<b>0.54</b>	87.4	2.2	36	132
5.8428	0.0758	<b>60.74</b>	<b>0.78</b>	101.6	1.6	-130	3264
4.6632	0.0607	<b>48.64</b>	<b>0.62</b>	104.4	1.8	44	500
4.0060	0.0580	<b>41.87</b>	<b>0.60</b>	93.1	1.6	24	138
3.9829	0.0491	<b>41.63</b>	<b>0.51</b>	96.0	2.0	31	156
13.6460	0.0459	<b>138.81</b>	<b>0.45</b>	94.2	3.0	11	8
4.6045	0.0596	<b>48.04</b>	<b>0.61</b>	96.7	1.6	14	37
4.8368	0.0529	<b>50.43</b>	<b>0.54</b>	100.8	1.7	25	103
4.5725	0.0332	<b>47.71</b>	<b>0.34</b>	100.3	2.8	41	133
6.1780	0.0483	<b>64.17</b>	<b>0.49</b>	98.0	2.4	86	958
3.7271	0.0702	<b>38.98</b>	<b>0.73</b>	91.4	1.5	21	82
5.0767	0.0585	<b>52.89</b>	<b>0.60</b>	90.2	1.6	6	8
4.9551	0.0363	<b>51.64</b>	<b>0.37</b>	90.9	2.5	28	135
4.8521	0.0563	<b>50.59</b>	<b>0.58</b>	85.5	1.5	8	15
5.2667	0.1541	<b>54.84</b>	<b>1.58</b>	89.9	0.7	-62	1518
4.9483	0.1040	<b>51.57</b>	<b>1.07</b>	89.7	1.0	-25	196
3.6311	0.0411	<b>37.99</b>	<b>0.43</b>	98.5	2.1	47	363
3.7664	0.0754	<b>39.39</b>	<b>0.78</b>	99.2	1.2	14	39
3.6870	0.0548	<b>38.57</b>	<b>0.57</b>	87.4	1.7	53	567
3.8325	0.0404	<b>40.07</b>	<b>0.42</b>	87.8	1.8	13	24
3.7559	0.0467	<b>39.28</b>	<b>0.48</b>	102.2	1.7	30	177
3.7002	0.0541	<b>38.70</b>	<b>0.56</b>	97.2	1.8	13	20
3.6708	0.0442	<b>38.40</b>	<b>0.46</b>	96.8	2.2	31	102
3.8783	0.0440	<b>40.55</b>	<b>0.45</b>	94.7	1.9	29	167
4.3172	0.0638	<b>45.08</b>	<b>0.66</b>	99.2	1.3	31	243
3.9760	0.0695	<b>41.56</b>	<b>0.72</b>	96.3	1.1	20	58
5.3576	0.0793	<b>55.78</b>	<b>0.81</b>	94.5	1.6	12	20
3.8977	0.0513	<b>40.75</b>	<b>0.53</b>	95.2	2.2	35	104
3.7868	0.0588	<b>39.60</b>	<b>0.61</b>	98.3	1.6	9	14
4.0630	0.0507	<b>42.46</b>	<b>0.52</b>	95.9	1.9	11	19
3.9310	0.1014	<b>41.09</b>	<b>1.05</b>	95.9	1.2	64	1142
4.0626	0.0899	<b>42.45</b>	<b>0.93</b>	94.6	1.2	23	91

$^{40}\text{Ar}^*/^{39}\text{Ar}_{(\text{K})}$	$\pm 2\sigma$	Age	$\pm 2\sigma$	$^{40}\text{Ar}^*$	$^{39}\text{Ar}_{(\text{K})}$	K/Ca	$\pm 2\sigma$
		(Ma)		(%)	(%)		
3.35	0.02	<b>35.12</b>	<b>0.25</b>	93.5	2.4	26.0	4.9
3.25	0.04	<b>34.03</b>	<b>0.38</b>	95.7	1.5	2490	59933
3.42	0.02	<b>35.87</b>	<b>0.16</b>	92.5	2.8	7.34	0.81
3.10	0.02	<b>32.50</b>	<b>0.22</b>	92.4	2.8	20.4	2.9
3.26	0.02	<b>34.13</b>	<b>0.22</b>	93.6	3.2	50	12
3.44	0.02	<b>36.04</b>	<b>0.18</b>	93.0	3.5	17.0	2.2
3.42	0.04	<b>35.84</b>	<b>0.43</b>	92.9	1.7	4.48	0.49
3.29	0.06	<b>34.51</b>	<b>0.58</b>	91.5	1.1	15.4	3.8
3.37	0.02	<b>35.28</b>	<b>0.26</b>	92.5	2.3	12.8	1.5
3.27	0.01	<b>34.29</b>	<b>0.15</b>	94.0	3.4	13.0	1.5
3.32	0.02	<b>34.83</b>	<b>0.22</b>	95.4	2.6	7.06	0.77
3.21	0.02	<b>33.68</b>	<b>0.23</b>	94.2	2.5	22.3	3.8
3.27	0.03	<b>34.32</b>	<b>0.32</b>	88.0	2.4	11.2	1.3
3.33	0.02	<b>34.85</b>	<b>0.17</b>	91.6	2.6	11.5	1.3

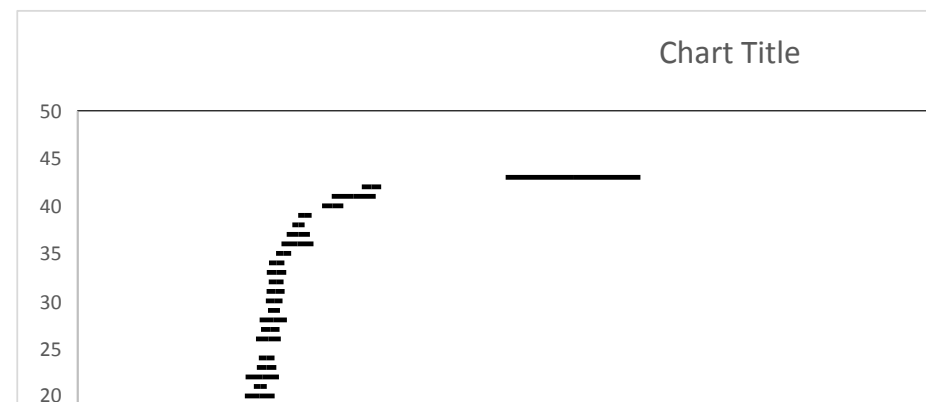
3.37	0.02	<b>35.29</b>	<b>0.20</b>	92.6	3.3	15.7	2.0	15	<b>34.36</b>	<b>0.27</b>
3.29	0.02	<b>34.45</b>	<b>0.18</b>	88.0	3.6	10.5	1.1	16	<b>34.45</b>	<b>0.18</b>
3.26	0.02	<b>34.19</b>	<b>0.26</b>	81.3	2.4	11.6	1.4	17	<b>34.51</b>	<b>0.58</b>
3.18	0.03	<b>33.35</b>	<b>0.28</b>	95.8	2.2	31.6	7.8	18	<b>34.65</b>	<b>0.15</b>
3.61	0.02	<b>37.81</b>	<b>0.26</b>	87.8	2.0	3.20	0.33	19	<b>34.83</b>	<b>0.22</b>
3.36	0.02	<b>35.22</b>	<b>0.22</b>	92.9	2.6	5.98	0.64	20	<b>34.84</b>	<b>0.40</b>
3.37	0.02	<b>35.27</b>	<b>0.20</b>	94.6	3.2	10.9	1.2	21	<b>34.85</b>	<b>0.17</b>
3.31	0.01	<b>34.65</b>	<b>0.15</b>	93.4	3.3	63	18	22	<b>34.91</b>	<b>0.44</b>
3.33	0.04	<b>34.91</b>	<b>0.44</b>	87.0	1.9	2.61	0.27	23	<b>35.02</b>	<b>0.26</b>
3.26	0.02	<b>34.15</b>	<b>0.20</b>	94.9	3.3	4.76	0.49	24	<b>35.02</b>	<b>0.21</b>
3.36	0.02	<b>35.22</b>	<b>0.16</b>	93.8	4.0	12.1	1.4			
3.25	0.02	<b>34.09</b>	<b>0.18</b>	88.6	3.5	4.12	0.42	25	<b>35.07</b>	<b>0.33</b>
3.34	0.02	<b>35.02</b>	<b>0.26</b>	92.7	2.4	3.11	0.32	26	<b>35.12</b>	<b>0.25</b>
3.51	0.03	<b>36.78</b>	<b>0.28</b>	92.7	2.0	2.02	0.20	27	<b>35.20</b>	<b>0.36</b>
4.13	0.17	<b>43.16</b>	<b>1.79</b>	91.6	0.4	2.4	5.1	28	<b>35.22</b>	<b>0.16</b>
3.36	0.03	<b>35.20</b>	<b>0.36</b>	91.5	1.3	3.1	1.7	29	<b>35.22</b>	<b>0.22</b>
3.32	0.04	<b>34.84</b>	<b>0.40</b>	95.3	1.3	8.5	12.6	30	<b>35.26</b>	<b>0.24</b>
3.18	0.03	<b>33.33</b>	<b>0.29</b>	93.5	2.0	4.7	3.4	31	<b>35.27</b>	<b>0.20</b>
3.36	0.02	<b>35.26</b>	<b>0.24</b>	94.0	2.6	12	19	32	<b>35.28</b>	<b>0.26</b>
3.39	0.02	<b>35.47</b>	<b>0.20</b>	91.6	2.5	9.6	6.5	33	<b>35.29</b>	<b>0.20</b>
3.42	0.03	<b>35.86</b>	<b>0.31</b>	86.2	1.3	5.9	4.4	34	<b>35.47</b>	<b>0.20</b>
3.15	0.04	<b>33.08</b>	<b>0.46</b>	94.9	1.3	19	99	35	<b>35.84</b>	<b>0.43</b>
3.26	0.02	<b>34.19</b>	<b>0.24</b>	94.8	2.4	53	352	36	<b>35.86</b>	<b>0.31</b>
3.34	2.85	<b>35.03</b>	<b>29.63</b>	7.6	0.0	0.7	5.9	37	<b>35.87</b>	<b>0.16</b>
3.28	0.03	<b>34.36</b>	<b>0.27</b>	85.9	2.1	4.0	2.0	38	<b>36.04</b>	<b>0.18</b>
3.22	0.02	<b>33.73</b>	<b>0.19</b>	89.9	3.2	10.3	10.3	39	<b>36.78</b>	<b>0.28</b>
3.35	0.03	<b>35.07</b>	<b>0.33</b>	86.4	1.5	7.3	11.3	40	<b>37.33</b>	<b>0.58</b>
3.34	0.02	<b>35.02</b>	<b>0.21</b>	81.6	2.8	8.3	4.3	41	<b>37.81</b>	<b>0.26</b>
3.57	0.06	<b>37.33</b>	<b>0.58</b>	92.8	0.8	17	112	42	<b>43.16</b>	<b>1.79</b>

$^{40}\text{Ar}^*/^{39}\text{Ar}_{(\text{K})}$	$\pm 2\sigma$	Age (Ma)	$\pm 2\sigma$	$^{40}\text{Ar}^*$ (%)	$^{39}\text{Ar}_{(\text{K})}$ (%)	K/Ca	$\pm 2\sigma$				
4.13	0.03	<b>43.12</b>	<b>0.33</b>	96.9	2.8	257	576	1	WM	<b>38.62</b>	<b>0.45</b>
4.08	0.03	<b>42.68</b>	<b>0.34</b>	94.8	2.8	359	1568	2	WM	<b>39.86</b>	<b>0.39</b>
3.91	0.03	<b>40.88</b>	<b>0.30</b>	99.5	4.0	455	1335	3	WM	<b>39.94</b>	<b>0.52</b>
3.92	0.03	<b>41.05</b>	<b>0.33</b>	97.6	3.0	96	78	4	WM	<b>40.09</b>	<b>1.08</b>
3.87	0.07	<b>40.45</b>	<b>0.67</b>	93.3	1.6	97	179	5	WM	<b>40.20</b>	<b>0.42</b>
3.95	0.02	<b>41.30</b>	<b>0.22</b>	97.4	5.0	95	58	6	WM	<b>40.25</b>	<b>0.41</b>
4.15	0.06	<b>43.32</b>	<b>0.57</b>	85.5	1.6	5.8	1.0	7	WM	<b>40.34</b>	<b>0.18</b>
3.97	0.02	<b>41.52</b>	<b>0.23</b>	99.0	4.4	51	23	8	WM	<b>40.41</b>	<b>0.49</b>
3.86	0.02	<b>40.34</b>	<b>0.18</b>	98.7	4.9	382	764	9	WM	<b>40.42</b>	<b>0.26</b>
4.35	0.02	<b>45.46</b>	<b>0.22</b>	98.7	4.0	1021	8175	10	WM	<b>40.45</b>	<b>0.67</b>
3.93	0.03	<b>41.12</b>	<b>0.27</b>	97.0	3.6	55	27	11	WM	<b>40.45</b>	<b>0.56</b>
4.53	0.06	<b>47.28</b>	<b>0.62</b>	98.2	1.7	-1978	83151	12	WM	<b>40.54</b>	<b>0.57</b>
5.36	0.09	<b>55.78</b>	<b>0.93</b>	96.8	1.2	76	167	13	WM	<b>40.62</b>	<b>0.80</b>
3.88	0.08	<b>40.62</b>	<b>0.80</b>	99.1	1.4	38	32	14	WM	<b>40.67</b>	<b>0.54</b>
4.31	0.06	<b>45.04</b>	<b>0.65</b>	95.2	1.5	4.08	0.59	15	WM	<b>40.88</b>	<b>0.30</b>
3.89	0.05	<b>40.67</b>	<b>0.54</b>	94.3	2.0	49	33	16	WM	<b>40.94</b>	<b>0.31</b>
5.56	0.03	<b>57.87</b>	<b>0.31</b>	99.2	3.1	88	64	17	WM	<b>41.05</b>	<b>0.33</b>
3.82	0.05	<b>39.94</b>	<b>0.52</b>	94.7	2.0	35	20	18	WM	<b>41.10</b>	<b>0.90</b>
3.92	0.03	<b>40.94</b>	<b>0.31</b>	97.3	3.4	239	529	19	WM	<b>41.12</b>	<b>0.27</b>
3.84	0.04	<b>40.20</b>	<b>0.42</b>	96.1	2.2	120	164	20	WM	<b>41.30</b>	<b>0.22</b>
4.47	0.06	<b>46.68</b>	<b>0.60</b>	83.3	1.2	117	277	21	WM	<b>41.40</b>	<b>0.24</b>
4.85	0.12	<b>50.60</b>	<b>1.24</b>	99.0	0.8	6	18	22	WM	<b>41.52</b>	<b>0.23</b>
3.83	0.10	<b>40.09</b>	<b>1.08</b>	90.8	1.0	21	198	23	WM	<b>42.68</b>	<b>0.34</b>
4.28	0.04	<b>44.72</b>	<b>0.42</b>	95.4	2.4	11	19	24	WM	<b>43.12</b>	<b>0.33</b>
3.88	0.05	<b>40.54</b>	<b>0.57</b>	87.7	1.7	4.5	4.4	25	WM	<b>43.30</b>	<b>0.29</b>
5.91	0.11	<b>61.45</b>	<b>1.16</b>	89.8	0.9	8	20	26	WM	<b>43.32</b>	<b>0.57</b>
4.68	0.04	<b>48.79</b>	<b>0.40</b>	98.8	2.8	54	315	27	WM	<b>44.72</b>	<b>0.42</b>
31.22	15.41	<b>303.34</b>	<b>137.81</b>	40.3	0.0	0.07	0.16	28	WM	<b>45.04</b>	<b>0.65</b>
3.69	0.04	<b>38.62</b>	<b>0.45</b>	95.5	2.0	383	35263	29	WM	<b>45.46</b>	<b>0.22</b>
3.93	0.09	<b>41.10</b>	<b>0.90</b>	86.5	1.4	7	20	30	WM	<b>46.68</b>	<b>0.60</b>
5.25	0.03	<b>54.69</b>	<b>0.27</b>	98.8	3.8	11	15	31	WM	<b>47.28</b>	<b>0.62</b>
4.14	0.03	<b>43.30</b>	<b>0.29</b>	98.1	3.9	-18	54	32	WM	<b>48.79</b>	<b>0.40</b>
3.81	0.04	<b>39.86</b>	<b>0.39</b>	98.7	2.9	-32	198	33	WM	<b>48.90</b>	<b>0.26</b>
3.87	0.05	<b>40.45</b>	<b>0.56</b>	96.1	1.8	11	42	34	WM	<b>50.60</b>	<b>1.24</b>
3.85	0.04	<b>40.25</b>	<b>0.41</b>	97.6	1.9	39	541	35	WM	<b>54.69</b>	<b>0.27</b>
3.86	0.03	<b>40.42</b>	<b>0.26</b>	97.9	3.5	26	101	36	WM	<b>55.78</b>	<b>0.93</b>
3.96	0.02	<b>41.40</b>	<b>0.24</b>	96.8	4.8	29	99	37	WM	<b>57.87</b>	<b>0.31</b>
3.86	0.05	<b>40.41</b>	<b>0.49</b>	99.5	2.3	16	68	38	Kfs?	<b>61.45</b>	<b>1.16</b>
4.69	0.02	<b>48.90</b>	<b>0.26</b>	96.6	4.2	28	86	39	Kfs?	<b>70.62</b>	<b>2.84</b>
6.81	0.28	<b>70.62</b>	<b>2.84</b>	103.1	0.4	1.6	3.7	40	Pl	<b>303.34</b>	<b>137.81</b>

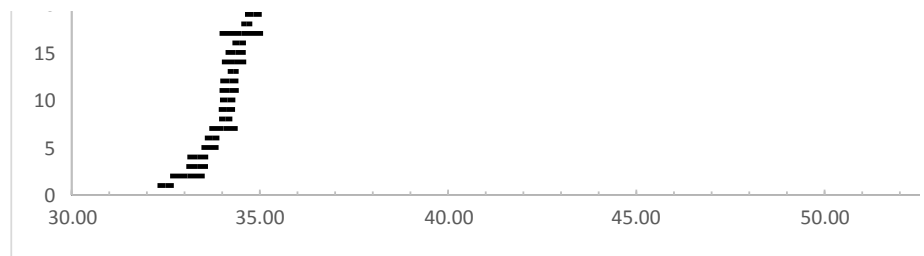
1  
2  
3  
4  
5  
6  
7  
8  
9  
10  
11  
12  
13  
14  
15  
16  
17  
18  
19  
20  
21  
22  
23  
24  
25  
26  
27  
28  
29  
30  
31  
32  
33  
34  
35  
36  
37  
38  
39  
40  
41  
42  
43  
44  
45  
46  
47  
48  
49



1  
2  
3  
4  
5  
6  
7  
8  
9  
10  
11  
12  
13  
14



15  
16  
17  
18  
19  
20  
21  
22  
23  
24  
25  
26  
27  
28  
29  
30  
31  
32  
33  
34  
35  
36  
37  
38  
39  
40  
41  
42  
43



1  
2  
3  
4  
5  
6  
7  
8  
9  
10  
11  
12  
13  
14  
15  
16  
17  
18  
19  
20  
21  
22  
23  
24  
25  
26  
27  
28  
29  
30  
31  
32  
33  
34  
35  
36  
37  
38  
39  
40

